VOLUME 39 MAY 1961 NUMBER 5

Canadian Journal of Physics

Published by THE NATIONAL RESEARCH COUNCIL

OTTAWA CANADA

CANADIAN JOURNAL OF PHYSICS

Under the authority of the Chairman of the Committee of the Privy Council on Scientific and Industrial Research, the National Research Council issues THE CANADIAN JOURNAL OF PHYSICS and five other journals devoted to the publication, in English or French, of the results of original scientific research. Matters of general policy concerning these journals are the responsibility of a joint Editorial Board consisting of: members representing the National Research Council of Canada; the Editors of the Journals; and members representing the Royal Society of Canada and four other scientific societies.

Manuscripts for publication should be submitted to Dr. H. E. Duckworth, Editor, Canadian Journal of Physics, Hamilton College, McMaster University, Hamilton, Ontario.
For instructions on preparation of copy, see **NOTES TO CONTRIBUTORS** (back cover).

Proof, correspondence concerning proof, and orders for reprints should be sent to the Manager, Editorial Office (Research Journals), Division of Administration and Awards, National Research Council, Ottawa 2, Canada.

Subscriptions, renewals, requests for single or back numbers, and all remittances should be sent to Division of Administration and Awards, National Research Council, Ottawa 2, Canada. Remittances should be made payable to the Receiver General of Canada, credit National Research Council.

The journals published, frequency of publication, and subscription prices are:

Canadian Journal of Biochemistry and Physiology	Monthly	$9.00 a year
Canadian Journal of Botany	Bimonthly	$6.00 a year
Canadian Journal of Chemistry	Monthly	$12.00 a year
Canadian Journal of Microbiology	Bimonthly	$6.00 a year
Canadian Journal of Physics	Monthly	$9.00 a year
Canadian Journal of Zoology	Bimonthly	$5.00 a year

The price of regular single numbers of all journals is $2.00.

Canadian Journal of Physics

Issued by THE NATIONAL RESEARCH COUNCIL OF CANADA

VOLUME 39 MAY 1961 NUMBER 5

PHOTONEUTRON REACTIONS IN C^{12} AND O^{16} [1]

J. P. ROALSVIG,[2] ISHWAR C. GUPTA, AND R. N. H. HASLAM

ABSTRACT

Absolute yields of the reactions $C^{12}(\gamma,n)C^{11}$ and $O^{16}(\gamma,n)O^{15}$ have been determined at 22-Mev maximum bremsstrahlung energy using the University of Saskatchewan 24-Mev betatron. For the reaction $C^{12}(\gamma,n)C^{11}$ a yield curve from threshold to 24 Mev has been obtained and the cross-section curve for the reaction computed. A thorough comparison with other results has been made.

INTRODUCTION

The reactions $C^{12}(\gamma,n)C^{11}$ and $O^{16}(\gamma,n)O^{15}$ have been investigated by several authors: Price and Kerst (1950), Haslam *et al.* (1951), Montalbetti *et al.* (1953), Nathans and Halpern (1954), Katz *et al.* (1954), Barber *et al.* (1955), Cook (1957), and Thorson (1957).

However, in view of the discrepancies of the results obtained (see Tables I and II) a redetermination of the activation and the cross-section curve for $C^{12}(\gamma,n)C^{11}$ was thought desirable. It was of particular interest to find out whether most of the reaction cross section took place by photon absorption into discrete nuclear levels or into the giant dipole resonance. The results in the case of the $O^{16}(\gamma,n)O^{15}$ reaction also cover a wide range. Due to this discrepancy and since the technique of absolute β counting is now a little better understood (Roalsvig and Haslam 1959) it was considered desirable to remeasure the absolute yield of the $O^{16}(\gamma,n)O^{15}$ reaction. The values obtained in the present work are thought to be of greater accuracy than those published from this department before, due to greatly improved knowledge of the betatron energy scale at the present time.

EXPERIMENTAL TECHNIQUE

(*a*) The carbon samples consisted of cylinders of polystyrene, 7.5 cm long with an outside diameter of 2.6 cm and a wall thickness of 2 mm. The samples were irradiated in the center of the X-ray beam from the University of Saskatchewan 24-Mev betatron. They were placed in a fixed position 60 cm from the betatron target, with their cylindrical axes perpendicular to the beam direction.

[1]Manuscript received January 17, 1961.
Contribution from the Physics Department, University of Saskatchewan, Saskatoon, Saskatchewan.
[2]Present address: Physics Department, St. John's University, Jamaica, New York, U.S.A.

The secondary activity from C^{11} with a half life of 20.5 minutes was counted with a Victoreen IB85 cylindrical Geiger–Müller counter placed inside a thick lead castle. The β^+ activity was counted in the time interval between 10 and 20 minutes after the irradiation was stopped. Any activity due to O^{15}, which decays with a half life of 2.1 minutes, was then found to be negligible.

(*b*) For the determination of absolute yields of $O^{16}(\gamma,n)O^{15}$ and $C^{12}(\gamma,n)C^{11}$, samples of mylar polyester ($C_{15}H_{12}O_6$) in the form of circular disks of 2.5 cm diameter and various thicknesses were irradiated in the center of the X-ray beam. The samples were placed at a fixed position of 18.3 cm from the target. The irradiation time was 2 minutes for studying the $O^{16}(\gamma,n)O^{15}$ reaction and 15 minutes for the study of the reaction $C^{12}(\gamma,n)C^{11}$.

The samples were then mounted on different backscatterers (C, Al, Cu, Cd, and Pb) and the total secondary activity produced (i.e. O^{15} with a half life of 2.1 minutes and C^{11} with a half life of 20.5 minutes) was measured. The counting was done using a proportional flow counter and the activities were followed for several half lives.

From the plots of counts/minute versus time, the C^{11} activity (which forms the background for the O^{15} activity) was obtained and subtracted from the total activity, yielding the O^{15} activity produced in the sample.

The counting rates were corrected for background and for counting losses due to the dead time of the tube. In the case of the proportional flow counter, the counting loss is less than 0.1% for a counting rate of 200,000 counts/minute. No correction for counting loss was necessary, since the counting rate was usually in the neighborhood of 10,000 counts/minute. In case of counting by the Geiger tube, the counting loss is relatively higher and therefore the following formula was used for this correction.

$$K_T = \frac{(e^{\lambda\rho K_M}-1)(\tau_1-\tau_2)}{\lambda\rho(\tau_1-e^{\lambda\rho K_M}\tau_2)}$$

where K_T is the corrected number of counts,

K_M is the measured number of counts,

λ is the disintegration constant (0.0338 min^{-1} for C^{11}),

ρ is the dead time of the tube,

$\tau_1 = e^{-\lambda t_1}$, $\tau_2 = e^{-\lambda t_2}$, where t_1 and t_2 are 10 and 20 minutes respectively.

The energy stability of the betatron was checked regularly by irradiating samples of boric acid at a fixed integrator setting (called monitor point) and measuring the induced 2.1-minute β^+ activity from O^{15}. During the course of the experiment the total energy drift was about 50 kev, but the integrator setting was correspondingly adjusted. The maximum unaccounted for drift was about 9 kev.

Two slightly different procedures were used to obtain relative activation curves:

(*a*) The samples were given a known relative dose, measured by a monitor in connection with a condenser (see Johns *et al.* 1950). Values for roentgens per unit relative dose for different maximum photon energies were obtained using a Baldwin–Farmer type r-meter. Thus relative numbers of counts per

roentgen could be obtained. These were corrected to relative saturated activity by multiplication by the factor $t_R\{1-\exp(-\lambda t_R)\}^{-1}$, where t_R is the irradiation time and λ is the disintegration constant.

(*b*) All samples were irradiated for the same length of time. The relative dose was measured by a monitor in connection with an R–C circuit, whose time constant equaled the mean life of the activity under consideration. Relative values of roentgens per unit dose were obtained by using a Baldwin–Farmer type r-meter.

The two relative activation curves for $C^{12}(\gamma,n)C^{11}$ reaction when normalized at 22 Mev showed good agreement, deviations being within statistical uncertainty.

NORMALIZATION AND RESULTS

(*a*) The relative yield curve for the reaction $C^{12}(\gamma,n)C^{11}$ was normalized by using the reaction $Cu^{63}(\gamma,n)Cu^{62}$ as a standard. Circular disks of copper and polystyrene were used, with diameter 2.5 cm and thicknesses ranging from 10 mg/cm² to several hundred mg/cm². All disks were irradiated at 22-Mev maximum photon energy, the relative dose being measured with a monitor as under (*a*) above. The secondary activities were counted in a proportional flow counter and followed for several half lives. The number of counts/minute at $t = 0$ were corrected for finite irradiation time and divided by the number of g-atoms of C^{12} and Cu^{63} respectively in the samples, and also by the number of relative dose units given to the disks. The correction factor for the self-absorption in the sample, backscattering, and absorption of the backscattered β^+-particles was calculated using the empirical formulae given by Roalsvig and Haslam (1959).

The ratio of the saturated activity of the reaction $Cu^{63}(\gamma,n)Cu^{62}$ in neutrons per g-atom per relative dose unit at 22 Mev to that of the reaction $C^{12}(\gamma,n)C^{11}$ was found to be 196 ± 2. The absolute yield value for the former reaction has recently been determined in this laboratory (Roalsvig, Haslam, and McKenzie 1959). Uncorrected for absorption of X rays in the lucite block surrounding the r-meter thimble chamber, this value was found to be 2.42×10^8 n/g-atom per 100 r at 22 Mev. The uncorrected yield value for the reaction $C^{12}(\gamma,n)C^{11}$ thus becomes 1.23×10^6 n/g-atom per 100 r. The correction factor for absorption in the lucite block was calculated to be 1.070 for the latter reaction, thus giving an absolute yield value of 1.15×10^6 n/g-atom per 100 r for the reaction $C^{12}(\gamma,n)C^{11}$ at 22 Mev. The absolute yield values quoted in this paper are those that would be obtained if the sample were placed in the center of an 8-cm lucite cube in the same position as the r-meter. These values are approximately 7% lower than if the sample were placed in air at the same distance from the betatron target.

(*b*) The absolute yield of $C^{12}(\gamma,n)C^{11}$ at 22 Mev was also determined without using the empirical relations for the correction factors for self-absorption in the sample, backscattering, and absorption of backscattered β^+-particles. The experimental technique followed was similar to that of Roalsvig and Haslam (1959). The dose in this case was calibrated against a Victoreen thimble in

an 8-cm lucite block. Dose calibration was checked by determining the $Cu^{63}(\gamma,n)Cu^{62}$ yield also.

For the determination of the absolute yield, the counting rates after subtracting background and any other undesirable activity were plotted against time. From these plots the counting rate at $t = 0$ after irradiation was obtained. This quantity was divided by the number of g-atoms of C^{12} and the relative dose (which was already corrected for the decay of the observed activity in the sample during the irradiation). The values of this new quantity, called $N'(x,z)$, where x refers to the thickness of the sample and z to the atomic number of the backscatterer, were plotted against z for each value of x and against x for each value of z (see Figs. 1, 2, 3, and 4). From the extrapolation of these curves the values of $N'(0,0)$ were obtained. The absolute yield was obtained by using the average value of $N'(0,0)$, multiplying it by the geometry factor (for the system used, the geometry factor was 2), and dividing by the number of 100 roentgens per unit registered dose (for further details, see Roalsvig and Haslam 1959).

The absolute yield curve, normalized to the value 1.15×10^6 n/g-atom per 100 r for the reaction $C^{12}(\gamma,n)C^{11}$ at 22 Mev, is given in Fig. 5. The cross-section curve was calculated by using the "modified total spectrum method" of Penfold and Leiss (1958) and is shown in Fig. 6. The cross-section curve is seen to have its maximum at 23.0 Mev with $\sigma_{max} = 7.9$ millibarns. The half width of the curve, $\Gamma_{\frac{1}{2}}$, is 3.2 Mev, and the integrated cross section from threshold to 24 Mev is 0.022 Mev barn.

(*c*) The absolute yield of the reaction $O^{16}(\gamma,n)O^{15}$ was determined in the same way as outlined in Part (*b*) of this section. Three independent runs of the experiment were made. The average value for the absolute yield for $O^{16}(\gamma,n)O^{15}$ reaction at 22 Mev (maximum energy) X rays is $(2.37\pm0.2)\times10^6$ n/g-atom per 100 r.

DISCUSSION

(a) The Yield Values

The measured yield values at 22 Mev are given in Table I. The absolute

TABLE I

Absolute yields of $O^{16}(\gamma,n)O^{15}$ and $C^{12}(\gamma,n)C^{11}$ at 22 Mev

References	Absolute yield of $O^{16}(\gamma,n)O^{15}$ (n/g-atom 100 r)	Absolute yield of $C^{12}(\gamma,n)C^{11}$ (n/g-atom 100 r)
Price and Kerst (1950)	0.67×10^6	0.67×10^6
Haslam, Johns, and Horsley (1951)	—	0.75×10^6
Johns, Horsley, Haslam, and Quinton (1951)	1.68×10^6	—
Montalbetti *et al.* (1953)	2.7×10^6	3.2×10^6
Nathans and Halpern (1954)	—	2.8×10^6
Barber *et al.* (1955)	—	2.3×10^6
Cook (1957)	—	1.5×10^6[a]
Thorson (1957)	—	0.76×10^6
Present work	2.37×10^6	1.15×10^6[b]

[a]According to the note added in proof the author mentions that this value should be reduced by 10%.
[b]A redetermination of the absolute yield gave results in close agreement with this value.

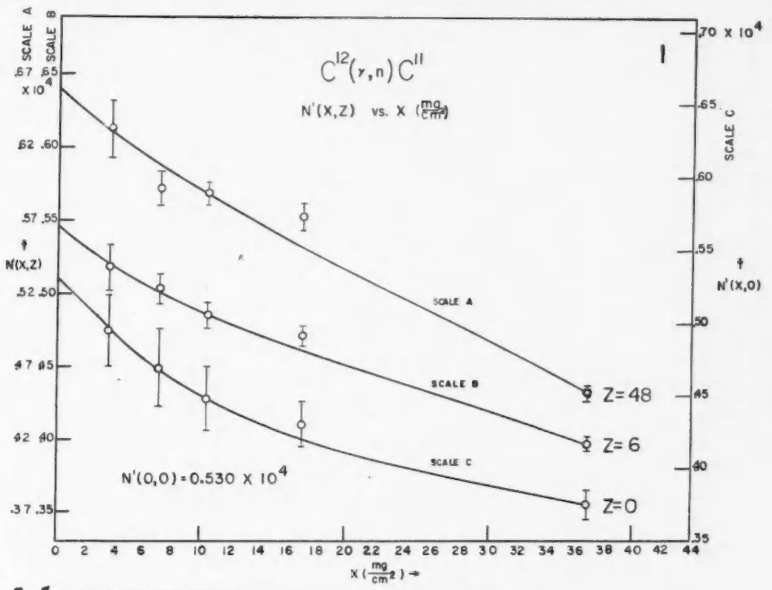

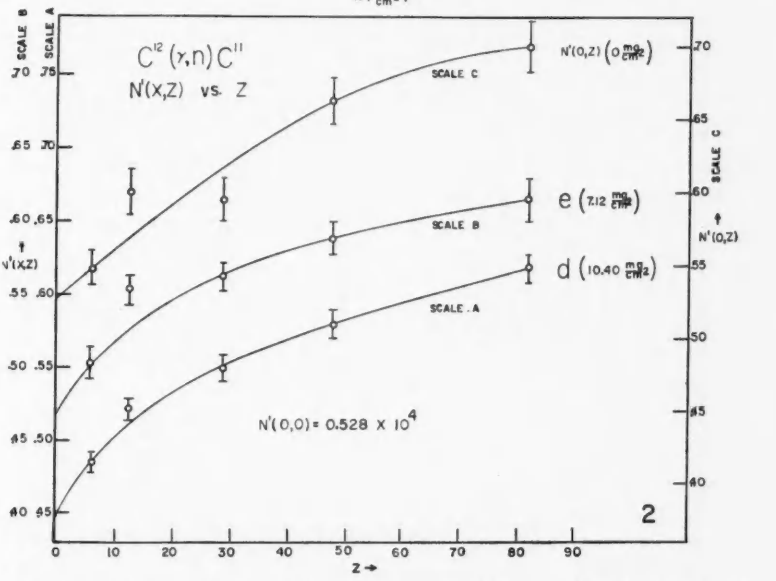

FIG. 1. Relative counting rate $N'(x,z)$ versus sample thickness, x, for a fixed value of the atomic number of backscattering material (for C^{11} positrons).

FIG. 2. Relative counting rate $N'(x,z)$ versus z, the atomic number of the backscatterer, for a fixed value of x, the sample thickness (for C^{11} positrons). e and d designate two typical sample thicknesses.

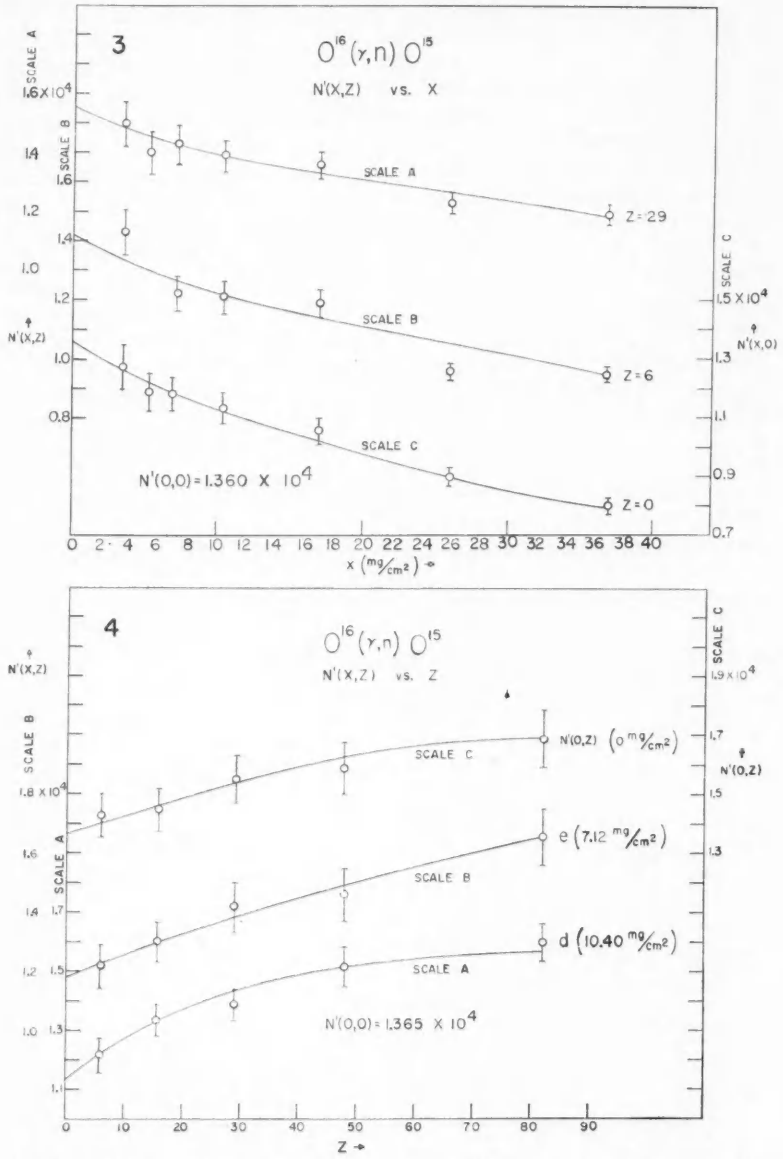

FIG. 3. Relative counting rate $N'(x,z)$ versus sample thickness, x, for a fixed value of the atomic number of backscattering material (for O^{15} positrons).

FIG. 4. Relative counting rate $N'(x,z)$ versus z, the atomic number of the backscatterer, for a fixed value of x, the sample thickness (for O^{15} positrons). e and d designate two typical sample thicknesses.

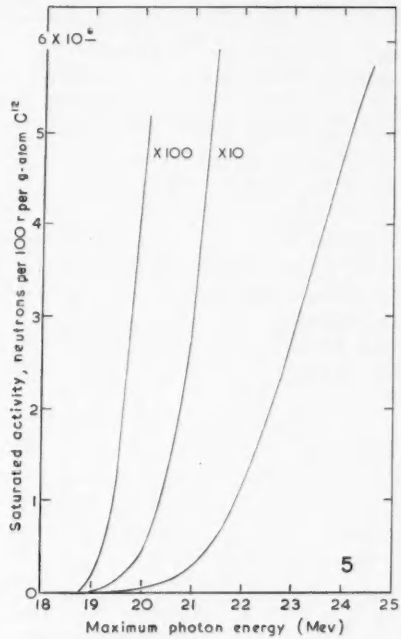

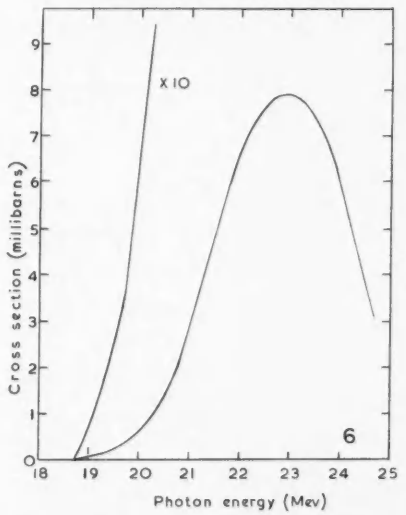

FIG. 5. Absolute activation curve for the reaction $C^{12}(\gamma,n)C^{11}$.
FIG. 6. Cross-section curve for the reaction $C^{12}(\gamma,n)C^{11}$.

yield values of the $C^{12}(\gamma,n)C^{11}$ reaction show a large discrepancy, varying from 0.67×10^6 n/g-atom per 100 r to 3.2×10^6 n/g-atom per 100 r, that is by a factor greater than 4. To investigate this great discrepancy, the activation curves from the investigations in which the photon source was a betatron were drawn on the same figure, Fig. 7. From this figure it is clearly seen that the shapes of the activation curves are generally quite similar, the curves being, however, displaced from each other along the energy axis. Thus, for example, a displacement of the curve of Montalbetti *et al.* of about 1.35 Mev to the right would make it coincide with the curve of the present work. This may thus indicate that the main source of error in obtaining the absolute yield at the standard point 22 Mev is in the energy calibration of the betatron. Due to the rapid variation of the yield with energy, a rather small displacement in energy will give a high difference in the absolute yield.

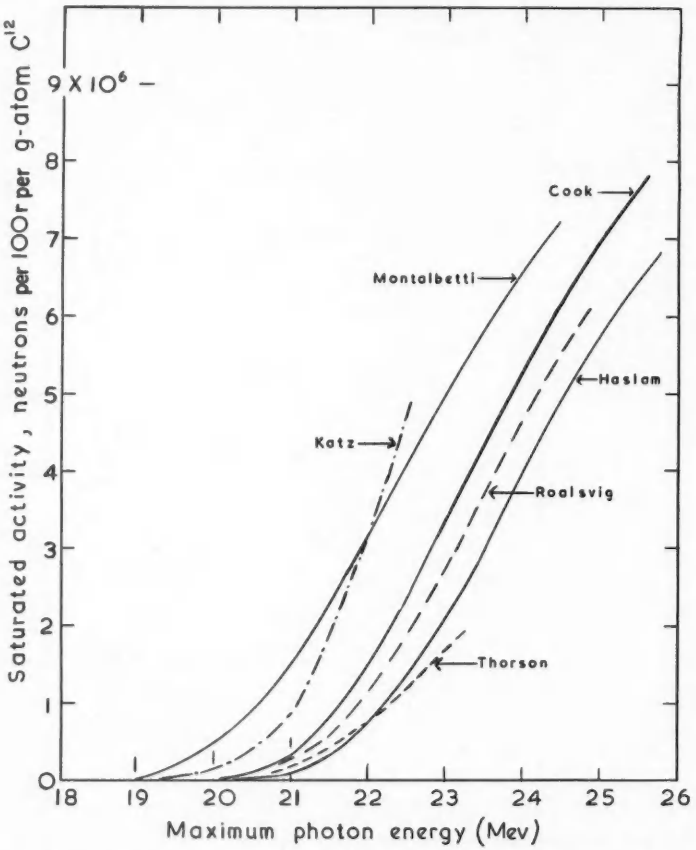

FIG. 7. Activation curves for the reaction $C^{12}(\gamma,n)C^{11}$, as given by different authors.

Our value of the absolute yield of $O^{16}(\gamma,n)O^{15}$ at 22 Mev is 2.37×10^6 n/g-atom per 100 r. This is twice as great as our value for the yield of the $C^{12}(\gamma,n)C^{11}$ reaction. Price and Kerst (1950) and Montalbetti *et al.* (1953) report nearly the same yields for the two reactions. However, if as suggested earlier, in the curves of Montalbetti *et al.*, the energy scale is shifted by 1.35 Mev, the ratio of the yields of $O^{16}(\gamma,n)O^{15}$ to $C^{12}(\gamma,n)C^{11}$ at 22 Mev becomes $\simeq 1.7$. The ratio of the yields obtained in our experiment is in very good agreement with those of Haslam *et al.* (1951) and Johns *et al.* (1951). Carver and Lokan (1957) report the yields of $C^{12}(\gamma,n)C^{11}$ and $O^{16}(\gamma,n)O^{15}$ in arbitrary units as 0.8 and 1.5 respectively. If the arbitrary units are the same in both the reactions then this result is also in agreement with ours. Further checks on the $C^{12}(\gamma,n)C^{11}$ yield were made by determining the ratio of the yields of $O^{16}(\gamma,n)O^{15}$ to $C^{12}(\gamma,n)C^{11}$, which was found to be 2.28. Using our value of oxygen yield we get for the $C^{12}(\gamma,n)C^{11}$ reaction at 22 Mev a yield of 1.04×10^6 n/g-atom per 100 r.

The similarity in the shape of the activation curves in $C^{12}(\gamma,n)C^{11}$ suggests that the cross-section curves would also exhibit similar shapes, though displaced with respect to the scale of photon energy. Thus the variation in E_{max}, the energy at which the cross-section curve has its maximum value, should provide a measure of the variation in the energy scale. The greater the apparent energy E_{max}, the lower should be the yield at some fixed energy below E_{max}, for example, 22 Mev. That this is the case is shown quite clearly in Fig. 8, in which the yield values reported for a bremsstrahlung energy of 22 Mev are plotted against E_{max}.

If the shapes of the activation curves had been exactly similar, and if the same method had been used by all authors to calculate the cross-section

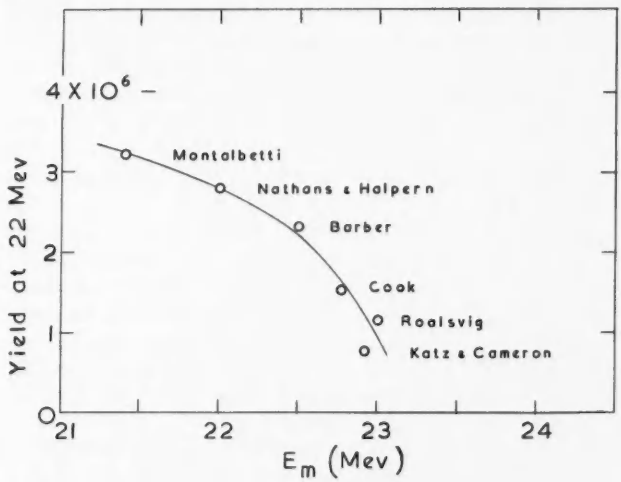

FIG. 8. Relation between the yield at 22 Mev and E_{max}, the energy at which the cross-section curve has its maximum value.

curves, the values of the yields at E_{max} should have been the same. These yield values are given in Table II, column 3. Although there is some variation, from 1.95×10^6 n/g-atom per 100 r to 3.45×10^6 n/g-atom per 100 r, the spread is much lower than for the yield values at 22 Mev. It would, therefore, seem more valuable, while energy scales are in doubt, to use the energy E_{max} as a comparison point for the absolute yield, rather than an arbitrary energy value such as 22 Mev.

From Table II, it is seen that the average value of E_{max} for the $C^{12}(\gamma,n)C^{11}$ reaction when taking all results into consideration is 22.4 Mev with a standard deviation of 0.6 Mev. Correspondingly from Fig. 8, one might deduce a "mean value" of the yield at 22 Mev of 2.4×10^6 n/g-atom per 100 r with an uncertainty of $+0.5\times10^6$ n/g-atom per 100 r and -1.4×10^6 n/g-atom per 100 r for this reaction. However, the actual mean value of the yields for $C^{12}(\gamma,n)C^{11}$ at 22 Mev is $(1.6\pm1.0)\times10^6$ n/g-atom per 100 r. The relatively low value of the yield of $C^{12}(\gamma,n)C^{11}$ at this energy obtained in the present work, 1.15×10^6 n/g-atom per 100 r, corresponds to a relatively high value of E_{max}.

(b) The Cross Sections

The integrated cross sections from threshold to an energy E_1 as reported by the different authors are given in Table II, column 6. The different values of the energy E_1 are also given in parentheses in Mev. In order to get comparable values of $\int_{thresh}^{E_1}\sigma(\gamma,n)dE$, a constant value of E_1 has to be used, the value 24 Mev has been chosen here. The integrated cross sections from threshold up to this energy have been tabulated from the reported cross-section curves, the values being given in Table II, column 7. The agreement between these values is rather good, the average value is found to be 0.026 Mev barn with a standard deviation of 0.003 Mev barn.

The difference in the values is mainly due to inaccuracy in computing the cross section from the measured activation curves. If this procedure had been more accurate, decreasing values of $\int_{thresh}^{24\text{ Mev}}\sigma(\gamma,n)dE$ should be expected to appear with increasing values of E_{max}. No such relationship is, however, indicated by the reported values as seen from Fig. 9*a*. Also the values of σ_{max}, the maximum cross section, should be expected to be constant. As seen from Table II, column 4, these values have, however, a rather high standard deviation of about 25%.

If the error introduced by computing cross-section curves was independent of the energy scale, the "normalized integrated cross section", defined as $\int_{thresh}^{24\text{ Mev}}\sigma(\gamma,n)dE/\sigma_{max}$ and given in Table II, column 8, should show decreasing values with increasing E_{max}. This is generally not the case, as seen from Fig. 9*b*. Thus a distortion with energy does also take place, which might also be seen from the divergent values of the half widths $\Gamma_{\frac{1}{2}}$ as given in Table II, column 5. A more accurate method of computing cross section from the activation values is therefore highly desirable.

However, one might say that to a first approximation, at least up to E_{max}, the shape of the cross-section curve is fairly well established. This is also indicated by Fig. 10, which shows the decrease of $\int_{thresh}^{24\text{ Mev}}\sigma(\gamma,n)dE$ with decreasing values of σ_{max}.

TABLE II

1	2	3	4	5	6	7	8	9	10
References	E_{max} (Mev) energy for max σ	Yield at E_{max} (n/g-atom 100 r)	σ_{max} (mb)	Half width $\Gamma_{\frac{1}{2}}$ (Mev)	$\int_{thresh}^{E_1}\sigma(\gamma,n)dE$ (Mev barn)		Norm. integr. cross section (Mev)	$\sum_{thresh}^{24\ Mev} G\int\sigma_i dE$ (Mev barn)	
					E_1 (Mev)	E_1 = 24 Mev		As given by authors	Norm. to present yield
Haslam *et al.* (1951)	22.4		11.6	4.2	0.047 (27)	0.028	2.41		
Katz and Cameron (1951)[a]	22.9	1.95×10^6	13.1	2.8	0.046 (27)	0.030	2.29		
Montalbetti *et al.* (1953)	21.4	2.05×10^6	13.4	2.0	0.029 (24)	0.029	2.16		
Nathans and Halpern (1954)	22.0	Activation curve not given in paper	8.6	3.0	0.027 (25)	0.025	2.91		
Barber *et al.* (1955)	22.5	3.45×10^6	8.3	4.3	0.032 (25)	0.027	3.25		
Cook (1957)	22.8	2.75×10^6	10.4	3.5	0.034 (25)	0.028	2.69		
Present work	23.0	2.77×10^6	7.9	3.2	0.022 (24)	0.022	2.78		
Katz *et al.* (1954)[b]								0.055	0.019
Thorson (1957)								0.0085	0.013
Average values[c]	22.4	2.6×10^6	10.3	3.1		0.026			0.016[d]
Standard deviation	0.6	0.3×10^6	2.6	0.8		0.003			0.003

[a] Recalculation of values of Haslam *et al.* (1951) using the photon-difference method.
[b] Values are normalized according to Montalbetti *et al.* (1953).
[c] Values of Haslam *et al.* (1951) are not included directly, but indirectly under Katz and Cameron (1951).
[d] This value should be compared to the present value 0.022 Mev barn for a smooth yield curve.

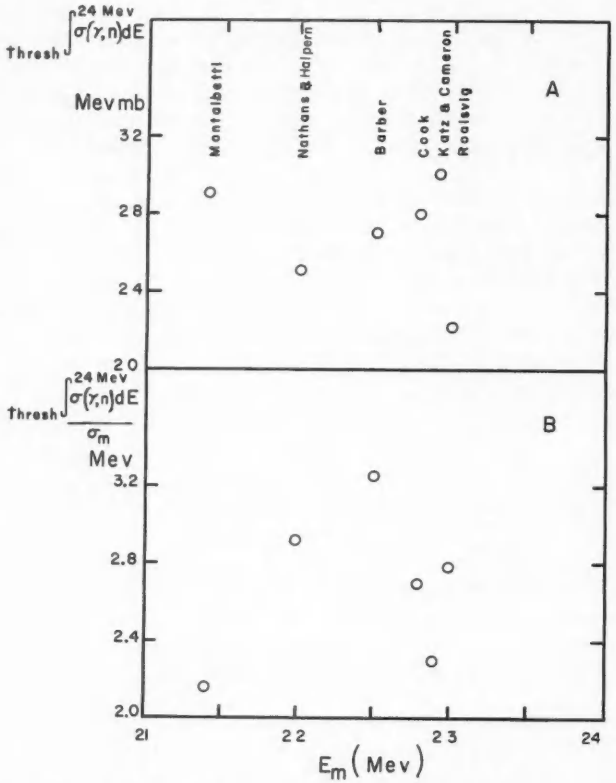

FIG. 9. (*a*) Relation between the integrated cross section from threshold to 24 Mev, and E_{max}, the energy at which the cross-section curve has its maximum value.
(*b*) Relation between the "normalized integrated cross section" from threshold to 24 Mev, and E_{max}, the energy at which the cross-section curve has its maximum value.

(c) Cross Section under the Breaks

The integrated cross section under the breaks in the fine structure of the activation curve $\sum_{thresh}^{24\ Mev} G\int \sigma_i dE$ has been investigated by Katz *et al.* (1954) and Thorson (1957), the values being given in Table II, column 9. These two values are, however, not directly comparable, since the value of Katz *et al.* is obtained by using the yield value of Montalbetti *et al.* of 3.2×10^6 n/g-atom per 100 r at 22 Mev, while Thorson determined this value to be 0.76×10^6 n/g-atom per 100 r.

When both these integrated cross-section values are normalized according to the yield value of 1.15×10^6 n/g-atom per 100 r as obtained in the present work, they become 0.019 Mev barn and 0.013 Mev barn respectively. The average value 0.016 ± 0.003 Mev barn should then be compared with the value 0.022 Mev barn for the continuous integrated cross section. This should

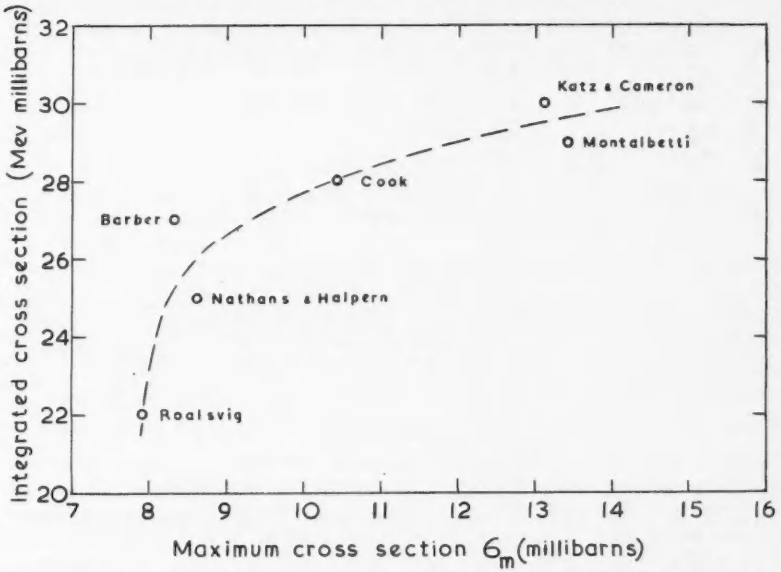

FIG. 10. Relation between the integrated cross section from threshold to 24 Mev, and the maximum cross section.

thus indicate that a substantial fraction, namely 75±20% of the $C^{12}(\gamma,n)C^{11}$ reaction cross section is due to photon absorption into discrete nuclear levels located at the energies of the observed breaks in the activation curve.

SUMMARY

The absolute yield for $O^{16}(\gamma,n)O^{15}$ reaction has been determined and is found to be $(2.37\pm0.2)\times10^6$ n/g-atom per 100 r. The absolute yield and the activation curve for the reaction $C^{12}(\gamma,n)C^{11}$ have been measured and the corresponding cross-section curve calculated. These have been compared with previous investigations, and reasons for the discrepancy in absolute yields and cross sections have been discussed. By taking all works on the reaction $C^{12}(\gamma,n)C^{11}$ up to the present, average values of various parameters are:

(*a*) yield at 22 Mev: $(1.6\pm1.0)\times10^6$ n/g-atom per 100 r,
(*b*) E_{max}: 22.4±0.6 Mev,
(*c*) yield at E_{max}: $(2.6\pm0.3)\times10^6$ n/g-atom per 100 r,
(*d*) σ_{max}: 10.3±2.5 millibarns,
(*e*) $\Gamma_{\frac{1}{2}}$: 3.1±0.8 Mev,
(*f*) $\int_{\text{thresh}}^{24\text{ Mev}} \sigma(\gamma,n)dE$: 0.026±0.003 Mev barn,
(*g*) $\dfrac{\sum_{\text{thresh}}^{24\text{ Mev}} G\int\sigma_i dE}{\int_{\text{thresh}}^{24\text{ Mev}}\sigma(\gamma,n)dE}$: 75±20%.

The values obtained in the present work are:

(*a*) yield at 22 Mev: $(1.15\pm0.02)\times10^6$ n/g-atom per 100 r,
(*b*) E_{max}: 23.0 Mev,
(*c*) yield at E_{max}: 2.77×10^6 n/g-atom per 100 r,
(*d*) σ_{max}: 7.9 millibarns,
(*e*) $\Gamma_{\frac{1}{2}}$: 3.2 Mev,
(*f*) $\int_{thresh}^{24\ Mev}\sigma(\gamma,n)dE$: 0.022 Mev barn.

ACKNOWLEDGMENTS

The authors would like to thank Mr. E. Buchholz for his assistance in carrying out part of the experiment during the summer of 1960. One of the authors (I.C.G.) acknowledges the financial assistance from the National Research Council and the Physics Department, University of Saskatchewan.

REFERENCES

BARBER, W. C., GEORGE, W. D., and REAGAN, D. D. 1955. Phys. Rev. **98**, 73.
CARVER, J. H. and LOKAN, K. M. 1957. Australian J. Phys. **10**, 312.
COOK, B. C. 1957. Phys. Rev. **106**, 300.
HASLAM, R. N. H., JOHNS, H. E., and HORSLEY, R. J. 1951. Phys. Rev. **82**, 270.
JOHNS, H. E., KATZ, L., DOUGLAS, R. A., and HASLAM, R. N. H. 1950. Phys. Rev. **80**, 1062.
JOHNS, H. E., HORSLEY, R. J., HASLAM, R. N. H., and QUINTON, A. 1951. Phys. Rev. **84**, 856.
KATZ, L. and CAMERON, A. G. W. 1951. Can. J. Phys. **29**, 518.
KATZ, L., HASLAM, R. N. H., HORSLEY, R. J., CAMERON, A. G. W., and MONTALBETTI, R. 1954. Phys. Rev. **95**, 464.
MONTALBETTI, R., KATZ, L., and GOLDEMBERG, J. 1953. Phys. Rev. **91**, 659.
NATHANS, R. and HALPERN, J. 1954. Phys. Rev. **93**, 437.
PENFOLD, A. S. and LEISS, J. E. 1958. Analysis of Photo Cross Sections, Phys. Research Lab., University of Illinois, Champaign, Ill., U.S.A.
PRICE, G. A. and KERST, D. W. 1950. Phys. Rev. **77**, 806.
ROALSVIG, J. P. and HASLAM, R. N. H. 1959. Can. J. Phys. **37**, 499.
ROALSVIG, J. P., HASLAM, R. N. H., and MCKENZIE, D. J. 1959. Can. J. Phys. **37**, 607.
THORSON, I. M. 1957. Thesis, University of Saskatchewan, Saskatoon, Sask.

THE ELECTRICAL CONDUCTIVITY OF GELATIN FILM HUMIDIFIED WITH HEAVY WATER VAPOR[1]

C. D. NIVEN

ABSTRACT

When protons were replaced by deuterium nuclei in gelatin films, by exposure of dry films in 75% relative humidities, the resistance increased very markedly.

At the present time proton migration is believed to account for the electrical conduction of hydrophilic substances. This conduction is much smaller than that of a true semiconductor and Riehl (1956) has suggested that a mechanism depending on the formation of chains of oxygen atoms, each of which has a proton suitably located to move to the next oxygen atom in the chain, explains the migration of the protons in a field.

If protons are responsible for the conduction in these hydrophilic substances, and, as Dr. Ta-You Wu* pointed out to the writer, if every proton taking part in the conduction process is replaced by a deuterium nucleus, the resistance should increase markedly. The work described below was undertaken to determine whether this was so, because if there was no increase in resistance the proton-conduction concept was probably incorrect: on the other hand if there was an increase, this concept was confirmed.

The problem demanded the provision of two comparable atmospheres, one humidified with ordinary water and the other humidified with heavy water. No relative humidity tables were available for use with a wet and dry bulb psychrometer when heavy water vapor instead of ordinary water vapor was in the air. Accordingly some method had to be found to determine the relative humidity from wet and dry readings using heavy water. Since the results of the conductivity measurements are highly dependent on the reliability of this method and on the figures actually used in applying it, some details concerning this calculation may not be out of place.

CALCULATION OF RELATIVE HUMIDITY FROM WET AND DRY BULB READINGS IN AN ATMOSPHERE HUMIDIFIED WITH HEAVY WATER VAPOR

The method was that described by Hougen and Watson in their book *Industrial Chemical Calculations* (1936). The basic assumption is that the heat lost by the humid air must equal that gained by the water in vaporization and superheating: hence an expression is obtained which can be written in the form

[1]Manuscript received January 11, 1961.
Contribution from the Division of Applied Physics, National Research Council, Ottawa, Canada.
Issued as N.R.C. No. 6255.
*Chief, Theoretical Physics Section, Division of Pure Physics, National Research Council of Canada.

$$H = \frac{L_v \times H_w - 6.95D}{L_v + 8.4D}$$

where H is the molal humidity of the air at dry bulb temperature t and wet bulb temperature t_w,

$D = t - t_w$,

L_v = molal heat of vaporization at t_w,

H_w = molal humidity of saturated air at t_w,

and the two constants 6.95 and 8.4 are the heat capacities of air and of water vapor respectively. These, incidentally, can be taken as constant, but the assumption is made that the heat capacity of heavy water vapor is approximately equal to that of ordinary water vapor. As a matter of fact in the present calculation the whole contribution of $8.4D$ to the denominator is less than 3 parts in 1000: accordingly this assumption does not affect the results.

The particular relative humidity at which the heavy water readings were made corresponded to dry and wet bulb readings of 87° and 81° F. (The Fahrenheit degrees enter in because the psychrometer was equipped with Fahrenheit thermometers.) Converting to centigrade $t = 30.5°$, $t_w = 27.2°$, and $D = 3.3°$. From the table drawn up by Whalley (1957) on the thermodynamic properties of heavy water, L_v at temperature 27.2° is 45.278 kilojoules per mole (amended value) or 10816.5 calories per mole, and the vapor pressure at 27.2° is 0.03125 bar. Therefore

$$H_w = \frac{0.03125}{1.01325 - 0.03125} = 0.031828.$$

Hence

$$L_v \times H_w = 344.211$$

and since $6.95D = 23.164$ the numerator in the expression for H is 321.049. The denominator is $10816.5 + 8.4 \times 3.3°$ or 10844.5; hence $H = 0.0296048$. Converting molal humidity to relative humidity by the formula

$$\frac{H}{1+H} \times \frac{1.01325 \times 100}{\text{saturated vapor pressure at } 30.5° \text{ C in bars}}$$

we reach a percentage relative humidity figure of 75.4% from the above quoted psychrometer readings.

For ordinary water vapor a relative humidity of 75% at dry bulb temperature 87° F corresponds to a depression of $6\frac{1}{2}$° F: so this determined the conditions at which readings had to be taken when ordinary water was used.

EXPERIMENTAL METHODS AND RESULTS

Apart from the matter of providing atmospheres which were reliably comparable, there was the problem of providing suitable samples, because previous experience with these gelatin films had indicated that samples did not all act alike. If the investigation was to yield results of any value, several samples

had to be used. Accordingly 13 small pieces of gelatin film about $\frac{3}{4}$ in. $\times \frac{1}{4}$ in. in size were painted with conducting rubber paint on either side so as to give an area of about $\frac{1}{8}$ in. $\times \frac{1}{8}$ in. through which current could pass. They were mounted on a piece of polystyrene carrying 13 pairs of electrodes suitably spaced to take the films: a switching arrangement could connect any particular pair to the megohmmeter. The gelatin resistors were alternately dried out and humidified. The drying was done by putting calcium chloride in the humidifier (Niven 1958) with a sensing element for relative humidity 19%.

Approximate relative humidities were of no use whatever for this investigation; accuracy in reading the psychrometer had to be pushed to the limit but since the sensing elements permitted remarkably good repetition of conditions, psychrometer readings would repeat to one quarter of a degree Fahrenheit in depression values. Before taking the resistance readings the megohmmeter was allowed to heat up, but as soon as the leads to the switching mechanism were connected, readings were taken just as quickly as they could be written down: leaving voltage on the film completely upsets the resistance reading possibly for days (Niven 1959). It seemed preferable to run a series of tests with heavy water and then change to ordinary water rather than to alternate heavy and ordinary tests, because there was then less chance of a residue of the wrong kind of hydrogen nucleus being in the gelatin.

The results are shown in Table I for the 13 different samples: each set of results was taken after the film had been dried out and allowed to come back to its value in the humid atmosphere.

The blanks in Table I for No. 13 arose because the voltage was accidentally left on, thus vitiating the usefulness of these readings. The ratios calculated from the averages show that the replacement of the protons with deuterium nuclei does increase the resistance quite markedly. Just why this is not approximately the same in every case is not clear: certainly the conditions in the humidity cabinet cannot account for this because all of the resistors were exposed to the same ambient humidities.

The average of the ratios in Table I is 1.62; Dr. Wu expected $\sqrt{2}$ or 1.41, according to the following reasoning. The drift (v) of an ion of mass m and charge e in an electric field E is the acceleration

$$\left(\frac{eE}{m}\right) \times \frac{\text{mean free path}}{\text{thermal velocity}} = \frac{eE}{m} \times \frac{\lambda}{\sqrt{(3kT/m)}}$$

where λ is the mean free path of the ion, T is the temperature, and k is Boltzmann's constant. If there are n ions per cc, resistance $= E/nev$ and is therefore proportional to $\sqrt{m}$.

Admittedly the disagreement between theory and experiment may be due to experimental errors. But it is also conceivably possible that it arises from much more fundamental reasons: the idea of collisions due to thermal agitation holds good in the theory proposed by Riehl because these collisions are responsible for making and destroying the chains of water molecules or "canals" down which a proton is passed. These "canals" consist of momentarily correctly oriented water molecules, and the proton is visualized as moving only from

TABLE I

Resistance of gelatin films in air humidified with D_2O and H_2O at 74% relative humidity and 87° F

Resistor	Megohms in D_2O vapor: relative humidity, 75.4%				Average	Megohms in H_2O vapor: relative humidity, 75%					Average	Ratio of averages
1	130	123	118	110	120	73	58	60	55	52.5	60	2
2	17.5	17	17	16.8	17.1	12.2	10.2	10.8	10.5	10.5	11	1.55
3	4.3	4.1	4.1	4.1	4.1	3.0	2.6	2.7	2.63	2.6	2.7	1.52
4	6.8	5.0	5.0	5.4	5.0	3.8	3.2	3.5	3.4	3.4	3.5	1.43
5	3.1	2.8	2.79	2.9	2.9	1.75	1.41	1.55	1.5	1.75	1.59	1.82
6	4.4	4.1	4.1	4.0	4.2	2.9	2.8	2.9	2.82	2.81	2.85	1.50
7	20	19.3	18.8	18.2	19.1	14.8	13.8	13.3	12.8	11.8	13.3	1.44
8	8.4	8.4	8.0	8.2	8.3	5.0	4.1	4.5	4.5	4.4	4.5	1.84
9	6.9	6.95	6.7	6.7	6.8	4.4	3.6	4.0	3.9	4.0	4.0	1.7
10	5.9	6.0	5.7	5.6	5.8	3.9	3.2	3.5	3.4	3.4	3.5	1.66
11	6.6	6.6	6.5	6.6	6.6	5.0	4.5	5.0	4.5	4.6	4.7	1.4
12	3.5	3.5	3.4	3.5	3.5	2.4	2.2	2.35	2.2	2.1	2.3	1.52
13	19	18.5	—	—	—	—	7.1	8.8	9.2	8.6	—	—

one sphere of influence to the next, and releasing a proton from the water molecule to which it arrives and this proton moves on to the next water molecule. The idea of mean free path does not fit into such a model too well unless it be construed as the length of a "canal".

However, the fact that changing the mass of the carrier of positive charge did alter the conductivity supports the proton migration theory of conduction in hydrophilic films.

ACKNOWLEDGMENTS

The author expresses his thanks to Dr. Ta-You Wu of the National Research Council, Ottawa, for suggesting the problem and for several discussions; to Dr. W. P. Bebbington of Du Pont de Nemours & Co. Inc. for pointing out the method to calculate the relative humidity; and to Dr. E. Whalley of the National Research Council, Ottawa, for valuable assistance in applying that method.

REFERENCES

HOUGEN, O. A. and WATSON, K. M. 1936. Industrial chemical calculations, 2nd ed. (John Wiley & Sons, Inc., New York), p. 148.
NIVEN, C. D. 1958. Trans. Faraday Soc. **54**, 441.
——— 1959. Can. J. Phys. **37**, 438.
RIEHL, N. 1956. Naturwissenschaften, **43**, 145.
WHALLEY, E. 1957. Proc. Joint Conference on Thermodynamic and Transport Properties of Fluids, pp. 15–26; or N.R.C. No. 4469.

HALF LIFE, Q_β VALUE, AND γ-RAY SPECTRUM OF La^{143} [1]

K. FRITZE, T. J. KENNETT, AND W. V. PRESTWICH[2]

ABSTRACT

The decay of La^{143} has been investigated. A half life of 14.0±0.1 min and a Q_β value of 3.3±0.1 Mev were found. The γ radiation is weak and the spectrum is rather complex.

Information concerning the high-yield fission-product La^{143} is quite limited. Gest and Edwards (1951) showed by indirect measurement that the lanthanum parent of Ce^{143} has a half life of about 19 min.

CHEMICAL PROCEDURES

In order to obtain La^{143} as highly enriched as possible, it was separated from fission-product barium rather than directly from irradiated uranium. The 13-sec Ba^{143} (Nethaway 1959) together with the longer-lived barium isotopes was isolated as the chloride from which the lanthanum was separated. Two somewhat different methods were used to obtain the lanthanum samples.

Method 1

The irradiated uranium solution (1 ml) was added to 2 ml $BaCl_2$ solution (100 mg Ba) and the $BaCl_2$ precipitated immediately by the fast addition of 15 ml of ice-cold HCl–ether mixture (5+1). The $BaCl_2$ was collected on a 47-mm membrane filter and washed with 5 ml of conc. HCl. (Tracer experiments with Sr^{90} showed that about 15% of it is co-precipitated in the absence of holdback carrier and about 10% if 20 mg of strontium is present.) The $BaCl_2$ was dissolved in 10 ml of hot lanthanum solution (0.5 mg of lanthanum) inside the filter funnel. The lanthanum was precipitated immediately as the hydroxide and filtered over the same membrane as had been used for the $BaCl_2$. The $La(OH)_3$ was "dry" approximately 1 minute after the $BaCl_2$ precipitation. Therefore, the other lanthanum activities which grow in from the 11-min Ba^{142} and the 18-min Ba^{141} were kept at a minimum. After addition of more lanthanum and barium carrier, the $La(OH)_3$ was reprecipitated and dissolved in 10 ml of conc. HNO_3. To remove yttrium which had grown in from the co-precipitated strontium this solution was extracted three times with 10 ml of tributylphosphate. This extraction was found to give a decontamination factor of about 10^4. The nitric acid phase contained about 50% of the purified lanthanum which was eventually converted to $La_2(C_2O_4)_3$. The samples were ready for counting approximately 25 minutes after the end of the irradiation.

Method 2

In his thesis, Nethaway (1959) showed that the exchange of carrier-free radiobarium with pre-precipitated $BaSO_4$ is very fast. To reduce strontium

[1]Manuscript received January 6, 1961.
Contribution from McMaster University, Hamilton, Ont.
[2]Holder of O.R.F.U. Scholarship (1959–1960).

contamination a similar procedure using $BaCl_2$ was developed for the investigation of La^{143}. The irradiated uranium solution was added to a suspension of $BaCl_2$ in 15 ml conc. HCl contained in the funnel of a large membrane filter assembly. Immediately following this, a vacuum was applied to the filter flask and the "dry" $BaCl_2$ washed with 5 ml of conc. HCl. (Separate experiments showed that the co-separation of carrier-free strontium is only 0.1% in this procedure.) Following this the procedure was identical with that of method 1 until after the $La(OH)_3$ reprecipitation. The $La(OH)_3$ was then dissolved in 10 *M* HCl and passed over a small Dowex 1 column. The lanthanum was finally obtained as the oxalate. Counting could usually be started 15 minutes after the irradiation.

Generally samples of 100 or 200 μg of U^{235} in 1 ml of water were irradiated for 10 seconds in a flux of 3×10^{12} n/cm^2 sec using the pneumatic rabbit facility of the McMaster Reactor. The $BaCl_2$ separation was completed 10 to 12 seconds after the end of the irradiation.

HALF LIFE

The La^{143} samples were β counted with a 2×2 in. plastic scintillator. The output of the detector was fed to a DD2 linear amplifier followed by a single-channel pulse-height analyzer. This analyzer was used to select energy regions in the β-ray spectrum. The output was recorded in a 256-channel time analyzer, using a channel width of 1 minute for the first 190 minutes. After the data were read out, the channel width was changed to 10 minutes in order to obtain detailed information on the long-lived background.

In order to minimize the contribution of other components, the single-channel analyzer was used to discriminate against La^{142} and La^{141} and also to eliminate any contribution from the ingrowing Ce^{143}. Three separate experiments employing different energy requirements and chemical procedures were conducted to determine the La^{143} half life by direct measurement. For runs 1 and 2 lower levels were set at 1.0 and 1.5 Mev respectively, while for run 3 a window covering an interval from 2.2 to 3.5 Mev was used. These energy requirements, combined with the chemical enrichment, reduced the contribution of other lanthanum activities to less than 2% of the initial activity. The conditions and results for these three measurements are summarized in Table I.

The third half-life run was analyzed using a least-squares program. The background associated with this run was determined by observing the long-

TABLE I

Summarized results of the La^{143} half-life measurement

Run	Chemistry	Counting	Initial activity (c.p.m.)	Analysis	Half life (min)
1	Method 1	$\beta>1.0$ Mev	49000	Graphically	14.1
2	Method 1	$\beta>1.5$ Mev	16000*	Graphically	14.0
3	Method 2	$2.2>\beta>3.5$ Mev	30000	Least-squares fit	14.0
				Average	14.0±0.1

*Loss of lanthanum during purification.

lived tail of the decay curve and analyzing it by means of a least-squares program. This tail was resolved into 81-minute, 3.7-hour, and constant components. These components were then subtracted from the original data. The contribution of the three background components were 81-minute La^{142}, 1.3%; 3.7-hour La^{141}, 0.07%; and room background 0.07% of the initial activity. The corrected data were then analyzed for a region covering 10 half lives (140 channels). The half life was found to be 14.03 min with a standard deviation of 0.03 min.

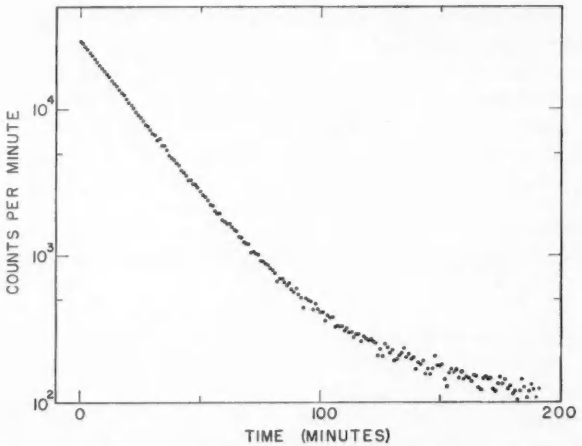

FIG. 1. The decay curve of La^{143} obtained in run 3. In this case only β rays whose energy fell between 2.2 and 3.5 Mev were recorded. The contribution from other activities amounted to 1.5% of the original counting rate. After this small correction was made, a least-squares analysis of the data from initial counting until 140 minutes gave a value of 14.03±0.03 min.

In view of the marked discrepancy between the half life reported here and the previously accepted value of 19 min it was decided to perform a similar experiment to that of Gest and Edwards. The Ce^{143} was separated from aliquots at 6.5, 13.5, 20.5, 27.5, 171.5, and 215.5 minutes after the preparation of a stock solution of fission-product lanthanum using the Ce^{4+}-hexone extraction (Glendenin *et al.* 1955). This method, which is described in more detail by Gest and Edwards (1951), gave a half-life value of about 12 min. This value is in agreement with the direct measurement. Finally it can be said that the 15-min rare-earth activity observed by Hahn and Strassmann (1943) undoubtedly must have been La^{143}.

β ENERGY AND Q VALUE

To obtain the β-ray spectrum of La^{143} a 2×2 in. plastic scintillator (Nuclear Enterprise NE 102) coupled to a 9536B EMI photomultiplier was used. The output of this detector was fed to a 256-channel pulse-height analyzer. The data stored in the analyzer were transcribed on paper tape in order that computation for a Fermi analysis of the spectrum might be easily performed.

The La^{142} source was prepared using the $BaCl_2$ exchange reaction (method 2) and 3 mg of lanthanum carrier. The final step in source preparation consisted of ashing the oxalate precipitate and mounting the La_2O_3 on a thin mylar film. This source was counted 18 minutes after the irradiation for a 20-minute period.

The spectrometer was calibrated before and after the analysis of the La^{143} sample using Sr^{90}–Y^{90} (2.26 Mev), Ru^{106}–Rh^{106} (3.53 Mev), Cl^{38} (4.9 Mev), and the Compton edges of Cs^{137} and Zn^{65}. Fermi–Kurie plots were obtained and the end points determined. The calibration indicated good linearity of the spectrometer. The end point for La^{143} was found to correspond to an energy of 3.30 ± 0.08 Mev.

An experiment conducted to determine the average number of γ rays associated with the decay of La^{143} gave a value of less than $\frac{1}{2}$. This low γ-ray yield suggests that the end point observed in the β-ray spectrum, 3.3 Mev, probably corresponds to the Q value for La^{143}. This value is not inconsistent with the decay-energy systematics in this mass region.

La^{143} γ-RAY SPECTRUM

The characteristic γ radiation from La^{143} was investigated using scintillation spectroscopy. An unshielded 3×3 in. NaI (Tl) detector was employed in conjunction with a double delay-line amplifier and a 256-channel analyzer. As mentioned above, this particular nuclide was found to be a relatively weak γ-ray emitter, so that both the contribution from La^{142} and ingrowing Ce^{143} was expected to be important. The contribution from La^{141} is negligible. Thus in order to obtain the pure La^{143} γ-ray spectrum, the spectral contribution of $La^{142}+Ce^{143}$ had to be determined and removed. To reduce the effects of β radiation a 1 g/cm^2 polyethylene absorber was placed on the face of the crystal.

A source was prepared using method 2 and the lanthanum oxalate sample mounted directly on the polyethylene absorber. The initial counting rate was $\sim$ 3000 counts/sec and resulted in a dead time of about 4% in the analyzer. From previous experience, rates of this order were known to produce no distortion in the data. Spectra were obtained beginning at 14 minutes, 162 minutes, and 18.3 hours after the end of the irradiation, for counting periods of 8 minutes, 32 minutes, and 1 hour respectively. The first spectrum was composed of La^{143} (14.0 minutes), La^{142} (81 minutes), and the Ce^{143} (33 hours) which had partially grown in. The second spectrum, taken after the complete decay of La^{143}, consisted only of La^{142} and the Ce^{143} which is fully grown in at this time. The third spectrum was solely that of Ce^{143}. The spectra were read out on tape, allowing reduction of the data using a Bendix G-15 computer. From a knowledge of the counting times, and the half lives involved, the interfering $La^{142}+Ce^{143}$ components were removed. The contribution of the long-lived activities was found to be 20%. The resultant La^{143} spectrum is shown in Fig. 2.

The energy calibration was obtained both with standard sources and known lines in the $La^{142}+Ce^{143}$ spectra as given by Schuman, Turk, and Heath (1958)

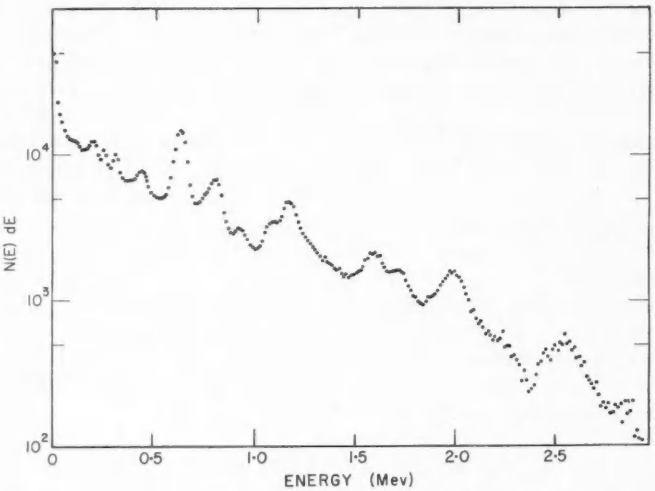

FIG. 2. The γ-ray spectrum of La^{143}. The spectrum shown has been corrected for the contribution from La^{142} and Ce^{143}. The region around 0.300 Mev is uncertain because of the strong interference caused by the 0.290-Mev line in Ce^{143}.

and Martin *et al.* (1956). Table II lists the observed lines in order of increasing energy. These intensities have been corrected for detection and photofraction efficiency of the NaI (Tl) crystal using the results of Miller, Reynolds, and Snow (1957).

The 0.265- and 0.320-Mev lines shown in Fig. 2 are not given in Table II

TABLE II

γ-Ray lines for La^{143}

Energy (Mev)	Relative intensity	Energy (Mev)	Relative intensity
0.200±0.01	0.08*	1.58±0.04	0.28
0.440±0.02	0.13	1.70±0.04	0.19
0.625±0.01	1.0†	1.98±0.03	0.35
0.800±0.01	0.44	2.22±0.03	0.06‡
0.915±0.02	0.08	2.46±0.03	0.13
1.07±0.04	0.26	2.56±0.03	0.27
1.17±0.02	0.57	2.85±0.04	0.15

*The shape of this line indicates that it is real; however, some contribution from backscattering is to be expected.
†Normalized to unity.
‡This line may possibly arise from the summing of the 0.625- and the 1.58-Mev transitions.

because their existence is somewhat in doubt. This ambiguity arises from interference of the intense 0.290-Mev line in Ce^{143}. No similar problem arose in the subtraction of the La^{142} spectrum.

ACKNOWLEDGMENTS

The authors wish to thank the National Research Council for its financial support. One of us (W.V.P.) acknowledges the assistance given by O.R.F.U.

REFERENCES

GEST, H. and EDWARDS, R. R. 1951. National nuclear energy series, Plutonium Project Record, IV, **9** (McGraw-Hill Book Co., Inc., New York), p. 1144.
GLENDENIN, L. E., FLYNN, K. F., BUCHANAN, R. F., and STEINBERG, E. P. 1955. Anal. Chem. **27**, 59.
HAHN, O. and STRASSMANN, F. 1943. Naturwiss. **31**, 499.
MARTIN, D. W., BRICE, M. K., CORK, J. M., and BURSON, S. B. 1956. Phys. Rev. **101**, 182.
MILLER, W. F., REYNOLDS, J., and SNOW, W. J. 1957. Rev. Sci. Instr. **28**, 717.
NETHAWAY, D. R. 1959. Ph.D. Thesis, Dept. of Chemistry, Washington University, St. Louis, Mo.
SCHUMAN, R. P., TURK, E. H., and HEATH, R. L. 1958. Bull. Am. Phys. Soc. **3**, No. 5, 315.

NOTE ADDED IN PROOF

Recent measurements in this laboratory indicate that the half life of La^{142} is 92 min. In view of this discrepancy in the La^{142} half life, all the data presented in this paper have been recalculated. It was found that this change in the La^{142} half life did not alter any of the data quoted for La^{143} within the assigned errors.

THE EFFECTIVE DIRECTIONAL SENSITIVITY OF COSMIC-RAY NEUTRON MONITORS[1]

S. M. LAPOINTE[2] AND D. C. ROSE

ABSTRACT

The direction of maximum sensitivity of a neutron monitor is calculated numerically for a set of points on the same geomagnetic meridian but extending in latitude from the equator to the pole. This leads to two master curves, one for the longitude, the other for the latitude of this direction. From these curves this direction is obtained in geographic co-ordinates for some 20 cosmic-ray stations. The method of calculation is described taking into account atmospheric absorption and the energy spectrum of the incident particles. The aperture of the sensitive cone, or source width, is also calculated. Finally the accuracy of the results is discussed and the application of the concept of effective direction is described.

1. INTRODUCTION

Neutron monitors, usually consisting of a layer of paraffin surrounding neutron counters, then a layer of lead, and then an outer layer of paraffin, have been used for several years as detectors of cosmic rays at ground level. They are particularly important in studying cosmic-ray intensity variations, because atmospheric effects can be eliminated by a simple correction for changes in the barometric pressure.

In problems relating to intensity changes due to solar activity or due to the earth's rotation it is desirable to know the direction of travel of the particles being studied at some distance away from the earth, that is, before they are deflected by the earth's magnetic field. It is also important to know whether a detector at ground level sensitive locally to particles in all directions, and accepting all particles above a minimum energy, can in fact be said to be measuring incoming particles from a unique direction in space or at least an effective direction that has some meaning in examining intensity variations that may be related to directional anisotropies in space.

The passage of the particles through the atmosphere, interactions with air nuclei, and the generation of secondaries which result in a strong collimating effect on the particles detected, is reasonably well understood and the behavior of charged particles in the earth's magnetic field has been investigated sufficiently to give reasonably accurate information on the above problem. In this paper we are reporting calculations based on available information which will give an effective direction of the primary particles responsible for the intensity recorded by a conventional neutron monitor.

Actually a neutron monitor at sea level responds to primary particles in a wide range of primary particle energies, from about 1 Bev upwards. It also detects particles impinging on the top of the earth's atmosphere from a wide

[1]Manuscript received February 6, 1961.
Contribution from the Division of Pure Physics, National Research Council, Ottawa, Canada.
Issued as N.R.C. No. 6269.
[2]Department of Physics, University of Montreal, Montreal, Que.

range of directions. Primary particles of different energies and different impact directions on earth come from different asymptotic directions far away from the earth ($\gtrsim$10 earth radii) outside the deflecting geomagnetic field. The neutron monitor's sensitivity is different for different primary energies or different impact directions on earth. From available information a weight can be given to each asymptotic direction, using the known energy spectrum of the incident radiation. In this manner an effective direction can be calculated for each neutron monitor station on earth. The concept of effective direction was introduced by Dorman (1957). It has been applied to the determination of onset times of Forbush-type decreases by Fenton, McCracken, Rose, and Wilson (1959) and the results of the present calculation have been used by Rose and Lapointe (1961) in the analysis of the recovery period after a series of Forbush-type decreases.

In what follows, a method for calculating numerically the effective direction of a neutron monitor is described in detail taking various factors into account. The calculation was performed for neutron monitor stations at all geomagnetic latitudes between the equator and the pole by steps of 5° or 10°. The results are presented in the form of a curve. From this master curve the effective direction can be obtained easily and rapidly for a neutron monitor in any geographic location.

Finally the accuracy of the results is discussed and the application of the concept of effective direction is described.

2. THE METHOD OF CALCULATION

The direction of the particle's trajectory at infinity can be specified by two angles: the asymptotic latitude ϕ_N and the asymptotic longitude ψ_E (Brunberg 1953). The dependence of these angles on energy, impact latitude (geomagnetic), and impact direction, already published, has been used (Jory (1956) and Lüst (1957) for low energies; Brunberg (1953) and Brunberg and Dattner (1953) for high energies). The problem then is to establish an effective weight at the detector for each energy and each zenith direction, that is, the zenith direction at impact on the atmosphere.

(a) Zenithal Weights

The mechanism giving rise to decreasing detector sensitivity with increasing zenith angle at the point of impact is atmospheric absorption. It has been experimentally established by Simpson, Fonger, and Treiman (1953), and by Simpson and Fagot (1953) that the counting rate in a neutron pile monitor decreases exponentially with increasing atmospheric depth. The attenuation length for the secondary nucleonic cascade in the atmosphere used in the present calculation is 150 g/cm^2. This leads to a zenithal weight

$$\exp\left[-\frac{h}{L}\left(\frac{1}{\cos Z}-1\right)\right]$$

neglecting the curvature of the earth where h is the thickness of the earth's atmosphere $\sim$1000 g/cm^2, L is the attenuation length 150 g/cm^2, and Z is the zenith angle.

The size of the solid angle at a given zenith angle must also be taken into account. The method introduced by Brunberg and Dattner (1954) was used here. Namely, the sky above the observer is divided first in annular regions with boundaries $Z = n\times 8°$ ($n = 0, 1, 2, 3, 4, 5, 6$). Then these rings of equal widths are cut in four quadrants N, S, E, and W by two appropriate perpendicular planes. In the N quadrant, for instance, there are six regions with solid angle proportional to $\sin Z_m$, where $Z_m = (n+\frac{1}{2})\times 8°$, ($n = 0, 1, 2, 3, 4, 5$).

The procedure followed to construct a histogram for asymptotic longitude is then the following: particles of a single fixed energy are now considered. The asymptotic longitudes are taken from the references above for particles of that energy having impact directions in the N–S plane and making zenith angles of 0°, 8°, 16°, 24°, 32°, 40°, and 48° N. Above 48° the weight is sufficiently low to neglect the larger zenith angles. These asymptotic longitudes are marked on the abscissa of the N histogram. Between the marks for 0° and 8° N a rectangular surface is plotted on the histogram with area equal to

$$\sin 4° \exp\left[-\frac{h}{L}\left(\frac{1}{\cos 4°}-1\right)\right].$$

In other words, asymptotic longitudes for impact directions between zenith angle 0° and 8° N are given equal weights totalling to the weight of the region centered on 4° N and so on for other zenithal regions. The same thing is done for the S, E, and W quadrants. Then all these four histograms are added together to give the final histogram for asymptotic longitude for incident primary particles of that chosen energy. The same thing is done for asymptotic latitude.

(b) Energy Weights

The histograms in Section (*a*) give an answer to the following question: if primary cosmic-ray particles of a given energy fall isotropically on a station, from what direction do the most efficient particles come? Or, in other words, what is the direction of maximum sensitivity of the neutron monitor for particles of that energy?

Now a further question must be answered: what is the direction of maximum sensitivity of a given neutron monitor with respect to a mixed beam containing particles of many energies? Obviously, many histograms of the type described in Section (*a*) must be obtained for many different energies; each one must be multiplied by an appropriate energy weight representing the abundance of particles of that energy in the incident beam. Then all the resulting histograms added together give the final one.

However, the energy weight is not given simply by the relative abundance of the various energies or, in other words, the differential energy spectrum of the incident beam. It must be remembered that one is dealing here with a detector at sea level and that one is looking for the direction in space which gives rise to largest counting rate in such a detector. Therefore, the energy weight is simply the primary differential spectrum times the specific yield function (Simpson, Fonger, and Treiman 1953).

Equivalently one can use the formalism of the coupling constant (Dorman 1957) and for practical reasons this will be done in what follows. Following Dorman (1957) one can write the following equations. The total counting rate at geomagnetic latitude λ and atmospheric depth h_0 is:

$$N_\lambda(h_0) = \int_{\epsilon_\lambda \min}^{\infty} D(\epsilon) m(\epsilon, h_0) d\epsilon$$

where $\epsilon_\lambda \min$ is the geomagnetic threshold energy, $D(\epsilon)$ is the differential energy spectrum of the primary cosmic rays, and $m(\epsilon, h_0)$ is the multiplicity or specific yield function at depth h_0. Considering fixed atmospheric and geomagnetic conditions the intensity variation is given by:

$$\delta N_\lambda(h_0) = \int_{\epsilon_\lambda \min}^{\infty} \delta D(\epsilon) m(\epsilon, h_0) d\epsilon$$

and obviously the relative variation is:

$$\frac{\delta N_\lambda(h_0)}{N_\lambda(h_0)} = \int_{\epsilon_\lambda \min}^{\infty} \frac{\delta D(\epsilon)}{D(\epsilon)} \frac{m(\epsilon, h_0) D(\epsilon)}{N_\lambda(h_0)} d\epsilon$$

$$= \int_{\epsilon_\lambda \min}^{\infty} \frac{\delta D(\epsilon)}{D(\epsilon)} W_\lambda(\epsilon, h_0) d\epsilon.$$

The last equation defines the coupling constant $W_\lambda(\epsilon, h_0)$. In this formalism, the effective angle described above can obviously be defined:

$$\bar{\phi}_\lambda = \frac{\int_{\epsilon_\lambda \min}^{\infty} \phi_\lambda(\epsilon) W_\lambda(\epsilon, h_0) \frac{\delta D(\epsilon)}{D(\epsilon)} d\epsilon}{\int_{\epsilon_\lambda \min}^{\infty} W_\lambda(\epsilon, h_0) \frac{\delta D(\epsilon)}{D(\epsilon)} d\epsilon}.$$

This represents the effective angle of a given variation in the intensity of the primary particles $\delta D(\epsilon)/D(\epsilon)$. The present calculation is carried out for an intensity variation having the same spectrum as the ordinary cosmic rays, that is, a power law spectrum; this is the case, for instance, of the Forbush decrease. Therefore, one can write $\delta D(\epsilon) = C D(\epsilon)$ where C is a constant, and

$$\bar{\phi}_\lambda = \frac{\int_{\epsilon_\lambda \min}^{\infty} \phi_\lambda(\epsilon) W_\lambda(\epsilon, h_0) d\epsilon}{\int_{\epsilon_\lambda \min}^{\infty} W_\lambda(\epsilon, h_0) d\epsilon}.$$

In the present paper, $\phi(\epsilon)$ is not a single angle but a whole histogram. However, this makes no difference to the above expression when it is integrated numerically in the manner described below. A point of practical interest is the following: an examination of Dorman's curves for the coupling constant for neutron monitors shows that, though it is a function of latitude, its variation with energy is the same for different latitudes. To a close approximation in this application one can write:

$$\frac{W_\lambda(\epsilon, h_0)}{W_{80°}(\epsilon, h_0)} = C_\lambda(h_0)$$

where $C_\lambda(h_0)$ varies only with latitude. Therefore,

$$\bar{\phi}_\lambda = \frac{\int_{\epsilon_\lambda \min}^{\infty} \phi_\lambda(\epsilon) W_{80°}(\epsilon, h_0) d\epsilon}{\int_{\epsilon_\lambda \min}^{\infty} W_{80°}(\epsilon, h_0) d\epsilon}.$$

The coupling constant for the neutron component at sea level used by Dorman was derived from the measurements of Rose and Katzman (1956). To perform the above integration the energy axis is divided in intervals of various lengths. The interval is chosen of such a length that the asymptotic angle over that length does not vary too much. Then the energy in the middle of each interval is chosen to work out a zenithal histogram; that histogram is then multiplied by the following energy weight: length of the energy interval times the value of the coupling constant at the middle energy. This is done for energies extending from a practical cut-off, where particles from more than half the directions are admitted, up to energies where an additional interval adds a negligible weight to those already accumulated. All the resulting weighted histograms are added together to give the final one.

From this final histogram the mean effective angle is calculated, and also the root mean square deviation giving a measure of the width of the sensitivity aperture of the neutron monitor.

3. RESULTS

The above described calculation has been performed for geomagnetic latitudes: 0°, 10°, 20°, 25°, 30°, 35°, 40°, 45°, 50°, 55°, 60°, 65°, 70°, 75°, 80°, 90°. For 25°, 35°, and 75°, interpolation of the raw data had to be used. The results are given in the form of two curves. Figure 1 presents the longitude shift of the source to the east of the observer's meridian ψ_E as a function of the geomagnetic latitude of his station. Figure 2 shows the northern latitude of the source ϕ_N. Both asymptotic angles ψ_E and ϕ_N are expressed in geomagnetic co-ordinates. To find the asymptotic effective angle at a given cosmic-ray station one proceeds as follows: the longitude shift ψ_E read off the master curve is added to the station's geomagnetic longitude φ_m. This, together with ϕ_N read off the second master curve, gives the source's geomagnetic co-ordinates. Using the Smithsonian Physical Tables one can convert these to geographic co-ordinates. This has been done for some 20 cosmic-ray stations and the result is shown in Table I. The present calculation agrees within 1 or 2 degrees with the four longitude shifts calculated independently by Fenton, McCracken, Rose, and Wilson (1959).

The root mean square deviation σ of the final histogram of the process is plotted in Fig. 3 for the longitude shift ψ_E, and in Fig. 4 for the latitude ϕ_N,

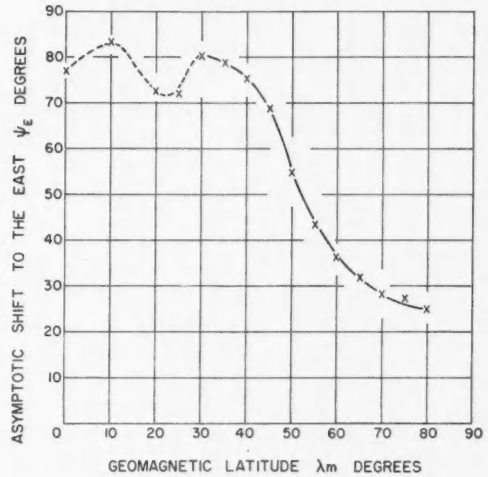

FIG. 1. East longitude ψ_E of the effective direction of the monitor vs. station latitude, both in geomagnetic co-ordinates. Station longitude taken to be 0°.

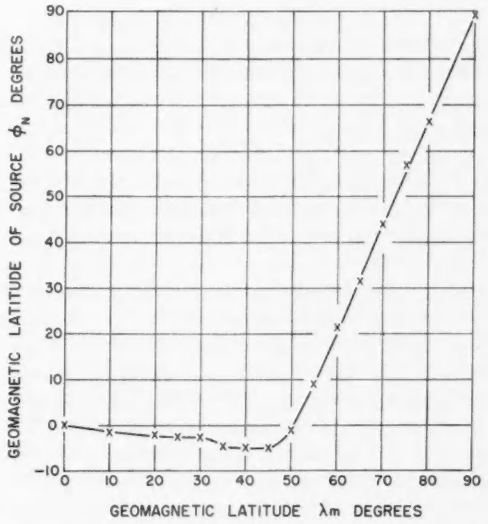

FIG. 2. Latitude ϕ_N of the effective direction of the monitor vs. station latitude, both in geomagnetic co-ordinates.

TABLE I

The first two columns give the station's location, the last two columns give the direction of maximum sensitivity of a neutron monitor there

Station	Geographic co-ordinate of station		Geographic co-ordinate of direction of maximum sensitivity	
	Lat.	Long.	Lat.	Long.
Sydney	−34	151 E	0	230 E
Berkeley	38	122 W	−16	300 E
Climax	39	106 W	−14	310 E
Mt. Wellington	−43	147 E	−4	205 E
Chicago	42	88 W	0	315 E
Ottawa	45	76 W	3	320 E
Deep River	46	78 W	6	320 E
Sulphur Mt.	51	116 W	5	272 E
College	65	148 W	28	228 E
Churchill	59	94 W	31	285 E
Uppsala	60	18 E	27	72 E
Mawson	−68	63 E	−44	70 E
Zugspitze	47	11 E	7	85 E
Munich	48	12 E	8	82 E
Herstmonceux	51	0	14	60 E
Leeds	54	2 W	20	53 E
Ellsworth	−78	41 W	−44	343 E
Mt. Washington	44	71 W	2	328 E
Rome	42	13 E	6	95 E
Pic du Midi	43	0	5	78 E
Mt. Norikura	36	138 E	−5	209 E
Lincoln	41	97 W	−10	310 E
Resolute	75	96 W	64	263 E
Thule	77	69 W	74–84	—

both as a function of station geomagnetic latitude λ_m. This deviation σ gives an idea both of the uncertainty of the calculated mean effective angles and also of the width of the sensitive aperture of the neutron monitor.

4. ACCURACY

Unfortunately, it is not possible to estimate accurately the uncertainty in these calculations. Therefore, some factors affecting the uncertainty will be discussed here in an attempt to give an idea of the magnitude of the possible errors.

(*a*) The accuracy of the fundamental data used, namely, the asymptotic directions of cosmic-ray trajectories as a function of energy and geomagnetic latitude, are estimated by Brunberg (1953) not to exceed 2° to 3°. On the other hand the agreement between the experimental points of Brunberg and Dattner and the calculated ones of Jory and Lüst is also within about the same limits of a few degrees. Therefore, in the present calculation, all the angles were read to the nearest 5°: histograms were, therefore, obtained for 5° intervals. This is likely to be as good as the basic data. In averaging over a range of angles wide compared to 5°, the inaccuracy on the resulting average angle is probably less than the one on individual points. The smoothness (within 1°) of the curves in Figs. 1 and 2 seems to corroborate this argument.

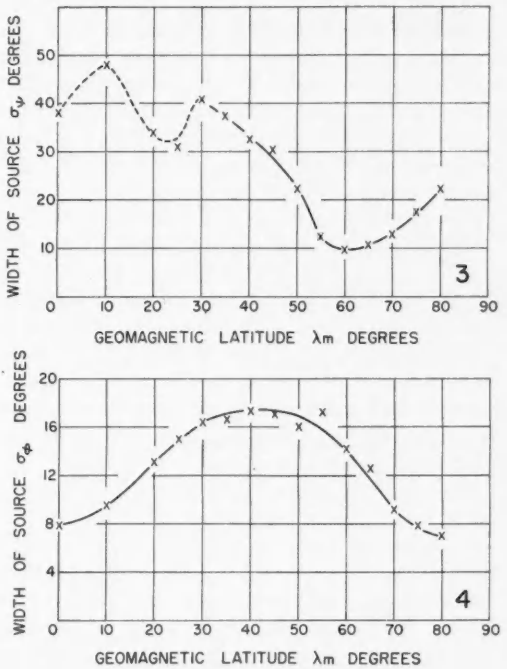

FIG. 3. Source width in longitude vs. station latitude, both in geomagnetic co-ordinates.
FIG. 4. Source width in latitude vs. station latitude, both in geomagnetic co-ordinates.

(*b*) The shape of the curve at low latitudes in Fig. 1 where there is a double reverse in curvature deserves special comment. The variations in ψ_E in this region amount to between 3° and 7°. All the neighboring points in that region have been treated in the same fashion, and therefore, if any, they should all bear the same bias and not vary up and down. Perhaps, therefore, this fluctuation is significant. The only test that can be applied in the present method is to break up an energy interval in a critical region (usually low energy where the asymptotic angles change rapidly) into two or three narrower intervals and with this to calculate the new mean angle in such a finer grid. This was tried in the low latitude region and it is felt that a further subdivision would not bring about a 1° change. If these variations are not significant the reason should probably be sought elsewhere, such as in the accuracy of the basic data, cut-off values, the approximation in the use of a single attenuation length, or perhaps other factors more critical in this region of higher magnetic field. It should be noted that the r.m.s. deviation plotted in Fig. 3 has its largest value at low latitudes, therefore, indicating greatest uncertainty in that region. This might explain the irregular curve. However, the r.m.s.

deviation curve has itself the same irregularity in that region, indicating that the width of the sensitive cone fluctuates. This fluctuation in source width is quite real in regard to these calculations but its physical significance is not clear.

(*c*) Another source of error is the attenuation length L used in the exponential term of the azimuthal weight. The same value of 150 g/cm^2 was used for all stations. However, it is well known that this length varies with altitude and latitude. This constant value can only be considered a rough and practical average value.

5. DISCUSSION

In conclusion, perhaps the more exact meaning of effective direction can be reviewed in the light of its derivation above. The method of calculation described here assumes an isotropic beam (at least within a minimum cone around the station's vertical) falling on the top of the atmosphere and having the same differential energy spectrum as ordinary cosmic rays, that is, an inverse power law. Then effective direction is that direction from which the particles are coming which are preponderant in producing the counting rate. It is obvious that particle trajectories from other directions could be absent without affecting the counting rate very much. In other words, if the beam is isotropic, by and large the particles counted are those coming from the effective direction. If an anisotropic variation comes from the effective direction it will be recorded with maximum sensitivity. But the reverse to this last statement is only probably true: that is, a recorded intensity variation only probably comes from the effective direction. Given any recorded counting rate variation it can be caused by a primary variation taking place in the effective direction, or by a larger one not in the effective direction. But if the intensity variation recorded is of short duration, for instance a peak above the neighboring background in the intensity–time curve, and if it occurs at many stations, and above all if all these stations' peaks and effective directions point at the same direction in space for the source, then it is very probably meaningful.

REFERENCES

BRUNBERG, E. A. 1953. Tellus, **5**, 135.
BRUNBERG, E. A. and DATTNER, A. 1953. Tellus, **5**, 269.
——— 1954. Tellus, **6**, 73.
DORMAN, L. I. 1957. Cosmic ray variations (State Publishing House for Technical and Theoretical Literature, Moscow. Translation by United States Technical Documents Liaison Office).
FENTON, A. G., MCCRACKEN, K. G., ROSE, D. C., and WILSON, B. G. 1959. Can. J. Phys. **37**, 970.
JORY, F. S. 1956. Phys. Rev. **103**, 1068.
LÜST, R. 1957. Phys. Rev. **105**, 1827.
ROSE, D. C. and KATZMAN, J. 1956. Can. J. Phys. **34**, 1.
ROSE, D. C. and LAPOINTE, S. M. 1961. Can. J. Phys. **39**, 239.
SIMPSON, J. A. and FAGOT, W. C. 1953. Phys. Rev. **90**, 1068.
SIMPSON, J. A., FONGER, W., and TREIMAN, S. B. 1953. Phys. Rev. **90**, 934.
SMITHSONIAN PHYSICAL TABLES. 1954. 9th revised ed.

MODELS OF AURORAL IONIZATION

PART I. AURORAL IONIZATION MODELS AND THEIR RADIO-REFLECTION CHARACTERISTICS[1]

D. R. MOORCROFT

ABSTRACT

Although radio observations of aurora contain information about the nature of the reflecting ionization, the use of dissimilar models of auroral ionization has led different workers to widely differing conclusions. In this paper several general models of auroral ionization are developed. By considering the ionization as an assembly of individual scatterers, it has been possible to include a unified treatment of both weak scattering and critical reflection. This treatment should provide a basis for resolving some of the difficulties in the interpretation of auroral radio observations. In a second paper the available experimental evidence is examined in the light of this theoretical treatment.

INTRODUCTION

Over the past thirteen years radar has been used extensively to study auroral ionization, but the distribution and density of the ionization responsible for these radar reflections is still the subject of much speculation. Perhaps the most fundamental question to be resolved is that of the density of this ionization. In terms of radar reflection this is a question of the relative importance of two basically different reflection mechanisms: critical reflection and weak scattering. The first of these mechanisms (sometimes known as ionospheric-type reflection) was proposed originally by Lovell, Clegg, and Ellyett (1947) to explain echoes observed by them on 46 Mc/s. More recently, other workers (Forsyth 1953; Bullough and Kaiser 1954; Kaiser 1956; Forsyth and Vogan 1957; Collins and Forsyth 1959) have suggested that critical reflection is important in explaining auroral echoes, at least on lower frequencies. Some of the workers (Herlofson 1947; Aspinall and Hawkins 1950; Booker, Gartlein, and Nichols 1955; Booker 1956; Presnell *et al.* 1959; Flood 1960) believe that all echoes are due to irregularities of small strength (i.e. electron density) in the normal ionosphere, the mechanism of reflection being partial reflection from these irregularities. Also in doubt are the size of the irregularities and the degree of elongation along the magnetic field. Estimates of the radius of the irregularities range from a fraction of a meter (Booker 1956) to 100 meters (Kaiser 1956); estimates of their elongation range from an axial ratio of 4:1 (Forsyth and Vogan 1957) to 40:1 (Booker 1956). Part of the reason for this controversy is the lack of a sufficiently general model with which the experimental results may be compared. The most developed theory of auroral reflections (Booker 1956) considers only weak scattering. While many authors have discussed the general characteristics of critical reflection, there is no detailed theory for the reflection of radio waves from critically reflecting

[1]Manuscript received December 14, 1960.
Contribution from the Institute of Upper Atmospheric Physics, University of Saskatchewan, Saskatoon, Saskatchewan.

irregularities, nor of the transition from critical reflection to weak scattering that will take place with increasing radio frequency. A satisfactory theory should provide a thorough and unambiguous basis from which to examine the existing experimental data, and should suggest still other types of experiments needed to prove the existence of particular models of auroral ionization.

The purpose of this paper is to develop a general theory which encompasses both critical reflection and weak scattering, and includes several different distributions in the size of the scatterers. The results of the theoretical development are examined in Part II (Moorcroft 1961) in the light of the available observational evidence.

In order to include several different scattering mechanisms, a rather versatile model is required. One quite useful method has been used by Booker (1956) in the development of his model of auroral ionization. He described the distribution of the ionization in terms of an autocorrelation function associated with variations in the dielectric constant (or electron density), and derived the scattered field in terms of the parameters of this autocorrelation function. This approach excludes consideration of critical reflections, and is therefore not satisfactory for a general treatment of reflection processes. In this paper, a family of models, consisting of assemblies of individual, specified scatterers is considered. The scattered field from the assembly of scatterers is obtained in terms of the scattered field from each of the individual scatterers. This permits the inclusion of critical reflections and allows the model to be more directly related to the physical situations which are believed to exist at auroral levels. During the development of the models a considerable number of approximations are introduced. These approximations can be justified because they permit theoretical consideration of otherwise intractable problems, and the results based on the approximations are still of greater precision than the observational material with which they are to be compared.

All the proposed models are assumed to consist of assemblies of scatterers having an electron density distribution

$$N = N_0 e^{-[(\xi^2+\eta)^2/a^2+(\zeta^2/c^2)]}, \tag{1}$$

where $a < c$, ξ, η, and ζ are spatial co-ordinates in meters, and N is the electron number density in m^{-3}. These may be called prolate-spheroidal, Gaussian distributions; for convenience they will be called "gaussoids" in this paper. This distribution can arise by diffusion from a point concentration of ionization in the presence of a magnetic field; this process may occur at auroral heights in the ionosphere.

THE SCATTERED FIELD FROM A GAUSSOID

The generalized behavior of a gaussoid in the presence of an electromagnetic wave is very difficult to determine. Several limiting situations can be considered, for each of which a different, special technique is available. This approach is analogous to the very successful treatments of radio-wave reflection from meteoric ionization (Eshleman 1952; Kaiser and Closs 1952). The limiting situations, amenable to theoretical treatment are weak scattering, critical reflection (ray theory), and small, strong scatterers.

Weak Scattering

If the electron density is sufficiently small or the frequency of the electromagnetic wave sufficiently high, the wave is essentially unattenuated by the ionization, and the Born approximation is valid. This implies that the electrons are far enough apart to be unaffected significantly by reradiated fields. Only the effect of the field of the incident wave needs to be considered. The scattered field from such an assembly of electrons is given by the sum of the fields reradiated by each electron separately, taking into account their relative phases. When these approximations are valid the reflection is said to be due to weak scattering and the resulting treatment is called scatter theory. If $N(\xi, \eta, \zeta)$ is the electron density in m^{-3}, (l_1, m_1, n_1) the direction cosines specifying the direction of the incident wave normal, (l_2, m_2, n_2) the direction cosines specifying the direction to the field point, $k=2\pi/\lambda$ the wave number in m^{-1}, E_1 the incident field, r_0 the distance to the field point from the origin of the co-ordinate system (ξ, η, ζ), assumed to be within the scattering volume, α the angle between $\bar{\mathbf{E}}_1$ and $\bar{\mathbf{r}}_0$, and $r_e=\mu_0 e^2/4\pi m$ the classical electron radius, the scattered field E_s at the field point is

$$(2) \qquad E_s = \frac{r_e \sin\alpha E_1}{r_0} e^{ikr_0} \iiint_V N(\xi, \eta, \zeta) e^{ik[(l_1-l_2)\xi+(m_1-m_2)\eta+(n_1-n_2)\zeta]} d\xi d\eta d\zeta.$$

It is assumed that the scattering volume has dimensions small compared to r_0. Substituting (1) in (2) gives for the scattered field from a gaussoid

$$(3) \qquad E_s = \frac{r_e \sin\alpha E_1 \pi^{3/2}}{r_0} a^2 c N_0 e^{-(k^2/4)[a^2(l_1-l_2)^2+a^2(m_1-m_2)^2+c^2(n_1-n_2)^2]}.$$

A scattering coefficient σ, defined as the power scattered per unit solid angle, per unit incident power density, is given by

$$(4) \qquad \sigma = r^2(E_s^2/E_1^2).$$

The total number of electrons in a gaussoid is given by

$$(5) \qquad q = N_0 a^2 c \pi^{3/2} = N_0 a^3 h \pi^{3/2}.$$

It follows that the scattering coefficient can be expressed by means of (3) as

$$(6) \qquad \sigma = r_e^2 q^2 \sin^2\alpha e^{-(a^2k^2/2)[(l_1-l_2)^2+(m_1-m_2)^2+h^2(n_1-n_2)^2]},$$

where $h=c/a$ is the axial ratio of the distribution. For the case of backscattering

$$(7) \qquad \sigma = r_e^2 q^2 e^{-2a^2k^2(\cos^2\phi+h^2\sin^2\phi)},$$

where ϕ is the angle that the z-axis of the distribution makes with the incident wave front. This is the case of particular interest for observations of radar reflections from aurora.

Critical Reflections (Ray Theory)

If the electron density N_0 increases, or the frequency of the radio waves decreases, until the index of refraction of the medium becomes negative, the incident wave no longer passes through the scatterer. In an ionized medium the index of refraction is related to the electron density by the expression

$$\mu^2 = 1-(4\pi r_e/k^2)N. \tag{8}$$

The index of refraction becomes zero when

$$k^2 = 4\pi r_e N_c. \tag{9}$$

If effects due to collisions are ignored, it can be shown that at normal incidence effectively all of the energy in the wave is reflected at the surface defined by (9). This is called critical reflection, and the surface will be referred to as the surface of critical reflection (N_c is called the critical density). If this critically reflecting surface has dimensions large compared with the wavelength, the propagation of a wave can be described with reasonable accuracy by geometrical optics, or ray theory.

For simplicity only the case of backscatter is considered. As a first approximation the scatterer can be replaced by a metallic surface coincident with the critically reflecting surface: the rays are then all straight lines specularly reflected from this surface. The scattering coefficient from a smooth, curved surface of this sort is obtained using similar considerations to those of Aspinall and Hawkins (1950);

$$\sigma = \frac{1}{4}\left(\frac{R_1 r_0}{R_1+r_0}\right)\left(\frac{R_2 r_0}{R_2+r_0}\right), \tag{10}$$

where r_0 is the distance from the point of reflection to the field point (receiver), and R_1 and R_2 are the principal radii of curvature of the surface at the point of reflection. Using the results of differential geometry, it can be shown that the scattering coefficient of a prolate spheroid which is small compared to r_0 is

$$\sigma = \frac{p^2h^2}{4(\cos^2\phi+h^2\sin^2\phi)^2}, \tag{11}$$

where p is the semiminor axis of the spheroid, h is the axial ratio, and ϕ is the angle that the axis of the spheroid makes with the incident wave front. For a gaussoid, $p=a[\ln(N_0/N_e)]^{\frac{1}{2}}$ and the scattering coefficient becomes

$$\sigma = \frac{a^2h^2\ln(N_0/N_e)}{4(\cos^2\phi+h^2\sin^2\phi)^2}. \tag{12}$$

Actually the rays are not straight lines as assumed in this derivation, but are curved due to the effect of the electrons outside the critically reflecting surface. The computation of the actual ray paths in a gaussoid is quite difficult. The effect of refraction can be approximated by using the results of a similar problem relating to a cylindrical, Gaussian distribution treated by Manning (1953) in connection with overdense meteor trails. He showed that the electrons outside the critical surface made the distribution behave as a specularly reflecting surface having an effective radius, ρ_e, that can be expressed in terms of r_c, the radius of the true critically reflecting surface:

$$\rho_e = r_c f(N_c/N_0). \tag{13}$$

The function $f(N_e/N_0)$ is shown in Fig. 1 (after Manning). The scattering coefficient for a gaussoid can be approximately corrected for this effect by

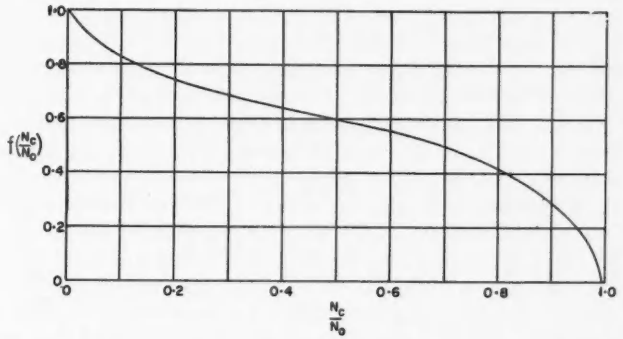

FIG. 1. Ratio of the effective radius to the critical radius for a cylindrical, Gaussian distribution (after Manning 1953).

multiplying each of the principal radii of curvature by $f(N_e/N_0)$. Thus

$$\sigma = \frac{a^2h^2f^2(N_e/N_0)\ln(N_0/N_e)}{4(\cos^2\phi+h^2\sin^2\phi)^2}. \tag{14}$$

The electrons outside the critically reflecting surface also have an effect on the angular dependence of the scattered field. Equation (14) is expressed in terms of the radii of curvature of the critically reflecting surface at the point where the normal to the surface makes an angle ϕ with the plane normal to the axis of the gaussoid. The ray which is normal to the critically reflecting surface at this point is, in general, curved, and the angle, ϕ', that it makes with the plane normal to the axis of the distribution at a large distance from the gaussoid is less than ϕ. The scattering coefficient can be expressed in terms of the angle ϕ' (which will provide the required correction to the angular dependence) by replacing ϕ in (14) by $\phi'+\delta(\phi', h, N_e/N_0)$, where $\delta=\phi-\phi'$. The definition of ϕ' now corresponds with the original definition of ϕ, so the prime can be dropped to give

$$\sigma = \frac{a^2h^2f^2(N_e/N_0)\ln(N_e/N_0)}{4[\cos^2(\phi+\delta)+h^2\sin^2(\phi+\delta)]^2}. \tag{15}$$

Without detailed ray tracing, all that can be said about δ is that it is zero when ϕ is 0° or 90°.

Small, Strong Scatterers

If the gaussoids are small compared with the incident wavelengths, and the electron density is large, interactions between the electrons can modify the scattered field, giving rise, on occasion, to strong electrostatic fields and to resonances for certain polarizations. Even though the peak electron density, N_0, is greater than the critical density, the wave may still penetrate the

scatterer if it is too thin to attenuate significantly the evanescent wave which exists within the surface of critical reflection.

If the wave penetrates the scatterer, it acts on the electrons with a force which is nearly equal across the scatterer. The resulting electrostatic fields can increase the amplitude of the reflected wave to a value greater than that obtained from scatter theory. For a Gaussian, cylindrical distribution (Kaiser and Closs 1952; Herlofson 1951) the scattered field may be as much as twice the value predicted by scatter theory for polarization transverse to the cylinder axis, but no increase occurs for parallel polarization. A similar study for a spherical distribution (Kaiser and Closs 1952) gives essentially the same value of the field as obtained from scatter theory. Although no calculations are available in the literature for a gaussoid, it is likely that the amplitude of the scattered field will be less than twice the value given by scatter theory and probably close to it. Since this study is concerned only with the general characteristics of the amplitude of the scattered field and not with polarization effects, it appears sufficient to use scatter theory to describe reflection from small, strong scatterers which are penetrated by the wave.

If the electron density is sufficiently high to prevent the wave from penetrating the scatterer, the electrostatic forces produced by the motion of the electrons are now large enough to keep the amplitude of this motion very small; in other words, the scatterer becomes highly conducting. An approximate indication of the behavior of a gaussoid in this situation can be obtained by considering the behavior of a conducting spheroid. The particular size of spheroid that should best represent the gaussoid is not evident. A spheroid having the dimensions of the surface $k = -1$ will be used. This is similar to, although more simple than, the criterion chosen by Kaiser and Closs (1952), in their discussion of meteor reflections. Assuming that this surface has dimensions that are small compared to the wavelength, and that the transmitted and received polarizations are identical, the following expression is obtained for the scattering coefficient:

$$\sigma = k^4 a^6 h^2 \ln^3(N_0/2N_c)[g_\perp \sin^2\theta + (g_\perp \sin^2\phi + g_\parallel \cos^2\phi)\cos^2\theta]^2. \tag{16}$$

Here ϕ is the angle that the axis of the distribution makes with the plane of the wave front, and θ is the angle that the incident field vector makes with the plane which contains the normal to the wave front and the axis of the distribution. The functions $g_\parallel$ and $g_\perp$ are given approximately in Fig. 2. These are the principal dipole moments of spheroids (parallel and transverse, respectively, to the axis of the spheroid) of different axial ratios, normalized to the dipole moment of a conducting sphere.

The Regions of Validity of the Different Mechanisms

The reflection of radio waves from gaussoids for various limiting conditions has been discussed. It is now necessary to examine the ranges of size and frequency for which these different reflection mechanisms apply. There are three conditions separating the mechanisms. The first is the one separating critical from non-critical reflection,

$$N_0 = N_c. \tag{17}$$

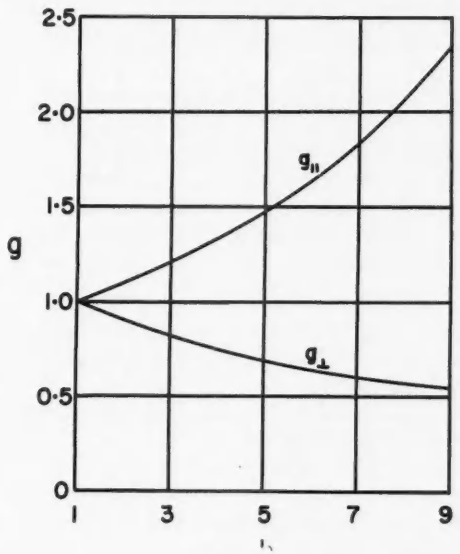

FIG. 2. Approximate, normalized, principal dipole moments of a spheroid as a function of its axial ratio, h.

The second distinguishes between large and small scatterers with greater than critical electron densities. This can be written

$$kr_c = 1, \tag{18}$$

where r_c is the radius of the critically reflecting surface. The third condition distinguishes between small, strong scatterers which are and are not fully penetrated by the wave. This is given approximately by equating the depth of penetration of the evanescent wave to the size of the scatterer. Following Kaiser and Closs (1952) the depth of penetration is assumed to be equal to the skin depth for a plane dielectric. This is given by

$$d = 1/k\sqrt{-\kappa}. \tag{19}$$

The skin depth is the depth at which the wave amplitude falls to $1/e$ of its original value. Assuming that the gaussoid behaves as a uniform slab of thickness 'a', and electron density N_0,

$$-\kappa = -1+\frac{4\pi r_e}{k^2}N_0 \approx \frac{4\pi r_e N_0}{k^2} = \left(\frac{k_c}{k}\right)^2,$$

and the condition becomes

$$k_c a = 1, \tag{20}$$

where $k_c=(4\pi r_e N_0)^{\frac{1}{2}}$ is the critical wave number for a scatterer. By defining normalized wave numbers and sizes we can represent all the cases on a single diagram:

$$k'=k/k_c, \qquad a'=k_c a. \tag{21}$$

Using these new variables, (17), (18), and (20) become

$$\begin{aligned} k' &= 1, \\ (k'a')^2 \ln(1/k'^2) &= 1, \\ a' &= 1. \end{aligned} \tag{22}$$

The resulting diagram (Fig. 3) shows the regions of validity for all gaussoids having a given peak electron density (which fixes k_c, and thus the scale of the diagram). This diagram indicates three different types of frequency dependence, depending on the size of the scatterer relative to the wavelength of the critical frequency for the scatterer. When $ak_c<1$, scatter theory is valid throughout the entire frequency range (keeping in mind the possibility of a slight resonance effect at the frequencies below the critical frequency); when $1 < a' < 1.65$, the small conductor theory becomes important at the lower frequencies; when $a' > 1.65$, there is a transition from scatter theory

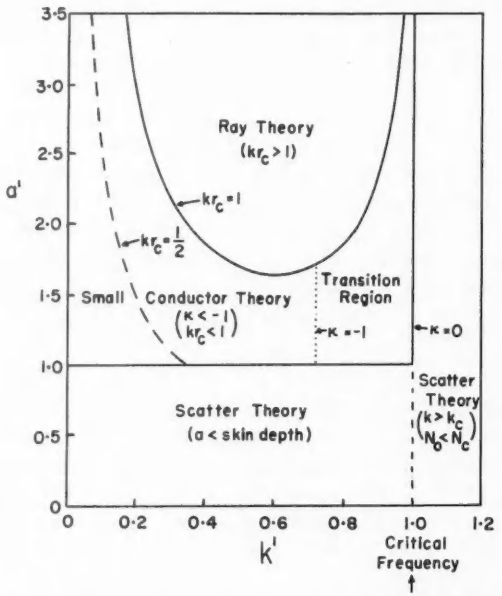

FIG. 3. Regions of validity of the different reflection mechanisms ($a'=ak_c$ is the normalized scatterer "size", and $k'=k/k_c$ is the normalized wave number of the radio wave).

to ray theory near the critical frequency, and again from ray theory to small conductor theory at a lower frequency (just how low depends upon the magnitude of a').

Not all of these dividing lines can be given equal importance. The $k'=1$ line almost certainly separates scatter theory from ray optics, particularly for large values of a'. The boundary $a'=1$, corresponding to the condition that a be equal to the skin depth, is very approximate and indicates only that a transition of this sort takes place in that region of the diagram. Similarly, the line separating ray theory from small conductor theory could probably be represented just as well by the curve $kr_e=\frac{1}{2}$, which, as can be seen in the diagram, is widely separated from $kr_e=1$, indicating a broad transition between these two limiting conditions.

The Frequency Dependence of a Gaussoid

An examination of the expressions (7), (15), and (16) for the scattering coefficients for the different mechanisms reveals that they can be expressed in terms of the normalized wave numbers and sizes as given by (21). With the introduction of a normalized scattering coefficient, $\sigma'=k_e^2\sigma/h^2$, (7), (15), and (16) become, respectively,

$$\sigma_s' = \frac{\pi a'^6}{16} e^{-2k'^2a'^2(\cos^2\phi+h^2\sin^2\phi)}, \tag{23}$$

$$\sigma_R' = \frac{a'^2 f^2(k'^2)\ln(1/k'^2)}{4[\cos^2(\phi+\delta)+h^2\sin^2(\phi+\delta)]^2}, \tag{24}$$

$$\sigma_c' = k'^4 a'^6 \ln^3(1/2k'^2)[g_\perp \sin^2\theta+(g_\perp \sin^2\phi+g_\parallel \cos^2\phi)\cos^2\theta]^2. \tag{25}$$

These expressions were used to plot the curves in Fig. 4, which show the frequency dependence of the normalized scattering coefficient for $\phi=0$, and for an axial ratio of 5. The curves would be the same for all but the small conductor theory for any other value of h. For the small conductor theory the average of the scattering coefficients for the two orthogonal polarizations, $\theta=0°$ and 90°, has been plotted. From Fig. 3, one would expect that below $a'=1$, the scatter theory would be valid throughout the entire frequency range. Examples of this type of frequency dependence are shown for $a'=0.5$ and $a'=1$. When $1 < a' < 1.65$, there should be, on the basis of Fig. 3, a transition from scatter theory to small conductor theory. The curve for $a'=1.5$ illustrates this type of behavior. The curves for $a'=2$, 3, show all three mechanisms becoming important in different frequency ranges. The scattering coefficient for the scatter theory decreases very rapidly for values of a' larger than 2.

Also of interest is the angular dependence of the scattering coefficient. As a measure of the angular dependence or aspect sensitivity (as this characteristic of radio-auroral reflections has come to be called) a normalized scattering coefficient, $\tau=\sigma(\phi)/\sigma(0)$, can be defined. The different mechanisms yield the following expressions for this aspect sensitivity factor:

$$\tau_s = e^{-2a'^2k'^2(h^2-1)\sin^2\phi}, \quad \text{(scatter theory)}, \tag{26}$$

$$\tau_R = (\cos^2[\phi+\delta(\phi, h, k'^2)]+h^2\sin^2[\phi+\delta(\phi, h, k'^2)])^{-2}, \quad \text{(ray theory)}, \tag{27}$$

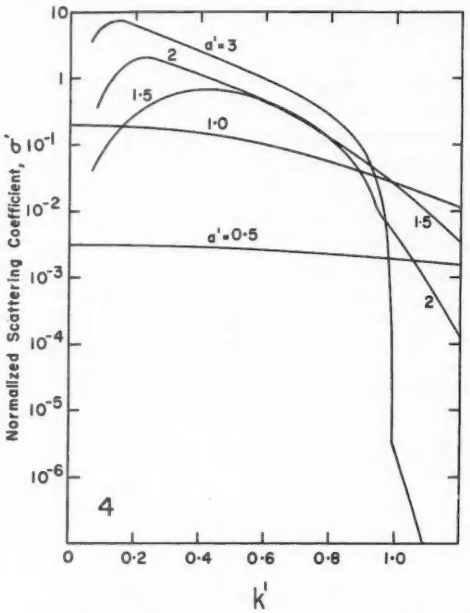

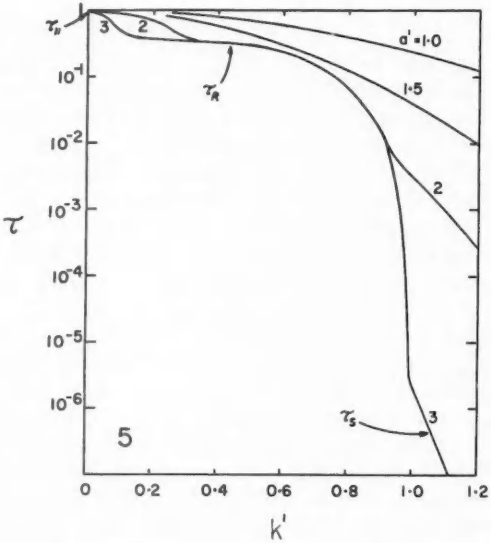

FIG. 4. Normalized scattering coefficient, $\sigma' = k_c^2\sigma/h^2$, as a function of frequency, for a gaussoid ($h=5$, $\phi=0$).

FIG. 5. Aspect sensitivity factor as a function of frequency, for a gaussoid ($h=5$, $\phi=10°$).

$$\begin{aligned} &\tau_\perp = 1, \\ &\tau_\parallel = [1-(1-g_\perp/g_\parallel)\sin^2\phi]^2, \end{aligned} \qquad \text{(small conductor theory).} \tag{28}$$

All of the variation of τ_R with frequency is due to the effect of $\delta(\phi, h, k'^2)$, the behavior of which is not completely known. It is likely that $\tau_\parallel$ should have some similar modification, but just how this is to be done is not clear. Figure 5 gives an indication of the probable type of frequency dependence of τ for $h=5$ and $\phi=10°$.

ASSEMBLIES OF GAUSSOIDS

The next step in developing a model of auroral ionization is to consider the nature of the field scattered from an assembly of gaussoids. If, as seems likely, the scatterers are distributed randomly in space, the power scattered from each individual scatterer will add. This is equivalent to adding the scattering coefficients. The use of such a procedure assumes that the scatterers are all at distances from the field point that are large compared to the dimensions of the region enclosing them, that they are sufficiently numerous, and that the scatterers are neither sufficiently strong nor sufficiently closely packed so that multiple scattering becomes important. It will be assumed in this section that such a situation prevails.

The simplest assembly of gaussoids is obviously one in which all of the scatterers are identical. For such an assembly a scattering coefficient per unit volume, σ_v, can be defined, which is related to that for the individual scatterers by n, the number of scatterers per unit volume:

$$\sigma_v = n\sigma. \tag{29}$$

Evidently the characteristics of the assembly are essentially the same as those of the individual scatterers. It is undoubtedly naive to use such an assembly as a model of auroral ionization, yet it is interesting to note that it includes as special cases most of the previously suggested models.

It is of particular interest to compare such an assembly of very weak scatterers with the model developed by Booker (1956). From an autocorrelation function for the electron density of the form

$$\rho(\xi, \eta, \zeta) = e^{-\frac{1}{2}[(\xi^2+\eta)^2/a^2+(\zeta^2/c^2)]}, \tag{30}$$

Booker derived a scattering coefficient per unit volume which can be written

$$\sigma_v = r_e^2\overline{(\Delta N)^2}a^3h(2\pi)^{3/2}e^{-2k^2a^2(\cos^2\phi+h^2\sin^2\phi)}, \tag{31}$$

where $\overline{(\Delta N)^2}$ is the mean square deviation of the electron density. Equations (7) and (29) give for an assembly of weak gaussoids,

$$\sigma_v = nr_e^2q^2e^{-2k^2a^2(\cos^2\phi+h^2\sin^2\phi)}. \tag{32}$$

The mean square deviation for the assembly can be easily determined if it is assumed that the scatterers are sufficiently far apart so that in the volume

$1/n$ around one scatterer the electrons due to the other scatterers are negligible. Then for the distribution of (1), the mean square deviation is

$$\overline{(\Delta N)^2} = nq^2/a^3h(2\pi)^{3/2}. \tag{33}$$

Substitution of (33) in (32) gives (31), which shows that the two approaches are essentially similar. The need to require that the scatterers be widely separated is clear, since it is only then that the autocorrelation of the medium will be that given in (30). In spite of the fact that the two approaches give the same expression for the scattering coefficient, there are interesting and useful differences in the two results. Since the Booker expression is derived on the basis of an autocorrelation function, it describes the scattered field from any distribution of ionization having an autocorrelation function of the form given by (30), of which media there are an infinite number. However, the problem of specifying these media is difficult. On the other hand, the expression derived from an assembly of similar gaussoids, (32), is known to describe the field scattered from a certain family of scattering media; namely, assemblies of similar, weak gaussoids. From (33), any assembly of similar, weak gaussoids which leaves the product nq^2 constant has the same scattering coefficient per unit volume.

A model such as that proposed by Kaiser (1956), which consists of an assembly of large, similar, critically reflecting, spheroidal scatterers, is adequately described by an assembly of similar, critically reflecting gaussoids: in addition the gaussoidal assembly includes the effect of diffuse boundaries, and is therefore perhaps more reasonable from the physical point of view.

This type of assembly also provides a quantitative basis for considering a model such as that suggested by Forsyth and Vogan (1957), which involves scatterers critically reflecting at one frequency, and weakly scattering at a higher frequency.

Although an assembly of similar scatterers is useful, it is likely that other classes of scattering assemblies will resemble the physical situation more closely. It therefore seems profitable to consider the physical processes that are likely to control the distribution of ionization in the aurora and the sort of assemblies that they suggest.

The irregularities in auroral ionization may be formed in several different ways, but it seems certain that the sharpness of the boundaries of such irregularities will be limited by diffusion. The earth's magnetic field will cause electrons moving across the field lines to gyrate around them; the diffusion will therefore be slower across the field lines than along them, although this anisotropy will disappear at heights where the collision frequency becomes comparable with the gyro-frequency. A rigorous examination of this problem requires consideration of the ambipolar effects in the diffusion. Apparently such an examination has not been carried out, but Kaiser (1953) has given a simplified treatment which suggests that the magnetic field probably introduces anisotropy into the diffusion at heights near 100 km and above, the anisotropy increasing with height. The distribution of ionization arising due to diffusion from a point in the presence of a magnetic field is a gaussoid.

Although many pictures of auroral ionization would directly imply diffusion from a point, and hence gaussoidal scatterers, it seems likely that even irregularities produced by other processes will, under the action of diffusion, acquire characteristics quite accurately represented by gaussoids.

It is possible to think of several basically different physical processes controlling the formation of auroral ionization, each of which leads to a different type of scattering assembly. The ionization might be produced in small clumps or columns by high-velocity, incoming particles continually entering the atmosphere. The resulting scatterers might well all have the same total number of electrons, and their subsequent diffusion would lead to a regime of scatterer sizes which was unchanging with time. On the other hand, it might be more appropriate to think of these scatterers as maintained against debilitation by recombination and diffusion by a continual regeneration of ionization, so that the resulting scatterers would have about the same peak electron density, and have a range of sizes introduced by the varying equilibrium conditions between the production and decay of ionization. Again, the auroral ionization might be produced by the incoming particles as a large, rather uniform blanket, the irregularities in the ionization being subsequently introduced by the action of turbulence or wave motion of the atmosphere. This would likely produce scatterers with about the same peak electron density, and with a distribution of scatterer sizes which is characteristic of turbulence. Almost certainly the actual situation is a combination of these various production mechanisms, the resulting assembly having a distribution of both size and peak electron density of the scatterers.

Consider first an assembly of scatterers produced by the continuous formation of very small clumps of ionization which subsequently diffuse, the number of electrons in each clump being the same, and their occurrence being random both in space and time. It is assumed that the process has been going at a constant rate for a time sufficiently long to make the distribution of scatterers with size constant with time. Then the number of scatterers per unit volume per unit range of scatterer sizes is

$$n(a) = Ma/2D, \tag{34}$$

where M is the number of scatterers formed per m^3 per second, and D is the diffusion coefficient in m^2/sec. If a scatterer of size a has scattering coefficient $\sigma(a)$, the scattering coefficient per unit volume for the assembly is

$$\sigma_s = \int_{a_0}^{\infty} n(a)\sigma(a)da = \frac{M}{2D}\int_{a_0}^{\infty} a\sigma(a)da, \tag{35}$$

where a_0 is a limit put on the initial size of the scatterers by the physical processes involved. No irregularity in the auroral ionization can be smaller than the electron mean free path, or the electron gyro-radius (which ever is the smaller) for directions transverse to the field lines. It appears likely that this will limit a_0 to values greater than about 0.3 meter in directions transverse to the magnetic field, and to values greater than about 0.3 to 1.0 meter for directions parallel to the magnetic field at ionospheric heights of about 100 km.

To evaluate (35) consider the case where $\phi=0$, and ignore the small conductor theory, since it is valid only for very small, strong scatterers, which are not important physically. If a_0 is sufficiently large, the scatterer will never be thicker than the skin depth at any frequency, and $\sigma(a)$ will be given entirely by (7). From (5) and (20), this will occur if

$$a_0 > \frac{4r_e q}{h\sqrt{\pi}} = \gamma. \tag{36}$$

For smaller values of a_0, $\sigma(a)$ will still be given by (7), if the frequency is sufficiently high so that the peak electron density is less than the critical density. From (5), (9), and (17), this occurs if

$$a_0 < \gamma, \qquad k > (\gamma/a_0^3)^{1/2}. \tag{37}$$

At lower frequencies both mechanisms are valid at different sizes, the size at which the transition occurs being given by

$$a = (\gamma/k^2)^{1/3}. \tag{38}$$

Using these results, and numerically integrating the ray theory expressions it is possible to evaluate (35) for different values of a_0 as a function of frequency. Figure 6 shows the resulting normalized scattering coefficient per

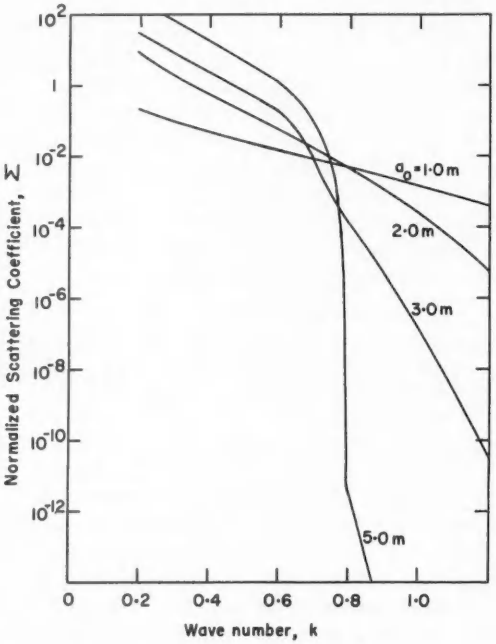

FIG. 6. Normalized scattering coefficient, $\Sigma = D\sigma_v/h^2M$, as a function of frequency, for an assembly of diffusing scatterers ($\phi=0$, $\gamma=0.64a_0^3$).

unit volume for various values of a_0 and γ (proportional to the total number of electrons in each scatterer). The values used were chosen so that for each curve the ray theory made a contribution only for wave numbers less than $0.8\ \mathrm{m}^{-1}$. This leads to a transition at this wave number from a region where ray theory is important to one where scatter theory is important. The curve for $a_0 = 1$ m illustrates a case where the scatter theory is valid throughout the frequency range. As the minimum size increases the sharpness of the transition also increases, but a comparison with Fig. 4 indicates that the transition is much less abrupt than for an assembly consisting of similar scatterers, all of the minimum size.

The other class of assemblies considered in this paper is one consisting of scatterers of different sizes, all having the same peak electron density. This is equivalent to integrating (with a weighting factor) along a vertical line on Fig. 3. If $k' < 1$, there is a transition from scatter theory to ray theory at a value of a' of approximately 2. If $k' > 1$, scatter theory is valid throughout. The scattering coefficient can be written

$$\sigma_v = \int_{a_0}^{\infty} n(a)\sigma_s(a)da, \qquad k' > 1, \tag{39}$$

$$= \int_{a_0}^{2} n(a)\sigma_s(a)da + \int_{2}^{\infty} n(a)\sigma_R(a)da, \qquad k' < 1.$$

Consider a size distribution of the form

$$n(a) = n_0 a^p e^{-pa^2/2a_m^2}. \tag{40}$$

This distribution has a maximum value at a_m, falling to zero both at $a = 0$ and $a = \infty$. Several examples of this family of distributions are shown in Fig. 7. As p approaches infinity the distribution becomes a very narrow peak about $a = a_m$, and thus approaches the case of an assembly of similar scatterers. For

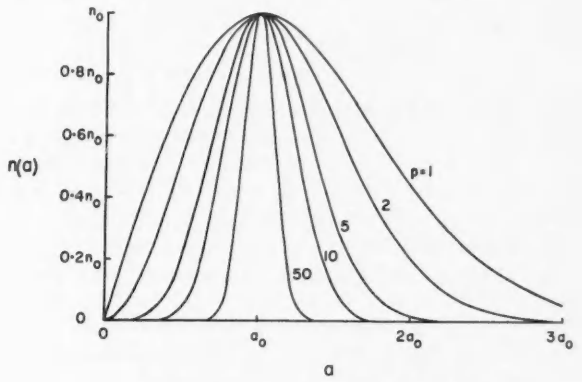

FIG. 7. The distribution $n(a) = n_0\, a^p e^{-pa^2/2a_m^2}$.

comparison, it is of interest to rewrite these size distributions so that they all have the same total number of electrons per unit volume, Q: from (5) and (40),

$$n(a) = \frac{p^{(p+4)/2}}{\pi^{3/2}2^{(p+2)/2}\Gamma\left(\frac{p+4}{2}\right)} \cdot \frac{Q}{N_0 h a_m^{p+4}} \cdot a^p e^{-pa^2/2a_m^2}, \tag{41}$$

where $\Gamma(x)$ is the gamma function. Here the minimum size, a_c, has been assumed to be zero. The scattering coefficients from these assemblies can be obtained by substituting (23), (24), and (41) in (39). In general the cases for $k' < 1$ can only be solved by numerical integration. However, in practice, if n is sufficiently large, and $a_m k_c$ is greater than 2, the scatter theory term can be neglected. Under these circumstances, little error will be introduced by assuming the minimum size to be zero. The resulting expressions can be integrated to yield the following scattering coefficients:

$$\sigma_v = \frac{Qhk_c a_m'^3 A_p}{N_0\left[1+\frac{4a_m'^2k'^2}{p}(\cos^2\phi+h^2\sin^2\phi)\right]^{(p+7)/2}}, \qquad k' > 1, \tag{42}$$

$$= \frac{Qhk_c B_p f^2(k'^2)\ln(1/k'^2)}{N_0 a_m'[\cos^2(\phi+\delta)+h^2\sin^2(\phi+\delta)]^2}, \qquad k' < 1, \tag{43}$$

where

$$A_p = \frac{\Gamma\left(\frac{p+7}{2}\right)}{2^{5/2}\pi^{1/2}p^{3/2}\Gamma\left(\frac{p+4}{2}\right)}, \tag{44}$$

$$B_p = \frac{p^{1/2}\Gamma\left(\frac{p+3}{2}\right)}{2^{5/2}\pi^{3/2}\Gamma\left(\frac{p+4}{2}\right)}, \tag{45}$$

and where $a' = k_c a$ and $k' = k/k_c$, as before. As p approaches infinity the assembly described by (41) approaches an assembly of similar scatterers, all of size a_m. Using the expansion of the gamma function for integral values of p, Wallis' product for π, and the limit expression for e^x, it can be shown that A_p approaches $1/16\pi^{1/2}$ and B_p approaches $1/4\pi^{3/2}$ and the scattering coefficients given by (42) and (43) become the expressions for an assembly of similar scatterers of size a_m having a total of Q electrons per unit volume, just as one would expect. Figures 8 and 9 show the normalized scattering coefficient per unit volume as a function of wave number for different values of p, for two values of a_m, and for $\phi = 0$. The distribution of sizes has little effect on the nature of the critically reflected coefficients, but changes markedly the frequency dependence of the weakly scattered waves. The lower values of p

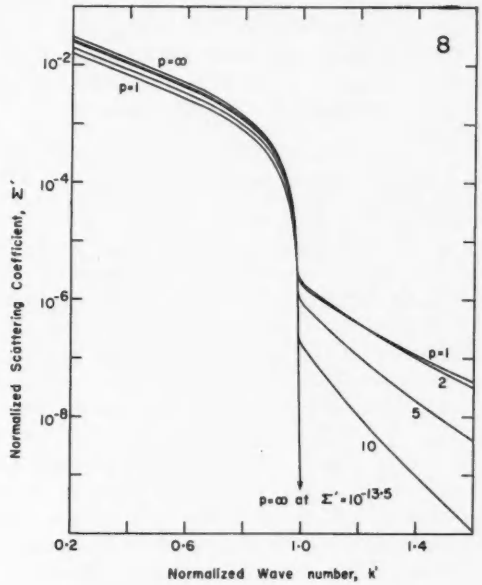

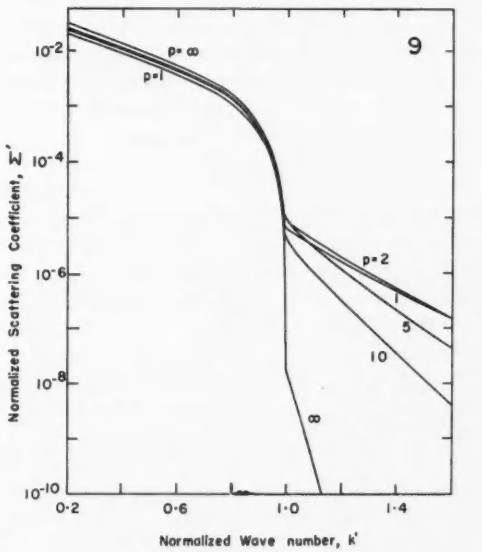

FIG. 8. Normalized scattering coefficient, $\Sigma' = N_0\sigma_T/Qhk_c$, as a function of frequency, for an assembly of gaussoids with a distribution of sizes given by (41) ($a_m' = 4$, $\phi = 0$).

FIG. 9. Normalized scattering coefficient, $\Sigma' = N_0\sigma_T/Qhk_c$, as a function of frequency, for an assembly of gaussoids with a distribution of sizes given by (41) ($a_m' = 3$, $\phi = 0$).

decrease the frequency dependence over that for the assembly of similar scatterers. For $k'=1$ this effect is reversed if a'_m is less than 1.3. Decreasing the size of p then makes the scattering coefficient fall more rapidly with frequency. Such a low value of a'_m does not allow the complete integrals from which (43) was derived to be used, and therefore cases such as this are not shown in these diagrams.

CONCLUSIONS

Scattering coefficients have been determined for several families of models of auroral ionization. These models appear to encompass many of the possible types of auroral models. The assembly of similar gaussoids is basic to any consideration of auroral ionization, covering the whole range of sizes, shapes, and frequencies. The effects of distributing the sizes and strengths of these scatterers are illustrated by the other assemblies considered. It should be noted that none of these assemblies involve a distribution of sizes with maxima at more than one size. (A simple example of a distribution with maxima at two sizes would be one consisting of scatterers of two different sizes.) The characteristics of such distributions can be quite different from those considered in this paper.

In this paper equations and curves have been presented, representing the properties of the scattering coefficients of these different auroral models. An experimental investigation does not usually provide a direct measurement of the scattering coefficient of auroral ionization, so the results of this paper must be interpreted in terms of the conditions of each particular experiment. In Part II (Moorcroft 1961) the available experimental data are examined, particularly with regard to their suitability for interpretation in terms of models of auroral ionization, and some of the results are used to draw conclusions concerning the nature of auroral ionization.

REFERENCES

ASPINALL, A. and HAWKINS, G. S. 1950. J. Brit. Astron. Assoc. **60**, 130.
BOOKER, H. G. 1956. J. Atmospheric and Terrest. Phys. **8**, 204.
BOOKER, H. G., GARTLEIN, C. W., and NICHOLS, B. 1955. J. Geophys. Research, **60**, 1.
BULLOUGH, K. and KAISER, T. R. 1954. J. Atmospheric and Terrest. Phys. **5**, 189.
COLLINS, C. and FORSYTH, P. A. 1959. J. Atmospheric and Terrest. Phys. **13**, 315.
ESHLEMAN, V. R. 1952. Tech. Rept. No. 49, Electronics Research Laboratory, Stanford University, California.
FLOOD, W. A. 1960. J. Geophys. Research, **65**, 2261.
FORSYTH, P. A. 1953. J. Geophys. Research, **58**, 53.
FORSYTH, P. A. and VOGAN, E. L. 1957. J. Atmospheric and Terrest. Phys. **10**, 215.
HERLOFSON, N. 1947. Nature, **160**, 867.
——— 1951. Arkiv. Fysik, **3**, 247.
KAISER, T. R. 1953. Advances in Phys. **2**, 495.
——— 1956. The airglow and the aurorae (Pergamon Press), p. 156.
KAISER, T. R. and CLOSS, R. L. 1952. Phil. Mag. **43**, 1.
LOVELL, A. C. B., CLEGG, J. A., and ELLYETT, C. D. 1947. Nature, **160**, 372.
MANNING, L. A. 1953. J. Atmospheric and Terrest. Phys. **4**, 219.
MOORCROFT, D. R. 1961. Can. J. Phys. **39**. This issue.
PRESNELL, R. I., LEADABRAND, R. L., PETERSON, A. M., DYCE, R. B., SCHLOBOHM, J. C., and BERG, M. R. 1959. J. Geophys. Research, **64**, 1179.

MODELS OF AURORAL IONIZATION

PART II. APPLICATIONS TO RADIO OBSERVATIONS OF AURORA[1]

D. R. MOORCROFT

ABSTRACT

In this paper the available experimental evidence concerning radio reflections from aurora is examined in relation to the reflection characteristics of the models of auroral ionization discussed in Part I.

The existence of critical reflection from auroral ionization at frequencies between 30 and 50 Mc/s appears to be established. This implies electron densities as great as 3×10^{13} electrons/m^3. It is shown that the observations are consistent with a model consisting of irregularities of ionization elongated parallel to the earth's magnetic field in a ratio of between 5 and 10 times, and having sizes transverse to the field lines of the order of a few meters. Some of the observations require the irregularities to be distributed in size. It is clear that there is a need for more relevant measurements on radio reflections from aurora to specify the characteristics of the ionization more precisely.

INTRODUCTION

In Part I (Moorcroft 1961) several general models of auroral ionization were presented, and their reflecting characteristics for radio waves were discussed. These models all include consideration of both critical reflection and weak scattering of radio waves, and, taken together, provide a general treatment, covering a range of differing pictures of auroral ionization as seen by means of radar techniques. A re-examination of the relevant experimental evidence in the light of this general treatment should provide information regarding the nature of the auroral ionization, and should indicate other types of experiments that would distinguish the various reflection mechanisms. It will be shown that such an examination settles the question of the existence of critical reflections in auroral reflections.

A description of auroral ionization can be given conveniently in terms of the size and distribution of sizes of the individual irregularities, their shape, their strength (i.e. peak electron density), the sharpness of their boundaries, and the number of scatterers per unit volume. In the literature there is considerable disagreement upon many of these aspects of the model. The estimates of size range from a fraction of a meter (Booker 1956) to hundreds of meters (Kaiser 1956). Some types of auroral ionization have been suggested to consist of isotropic scatterers (Collins and Forsyth 1959), while estimates of the elongation of anisotropic scatterers range from an axial ratio of 4:1 (Forsyth and Vogan 1957) to about 40:1 (Booker 1956). The most fundamental and important difference relates to the strengths of the scatterers. From the beginning of these studies, when Herlofson (1947) suggested that it would be physically unreasonable to interpret the auroral reflections obtained by Lovell, Clegg, and Ellyett (1947) as due to critical reflections, with the higher electron

[1]Manuscript received December 14, 1960.
Contribution from the Institute of Upper Atmospheric Physics, University of Saskatchewan, Saskatoon, Saskatchewan.

densities that that interpretation implied, the role of critical reflection in producing auroral echoes has been widely discussed. More recently, Booker (1956) has suggested that weak scattering is the reflection mechanism at frequencies as low as 30 Mc/s, while Kaiser (1956) has visualzed critical reflection being important up to frequencies as high as 100 Mc/s. Forsyth (1953), Forsyth and Vogan (1957), and Collins and Forsyth (1959), on the basis of multiple-frequency measurements, have concluded that for frequencies between 30 and 100 Mc/s, there are times when the frequency dependence is such that a transition from strong to weak scattering must take place within this frequency range. They also suggest that at other times the whole frequency range may be reflected by either weak scattering or critical reflections.

EXPERIMENTAL EVIDENCE

Not all of the experimental evidence on radio-auroral reflections is directly relevant to a discussion of the properties of auroral ionization. Many studies have been undertaken to reveal the diurnal, annual, and solar variations of radio-aurora, and its correlation with various other geophysical phenomena: these are not concerned with the process of reflection. Other observations which do relate to the reflection mechanism (and thus to the nature of the ionization responsible for the reflection) are complicated by the superposition of effects due to the properties of the radio system being used, and other effects resulting from the spatial distribution of auroral ionization.

In particular, there are several limitations imposed on the interpretation obtained from a radar system which, while perhaps obvious, are nevertheless worthy of mention. Since the pulse length of a pulsed radar is finite, all echo information is integrated over distances equal to the spatial length of the pulse. Similarly, the finite repetition rate means that changes in the scattering region which take place in times shorter than the repetition period cannot be detected. The antenna pattern of the radar is affected to some extent by the terrain over which it is directed. For this reason it is sometimes difficult to specify theoretically the precise antenna pattern. Even experimental determinations of the antenna pattern are not usually sufficiently accurate to allow accurate information to be obtained about the height of the reflecting region (this is particularly true at low frequencies).

The relevant experimental evidence available is now examined in the light of the considerations mentioned above, under the following five headings: (i) classification of auroral echoes; (ii) height of reflecting regions; (iii) echo amplitude; (iv) aspect sensitivity; (v) frequency dependence.

Almost all workers, in discussing the nature of echoes received, have classified the reflections into two general categories, usually termed "diffuse" and "discrete". The diffuse echoes are long lasting and widely spread in range (several hundred kilometers). Discrete echoes exhibit structure which is characteristically tens of kilometers in size, sometimes limited by the finite pulse length, which is typically in the range 12 km (for a pulse length of 40 μsec) to 600 km (for 2 msec). Some workers (Booker, Gartlein, and Nichols 1955) do not find any sharp demarcation between short and long spreads in

range. Aspinall and Hawkins (1950), Hellgren and Meos (1952), Currie, Forsyth, and Vawter (1953), and Meos and Olving (1958) suggest two quite distinct types of echoes. Bullough and Kaiser (1954, 1955) obtained both types of echoes but suggest (Bullough and Kaiser 1954) that at least on one occasion the diffuse echo was the coalescence of a large number of discrete echoes. Presnell *et al.* (1959), operating a narrow beam antenna on 218, 398, and 780 Mc/s, find two quite different types of auroral echoes, and associate them with quite different distributions in space. The "diffuse" scattering centers seem to be distributed in an almost horizontal layer of wide extent, while the "discrete" scattering centers seem to lie along lines of the magnetic field. They found that the diffuse type of echoes occurred during the daytime. There may be no relation between the "diffuse" and "discrete" classifications of Presnell and those of the earlier workers. It is tempting to associate the diffuse radio-aurora of Presnell *et al.* with the type A_3 radio-aurora observed by Collins and Forsyth (1959) on their bistatic system. Of the three types of auroral echoes observed they found only A_3 occurring in the daytime. However, it appeared to be located in a layer rather low in the ionosphere (that is, probably below 100 km), and was apparently not aspect sensitive, which contrasts with the observations of Presnell *et al.*, who found the diffuse radio-aurora to be quite aspect sensitive, and located at about 100-km height. It is not clear how all these different observations are related, but there seems to be evidence of at least two distinct types of auroral ionization, which may have quite different characteristics.

The ionospheric parameters used in conjunction with a model of auroral ionization depend very markedly upon the height at which the reflecting ionization is located. These heights are very difficult to determine accurately with a v.h.f. radar alone, since usually the width of the antenna pattern and the uncertainties in it are so large as to make height estimates ambiguous. Studies by various workers suggest that most radio-auroral reflections come from ionization located between 100 and 120 km. The most accurate determination of height available is that of Unwin and Gadsden (1957), who used an antenna with a large number of well-defined lobes (produced by interference between the direct signal and the signal reflected from the sea, over which the antenna looked from a high cliff). They obtained very consistent results, indicating reflection from a layer many hundreds of kilometers in extent and often varying in height by only 4 or 5 km along its extent. They concluded that the reflecting layer was less than 2.5 km in thickness, and had a height of about 110 km, with individual heights ranging from 100 to 120 km. However, recent observations of the Stanford group (Schlobohm *et al.* 1959) at 106 Mc/s suggest that at low latitudes radio-auroral echoes can be obtained from much greater heights, perhaps as high as 300 km.

Although, in principle, amplitude measurements of radio-auroral echoes contain much useful information about the mechanism of reflection, the information is very difficult to separate from the many other factors that contribute to the echo amplitude. Finally, one would like to deduce the scattering coefficient per unit volume, whereas a radar gives the total scattering

coefficient. To obtain the latter from the former one needs to know the location and extent of the scattering volume, and its depth. Because of these complexities, it is only possible to indicate by amplitude measurements that radio-aurora is quite transparent to v.h.f. radio waves. If the total scattering coefficients observed by different workers are expressed in square kilometers, the extent to which radio-aurora is transparent will become evident. The total scattering coefficient is easily expressed in terms of the radar parameters (Bowen 1954):

$$\sigma = \frac{(4\pi)^2 r^4}{G^2 \lambda^2} \frac{P_r}{P_t}, \tag{1}$$

where G is the antenna gain (with respect to an isotropic radiator), P_t is the transmitted power, P_r is the received power, r is the range, and λ is the free space wavelength. (Note that σ is defined by equation (4) of Part I. The radar cross section often used in the literature is just 4π times this value.) Using (1) it can be seen that Aspinall and Hawkins (1950) detected a total scattering coefficient of 0.36 km^2 at 72 Mc/s. Forsyth (1953) found values of σ as large as 4.5 km^2 on both 56 and 106 Mc/s. Little, Rayton, and Roof (1956) quote Dyce as saying that at 50 Mc/s the equivalent target area is about 30 km^2 for strong aurora, which corresponds to $\sigma = 2.4$ km^2. It is obvious that the value obtained depends to a considerable extent on both the width of the beam, and the integration introduced by the pulse length. Another way of illustrating the over-all transparency of radio-aurora is to define an effective reflection coefficient, defined as the ratio of the echo strength received to that which would be received from a specularly reflecting metal sheet located at the radio-auroral range. Little, Rayton, and Roof (1956) give a value of 10^{-4} for the effective reflection coefficient of strong aurora at 100 Mc/s. These measurements indicate that, on the average, radio-aurora is transparent; they do not imply necessarily that small regions of it can not be highly reflecting.

One of the more controversial aspects of the radio-auroral literature is the interpretation of the observed angular dependence of auroral echoes. Part of the difficulty is that several different factors contribute to the observed distribution and their relative importance is not easily determined. The term aspect sensitivity is generally used to imply an angular dependence of echoes produced as a result of the nature of the reflection process itself.

Before the observed angular dependence can be interpreted in terms of aspect sensitivity, the other factors contributing to the angular dependence must be removed. It is reasonable to expect that radio-aurora is distributed geographically much like optical aurora. If this is the case, then simply from the geographic situation one would expect that for low latitude stations the echoes would come from the north at low elevation angles. Bullough and Kaiser (1954) and Kaiser (1957) have shown that their echoes lie distributed along parallels of geomagnetic latitude, suggesting that the dominant effect in determining the echo location is the geographic distribution of the ionization (presumably closely associated with the optical aurora), and not an aspect sensitive reflection mechanism. Echoes may also be restricted to the northern

azimuths as a result of the actual volume of ionization presented to the antenna beam as it looks in different directions (Forsyth 1960). Suppose that the ionization is distributed along lines of geomagnetic latitude. Then Fig. 1 shows how the difference in volume scattering operates to restrict echoes to

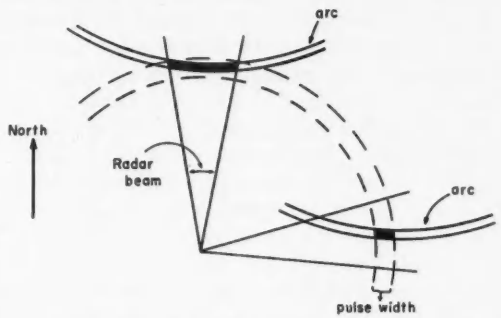

FIG. 1. The effect of the volume distribution of auroral ionization on the angular dependence of radio reflections (after Forsyth 1960).

the north, even for stations which are quite close to the auroral zone. Forsyth has shown that this can account for all of the azimuthal aspect sensitivity observed. Although it is apparent that the ionization is not likely to be distributed strictly in arcs along the geomagnetic latitudes, this effect is nevertheless likely to be of some importance in determining the final angular dependence of the auroral echoes. This same effect (to a reduced extent) is likely important in explaining the variation with elevation angle.

As an alternative to aspect sensitivity for the explanation of the limitation of echoes to low elevation angles, it has been suggested (Currie, Forsyth, and Vawter 1953) that the ionization responsible for radio reflections is underlain with absorbing ionization. It is sufficiently patchy so that from a distance the reflecting ionization is visible between the patches of the absorbing layer. At greater elevations the reflecting ionization is obscured by absorption. There is some question as to how effective this would be. It would require a very particular distribution of ionization below the radio-aurora to extinguish echoes at elevations as low as 15 degrees, and still leave them visible at 12 degrees.

In the light of the above discussion, most of the low latitude observations, which localize radio-auroral occurrence to the north and to low elevation angles, can be explained without any recourse to aspect sensitivity. One exception to this statement is the low latitude, high elevation observations of Schlobohm *et al.* (1959), who detected echoes on 106 Mc/s at heights of 200 to 300 km from a latitude of 43°. They suggest that the only reason these echoes could be seen was that the observations were made normal to the lines of the magnetic field, along which they assume the ionization to lie. Dyce (1955*a*) has operated an auroral radar on 51.7 Mc/s at Point Barrow, which is about 200 km north of the visual auroral zone maximum. He found that more

than 90% of the echoes were obtained from directions to the north of east and west. He presents this as strong evidence for the importance of aspect sensitivity in determining the azimuthal distribution. Recently McNamara (1959) has studied the azimuthal distribution of auroral echoes on 48 Mc/s at Resolute Bay, Baker Lake, Saskatoon, and Ottawa, using four 90° corner reflectors at each station. The results he obtained are shown in Fig. 2. The relative total occurrence at the different stations were in the ratios of 1:8:24:8 for Resolute Bay, Baker Lake, Saskatoon, and Ottawa, respectively. For

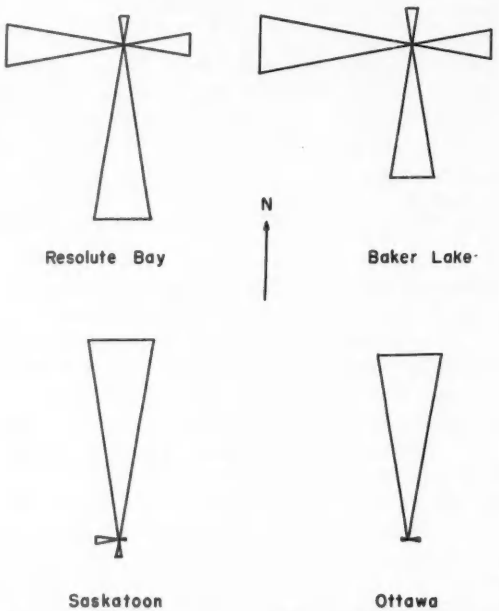

FIG. 2. Azimuthal dependence of auroral echoes (after McNamara 1959).

Resolute Bay and Baker Lake, both of which are far inside the auroral zone the fewest echoes were found to come from the north, although the total number of echoes received was considerably less than at Saskatoon. This suggests that although aspect sensitivity plays some part in determining the azimuthal distribution of echoes, it is not enough to counterbalance the effect of the geographic distribution of ionization at high latitudes. More significant estimates of aspect sensitivity can be made using the variation of echo occurrence with elevation angle, since the effects of geography are not as important as for the azimuthal distribution. Apparently echoes have not been seen at elevation angles above 30°, regardless of the location of the radar. The effect of the volume distribution of scatterers is not likely to be strong enough to cut off echoes at such low elevations, although the strength of the effect will

depend very much on the thickness of the scattering region. Although absorbing regions may be capable of explaining observations of this type at frequencies below, say 100 Mc/s, they will have little effect on high frequencies. It appears likely that the most important factor in limiting auroral echoes to low elevation angles, particularly at high latitudes, is aspect sensitivity. However, if aspect sensitivity is responsible for the elevation angle cutoff, then this maximum angle should be a sharp function of the azimuth, an effect which does not appear to have been observed. Presnell *et al.* (1959) have reported observing echoes at College, Alaska, on 218, 398, and 780 Mc/s at angles up to 12, 10, and 6 degrees, respectively, off perpendicularity with the magnetic field lines. These measurements were not simultaneous, were not made with antennas of similar beam widths, nor were the different frequencies all operated for the same length of time, so it is difficult to draw any reliable conclusions about the frequency dependence of aspect sensitivity from these results. Recently Greenhow, Neufeld, and Watkins (1960) have reported measurements of the angular dependence of auroral echoes made with the Jodrell Bank radio telescope on 36 Mc/s. In analyzing the results they made a correction for the probable geographical distribution of the ionization by using a distribution for optical aurora given by Vestine. They deduced the angular dependence of the scattering from the number of echoes received at different aspect angles, correcting for the relative times spent by the beam in different parts of the sky. The observations and corrected results which they obtained are shown in Fig. 3.

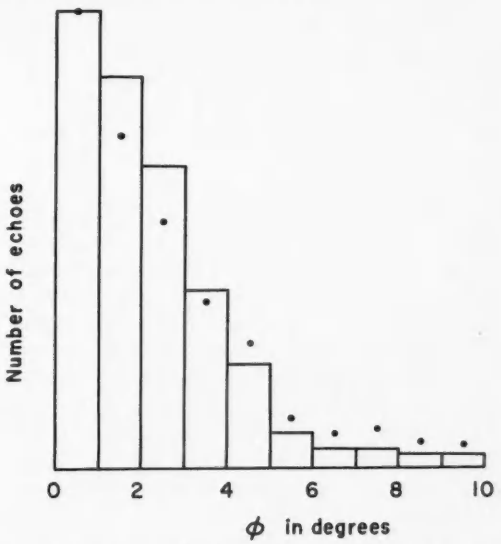

FIG. 3. Aspect sensitivity of auroral echoes observed at Jodrell Bank on 36 Mc/s (after Greenhow *et al.* 1960). The histogram indicates the experimental results; the dots are corrected values.

Further qualitative, if not quantitative evidence for the existence of aspect sensitivity is provided by measurements using bistatic radar systems. Because of the different geometry of the bistatic system it is possible to reduce the effect of the geographical distributions of ionization, and the effect of the volume distribution of the scatterers. That is, a bistatic system can "see" scattering centers over a sufficiently wide area that the conditions related to the location of the ionization (near to the auroral zone, in long arcs aligned along parallels of geomagnetic latitude, perhaps) can be satisfied and still leave a wide range of different conditions of aspect sensitivity to be fulfilled. In the absence of aspect sensitivity, the most favorable condition for forward-scattering is straight along the path, since isotropic scatterers will scatter the greatest amount of energy in the forward direction. If the scatterers are aspect sensitive, echoes could be detected from directions off the path of the system if the aspect conditions were more favorable there. Collins and Forsyth (1959) have reported a detailed investigation of radio-aurora using several bistatic systems. The three types of radio-aurora they distinguished were found to have quite different characteristics, the type A_3 (mentioned before in the discussion of the classifications of auroral echoes) being apparently isotropic, while types A_2 and A_1 showed evidence of progressively more aspect sensitivity.

It is generally recognized that the only satisfactory way to study the frequency dependence of radio-auroral echoes is to use scaled systems. That is, to use antenna systems on the different frequencies which have as nearly as possible identical beams, to use the same pulse lengths and repetition rates, and to have the same sensitivity on all frequencies. Further, it is necessary for the observations to be carried out simultaneously if the information is to be useful, since observations at different times may be of quite different strengths of radio-aurora, and involve different mechanisms of reflection.

Simultaneously, multiple-frequency observations which have been made to study the frequency dependence of echo strengths have been made by Forsyth (1953, see also Currie, Forsyth, and Vawter 1953), Harang and Landmark (1954), Dyce (1955*b*), Forsyth and Vogan (1957), and Collins and Forsyth (1959), and Flood (1960). The experiments of Harang and Landmark, and Dyce were both on two frequencies, with quite different antenna patterns for the two frequencies. The work of Forsyth (1953) was on 56 and 106 Mc/s. The pulse widths were different, and the 56 Mc/s beam was twice as wide as that on the higher frequency. In analyzing the data Forsyth attempted to correct for these differences, but this involves certain assumptions, since the correction depends upon the distribution of the ionization and the mechanisms of reflection. The effect of the different pulse widths on the two frequencies was corrected for by defining a total scattering coefficient per kilometer range in terms of amplitudes normalized to have a value of unity at the mean noise amplitude. Out of a total of 1204 periods of observation during which echoes occurred, 922 corresponded to echoes on 56 Mc/s only, 23 to echoes on 106 Mc/s only, the remaining 259 being simultaneous occurrences on the two frequencies. For the simultaneous observations the amplitude was most frequently greatest for 56 Mc/s, although the ratio of amplitude took on all

measurable values. It appears likely that those observations which indicated a smaller signal on the lower frequency were affected by the presence of selective absorption. Both Forsyth and Vogan, and Collins and Forsyth operated exactly scaled systems on 32.22, 39.22, and 48.82 Mc/s, using forward-scattering. Forsyth and Vogan illustrated their three-frequency observations by means of what they called an XY diagram. If the amplitudes and wavelengths of 32.22, 39.22, and 48.82 Mc/s are designated by A_1, A_2, A_3, and λ_1, λ_2, λ_3, the two ratios X and Y are given by

$$X = \frac{(A_2/\lambda_2)}{(A_3/\lambda_3)}, \qquad Y = \frac{(A_1/\lambda_1)}{(A_2/\lambda_2)}. \tag{2}$$

The division of each amplitude by the wavelength gets rid of the wavelength dependence in the radar equation (1), so that (2) becomes

$$X = \left(\frac{\sigma_2}{\sigma_3}\right)^{\frac{1}{3}}, \qquad Y = \left(\frac{\sigma_1}{\sigma_2}\right)^{\frac{1}{3}}, \tag{3}$$

where σ_1, σ_2, and σ_3 are the scattering coefficients for 32.22, 39.22, and 48.82 Mc/s, respectively. Forsyth and Vogan plotted X vs. Y (XY diagram) for observations obtained during two nights of radio-auroral activity, and these results are shown in Fig. 4. Small values of both X and Y indicate a gradual frequency dependence, whereas large values of both X and Y indicate that the

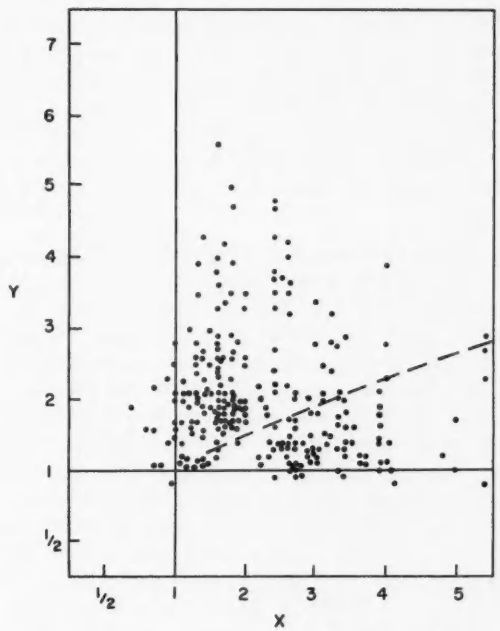

FIG. 4. XY diagram showing the results of Forsyth and Vogan (1957).

scattering coefficient is getting rapidly smaller with frequency. A large value of X together with a small value of Y indicates that the difference between A_2 and A_3 is much greater than that between A_1 and A_2, while a large value of Y with a small value of X indicates the reverse. The observations of Collins and Forsyth (1959) are essentially the same as those of Forsyth and Vogan, except that they find that type A_1 echoes seem to give a large value of Y and small X, while type A_3 has both X and Y small.

Flood (1960) has reported results obtained from a simultaneous, three-frequency study of radio-aurora on 49.17, 143.5, and 226 Mc/s. The two lower frequencies were operated on essentially scaled systems, while the highest frequency used an antenna with a considerably narrower beam, but which was, as nearly as possible, arranged to illuminate the same portion of the ionosphere at the 100-km level. The ratio of total scattering coefficients (as defined by (1)) on 49.7 and 143.5 Mc/s varied from values less than 1 to as large as 1700 (or more), with the over-all average ratio being 41. Echoes on 226 Mc/s occurred only with strong echoes on the other frequencies. On these occasions, the ratio of the scattering coefficients on 143.5 Mc/s to that on 226 Mc/s varied from about 2 to 230, with the average ratio being about 19. It is interesting to note (Flood 1959) that the strongest echoes on 49.7 Mc/s were not accompanied by echoes on 226 Mc/s.

RADIO-AURORAL REFLECTION MECHANISMS

These experimental results can now be examined in relation to the models of auroral ionization developed in Part I. Let us first see how well the results can be explained by a model of auroral ionization consisting of an assembly of similar gaussoids. Of particular interest is the comparison of the frequency dependence of the waves scattered from such a model with that found experimentally, since it will likely provide evidence relating directly to the relative importance of weak scattering (Booker's theory) and critical reflection.

Frequency Dependence

In view of the variety of theoretical curves which can be constructed, it is necessary to have simultaneous measurements with scaled systems on as many frequencies as possible. The most satisfactory results for this purpose are those of Forsyth and Vogan (1957), and Collins and Forsyth (1959). It should be borne in mind, however, that these experimental results were obtained using forwardscatter systems. Whether or not the following analysis applies in detail to forwardscattering, it nevertheless indicates a way of interpreting any future three-frequency backscatter experiments. The formulae developed in Part I can be used with (3) to give expressions for X and Y. These will be different, according as the critical wave number, k_c, for the scatterer is less than k_1, between k_1 and k_2, between k_2 and k_3, or greater than k_3. From Part I if $k_c < k_1$,

$$X_1 = e^{0.364a^2}, \tag{4}$$

$$Y_1 = e^{0.229a^2}. \tag{5}$$

If $k_1 < k_c < k_2$,

$$X_2 = e^{0.364a^2}, \tag{6}$$

$$Y_2 = \frac{2f\left(\frac{k_1^2}{k_c^2}\right)\left[\ln\left(\frac{k_c^2}{k_1^2}\right)\right]^{\frac{1}{2}}}{\pi^{1/2}k_c^2a^2}e^{0.676a^2}. \tag{7}$$

(If $Y_2 < Y_1$, use Y_1. This is necessary, because at frequencies just below the critical frequency, the critically reflecting surface is too small to prevent the wave from penetrating, and the scatter theory then becomes valid. It corresponds to the transition region indicated in Fig. 3 of Part I. The other provisional cases which are given below are also a result of this effect.)
If $k_2 < k_c < k_3$,

$$X_3 = \frac{2f\left(\frac{k_2^2}{k_c^2}\right)\left[\ln\left(\frac{k_c^2}{k_2^2}\right)\right]^{\frac{1}{2}}}{\pi^{1/2}k_c^2a^2}e^{1.04a^2}, \tag{8}$$

$$Y_3 = \frac{f\left(\frac{k_1^2}{k_c^2}\right)}{f\left(\frac{k_2^2}{k_c^2}\right)}\left(\frac{\ln\left(\frac{k_c^2}{k_1^2}\right)}{\ln\left(\frac{k_c^2}{k_2^2}\right)}\right)^{\frac{1}{2}}. \tag{9}$$

(If $X_3 < X_1$ use X_1; if $Y_3 > Y_2$ use Y_2; if $Y_2 < Y_1$, use Y_1.)
If $k_3 < k_c$,

$$X_4 = \frac{f\left(\frac{k_2^2}{k_c^2}\right)}{f\left(\frac{k_3^2}{k_c^2}\right)}\left(\frac{\ln\left(\frac{k_c^2}{k_2^2}\right)}{\ln\left(\frac{k_c^2}{k_3^2}\right)}\right)^{\frac{1}{2}}, \tag{10}$$

$$Y_4 = \frac{f\left(\frac{k_1^2}{k_c^2}\right)}{f\left(\frac{k_2^2}{k_c^2}\right)}\left(\frac{\ln\left(\frac{k_c^2}{k_1^2}\right)}{\ln\left(\frac{k_c^2}{k_2^2}\right)}\right)^{\frac{1}{2}}. \tag{11}$$

(If $X_4 > X_3$ use X_3; if $X_3 < X_1$ use X_1; if $Y_4 > Y_2$ use Y_2; if $Y_2 < Y_1$ use Y_1.)
The resultant values of X and Y (which are functions of a, the scatterer size) are plotted in Fig. 5 for four different strengths of scatterers, illustrating each of the four cases given above. The curve for $k_c = 0.818$ m^{-1} (critical frequency 39.0 Mc/s) represents the upper limit for values of Y associated with an assembly of similar gaussoids. Comparison of these curves with the experimental results obtained by Forsyth and Vogan (1957) as shown in Fig. 4 reveals many experimental points which are not encompassed by these theoretical curves. No points which lie above the broken line shown in Fig. 4 can be explained by an assembly of similar scatterers. In particular, values of Y greater than X still require explanation.

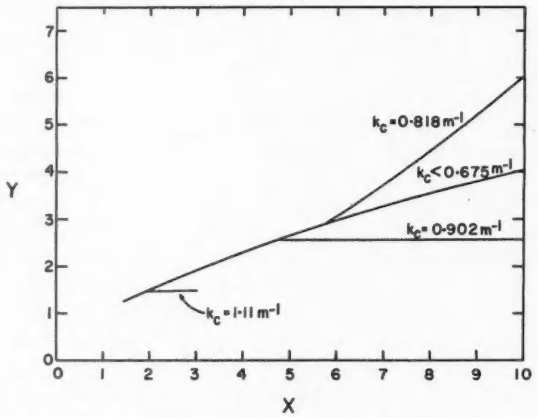

FIG. 5. *XY* diagram for the frequencies used by Forsyth and Vogan (1957), showing curves for various assemblies of similar gaussoids. Values of a range from 1.0 m at $X=1.4$ to 2.5 m for $X=10$.

There are several ways in which this discrepancy might be explained: (i) the results are for forwardscattering, while the theory is for backscattering; (ii) the scatterers are not accurately represented by gaussoids; (iii) some other effect such as multiple scattering or absorption plays a role in the scattering process; (iv) the scatterers are not similar, but their distribution rather involves various sizes and strengths. Each of these possibilities will be considered in turn.

Although it is difficult to develop any accurate theory for forwardscattering, it is not difficult to make a rough estimate of the resulting modifications. To a first approximation, the scattering coefficient for a critically reflecting scatterer reflecting at an angle of 90°, say (a likely angle for the experiments of Forsyth and Vogan), will not be substantially different from that for backscattering. There may be a slight increase in the value of σ due to the greater size of the critically reflecting surface at oblique incidence. This also results in the critical reflection being the mode of reflection at higher frequencies than for backscatter. For weak scattering, the formulae of Part I include the case of forwardscattering. For scattering in the plane normal to the scatterer axis, (6) of Part I becomes

$$\sigma = r_e^2 q^2 e^{-a^2k^2(1-\cos\theta)}, \tag{12}$$

where θ is the angle between the incident and received directions. If $\theta=180°$, we have backscattering, and (12) becomes

$$\sigma = r_e^2 q^2 e^{-2a^2k^2},$$

as before. If $\theta=90°$, then

$$\sigma = r_e^2 q^2 e^{-a^2k^2}. \tag{13}$$

Thus, approximately, all the expressions (4) to (11) can be corrected for forwardscattering by dividing the exponent by 2. The resulting expressions all have exactly the same value, for a given a, as the backscatter expressions with a value of a smaller by a factor $2^{-1/2}$, with the exception of (7) and (8), both of which have values which are one-half of the corresponding values for $2^{-1/2}a$. This has the effect of sliding the rising curves further to the right of the XY diagram. It is thus clear that this correction provides no basis for an explanation of the experimental results above the $Y=X$ line.

It is possible that in using the gaussoid physically unreasonable characteristics have been introduced into the model, and for this reason the model is not applicable. If this is the case, the difficulty could involve only the diffuseness of the boundary of the scatterer, since the shape will have little effect on the frequency dependence of the scatterer, and the size and strength can already be freely varied. It appears likely that for scatterers, which are only a few mean free paths in size, the nature of the electron density distribution will almost certainly be determined by diffusive process, leading to a gaussoidal distribution. Larger irregularities may be formed by other processes, and result in boundaries which are less diffuse, relative to the size of the irregularity, than a gaussoid. However, the sizes shown in Fig. 5 indicate that only the small size scatterers are of importance for values of X and Y less than 5, and hence it is unlikely that there is any basic error in assuming the scatterers to be gaussoids.

In the treatment of scattering given in Part I no consideration was given to the possible influence of multiple scattering. Recent calculations (Moorcroft 1960) suggest that this may be an important effect, particularly in reflection from weak scatterers. The effect of this appears to be to decrease the frequency dependence of weak scattering, and this might justify an upward shift of some of the curves into the region above $Y=X$ on the XY diagram.

Another effect which has not been taken into account is absorption of the radio waves. There is considerable evidence for this in the observations of frequency dependence (Forsyth and Vogan 1957; Flood 1960). The effect of this on a point on the XY diagram is to move it downwards to the left along a line that makes an angle of 45° or more with the X-axis. Such an effect cannot move the curves of Fig. 5 above the $Y=X$ line.

It seems likely that the correct way out of this difficulty lies in choosing an assembly of scatterers having a distribution of sizes and strengths. There are several different types of distribution which we could consider, involving strength alone, both size and strength together (as in the assembly of diffusing scatterers, which was discussed in Part I), or sizes alone (as in the various other assemblies considered at the end of Part I). To explain the observations, a satisfactory distribution must give values of Y greater than X, for small values of both X and Y. This implies that the lowest frequency is reflected much more strongly than the other two frequencies. Distributions such as those considered in Part I have this type of frequency dependence only when radio waves of the lowest frequency are critically reflected. However, none of the assemblies considered in Part I had size distributions with maxima at

more than one size. There are assemblies of this type which have the observed frequency dependence without requiring critical reflection on any of the frequencies. Suitable distributions of this kind appear unlikely to occur in the ionosphere, and will not be considered in this paper, but they cannot be excluded as possibilities by the observations considered here.

Consider an assembly with scatterers of the same size but having different peak electron densities. With a little thought it can be seen that this will smooth out the transition between the two mechanisms, since now the number of scatterers critically reflecting at any given frequency will be a decreasing function of frequency, instead of dropping abruptly to zero at one particular frequency. Such a distribution will be no improvement over the assembly of similar scatterers.

The assembly of diffusing scatterers is a physically reasonable example of an assembly involving a distribution both of size and strength. Values of X and Y for the three frequencies used by Forsyth and Vogan for assemblies of this type are given by curve (*b*) shown in Fig. 6. The parameter which

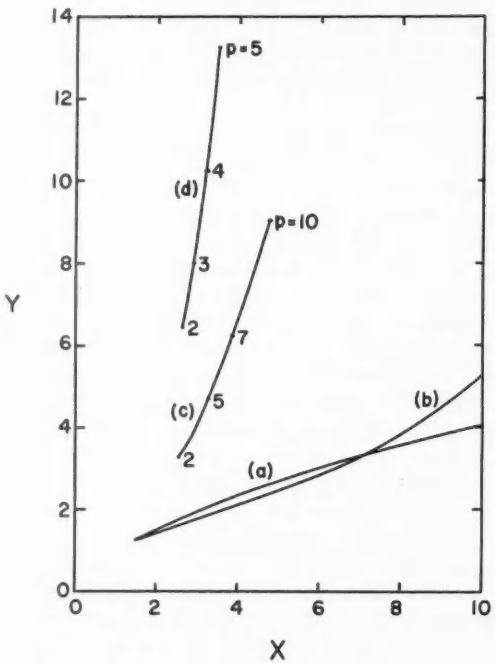

FIG. 6. XY diagram for the frequencies used by Forsyth and Vogan (1957), showing curves for various assemblies of gaussoids. (*a*) Scatter theory for an assembly of similar gaussoids. (*b*) Assembly of diffusing scatterers. (*c*) Assembly of gaussoids having a size distribution given by (41) of Part I; $a_m=4.3$ m, $k_c=0.7$ m^{-1}. (*d*) Assembly of gaussoids having a size distribution given by (41) of Part I; $a_m=5.8$ m, $k_c=0.7$ m^{-1}.

varies along the curve is a_0, the minimum scatterer size. For comparison the scatter theory curve is also shown (curve (*a*)). This distribution is of little help in extending the theoretically predicted regions of the XY diagram.

The distributions considered at the end of Part I involve a distribution of sizes only, the scatterers all having the same peak electron density. This promises to be useful, since, roughly speaking, the weak scattering will tend to be characteristic of the small scatterers, while the nature of the critical reflection will be largely determined by the presence of larger scatterers, resulting in a sharper transition at the critical frequency. The two curves marked (*c*) and (*d*) in Fig. 6 have been calculated for groups of models of this type. As anticipated, this type of assembly leads to a considerably sharper transition than the assembly of similar scatterers and thence to the larger values of Y, just as required. It is not surprising to see that the curve representing assemblies with a greater proportion of larger scatterers leads to the larger value of Y. The different points along the curve correspond to different values of p (see Fig. 7 of Part I for the properties of the size distribution). These curves are both drawn for assemblies with the same value for the critical frequency of the scatterers, 33.2 Mc/s. Increasing the critical frequency (up to the limit of 39.22 Mc/s) has the effect of raising these curves with very little shift in the X-direction. It appears likely that smaller values of a'_m will give lower, flattened curves, covering the major part of the XY diagram. As explained in Part I, these curves have not been computed because they involve more effort, in the form of numerical integration, than the problem warrants. Thus any point in the region to the right of $X=2$ can be filled by any of an infinite number of assemblies having a certain combination of p, k_0, and a'_m.

There are still no theoretical curves lying to the left of $X=2$. Since a value of Y greater than X is required, the reflection on the two higher frequencies must be due to weak scattering. Using this fact, a theoretical lower limit can be placed on X. An assembly of similar scatterers of size $a=1$ m gives a value for X of 1.44. Any smaller values of X could only be obtained with smaller scatterer sizes. If some of the scatterers in this assembly are replaced by larger and thus more strongly frequency-dependent scatterers, the frequency dependence of the assembly as a whole will inevitably increase, and with it the value of X. Thus, for physically reasonable sizes of scatterers, the value of X will be larger than 1.5 and usually larger than 2.0. Figure 3 shows that many echoes have values of X less than 2. These echoes can be readily accounted for by moving the curves in Fig. 6 downward to the left. As mentioned earlier, this is precisely the effect to be expected in the presence of absorption. This appears to be the correct explanation of the frequency dependence of such echoes.

Although the results reported by Flood (1960) are not in a suitable form to examine them in the detail with which we have examined those of Forsyth and Vogan, it is useful to represent them on an XY diagram (Fig. 7). The marked dot indicates the over-all average values of X and Y obtained; the broken line indicates the values of X and Y inside of which fell all of the observations (excluding those which did not include echoes on the higher frequencies).

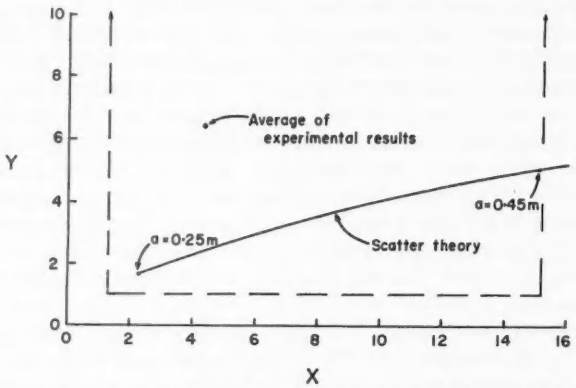

FIG. 7. XY diagram for the frequencies used by Flood (1960), illustrating his results. The curve gives values of X and Y for weak scattering from an assembly of similar gaussoids.

The curve shown in Fig. 7 is for weak scattering, and represents theoretical values of X and Y from assemblies of similar scatterers having the sizes indicated. If the reflections are to be explained on the basis of this curve, the scatterers must have values of a as low as .35 or .40 m. Such sizes are equal to or less than the values of the mean free path and gyro-radius to be expected at heights of 100 or 110 km. Irregularities of such a small size are not likely to persist longer than the collision time, which is of the order of 1 microsecond. It therefore seems physically improbable that the reflection could be caused by such small irregularities. In addition, the position of the average values of X and Y lies significantly above the curve. There is no obvious way in which this observation can be explained in terms of weak scattering alone. Introducing absorption will again shift the curve for weak scattering downwards to the left, making the explanation of the observations even more difficult. It appears likely that these results can be explained by the introduction of assemblies similar to those used to explain the results of Forsyth and Vogan, involving a distribution of sizes of scatterers and critical reflection at 49.7 Mc/s. This is not to say that the observations of Flood contain no instances of weak scattering, but that the general nature of the frequency dependence suggests that critical reflection plays an important part in the explanation of the observations. The curves for such assemblies would be located at very large values of X, well off the region shown in the diagram. The effect of very strong absorption would be to bring the points down into the region of the XY diagram containing the experimental points. This interpretation is supported by the observation by Flood (1959) that the strongest echoes on 49.7 Mc/s are not accompanied by echoes on 226 Mc/s. Such an observation could be explained if 226 Mc/s echoes occurred only when the level of ionization was so intense that the 49.7 Mc/s echoes began to suffer considerable absorption. The form of the results does not allow anything more specific to be said.

From time to time experimental observations which appear to be in agreement with a theory of weak scattering have been taken to imply that critical reflections are excluded from auroral reflections, and that the maximum electron density in auroral ionization is thus less than the critical density for the propagated waves: it is usually considered to depart only slightly from the ionospheric background. It is now clear that such observations do not exclude the presence of auroral irregularities having electron densities considerably in excess of the critical density for radio waves in the 30 to 50 Mc/s range. For example, the theoretical XY curves for an assembly of diffusing scatterers and for an assembly of similar, weakly scattering scatterers (Booker theory) are nearly identical for moderate values of X and Y (see Fig. 6). The first of these models includes strong critically reflecting scatterers, while the second includes none.

Aspect Sensitivity

Until now this discussion has not included any mention of the shape of auroral scatterers. In this regard, there is a great deal of evidence to support the existence of anisotropy of auroral scatterers, but the actual extent of this anisotropy is by no means clearly established. As was pointed out in the discussion of the experimental evidence, both the azimuthal and elevation distributions of echo occurrence, particularly at high latitudes, and in spite of the complications already mentioned, definitely indicate the presence of aspect sensitivity. Also mentioned as evidence of aspect sensitivity, and hence of anisotropy of the scatterers, were the forwardscatter results of Collins and Forsyth (1959). Nevertheless a precise estimate of the anisotropy of auroral ionization is difficult to make. It is perhaps possible to put a rough upper limit on the degree of anisotropy to be expected by assuming that all the angular dependence of auroral echoes is due to the reflection mechanism. Presnell *et al.* (1959) made this assumption to deduce (on the basis of weak scattering theory) from the maximum observed deviation angles from perpendicularity to the magnetic field lines which they observed on 218, 398, and 780 Mc/s, a "length" of 3.2 meters, corresponding in the notation of this paper to a value for "ah". This implies, from the physical limitations on a, an axial ratio of 4 or 5. This result could be considerably in error, since the data used by Presnell *et al.* were not taken simultaneously on the different frequencies, nor with scaled systems.

More recently, Greenhow, Neufeld, and Watkins (1960), using results obtained on 36 Mc/s with the Jodrell Bank radiotelescope, and using a theory of weak scattering, deduced a value for ah of about 26 meters. Their measurements are shown in Fig. 3. This gives a maximum value for h of about 30, considerably different from the value suggested by the results of Presnell *et al.* Greenhow *et al.* suggested that this discrepancy resulted from the lack of small aspect angles in Alaska, which would not give a proper base against which to judge the results. It is interesting to compare the results obtained by Greenhow *et al.* with theoretical curves based on the models of Part I. This has been done in Figs. 8*a*, 8*b*, and 8*c*, where the corrected results of Greenhow *et al.* are

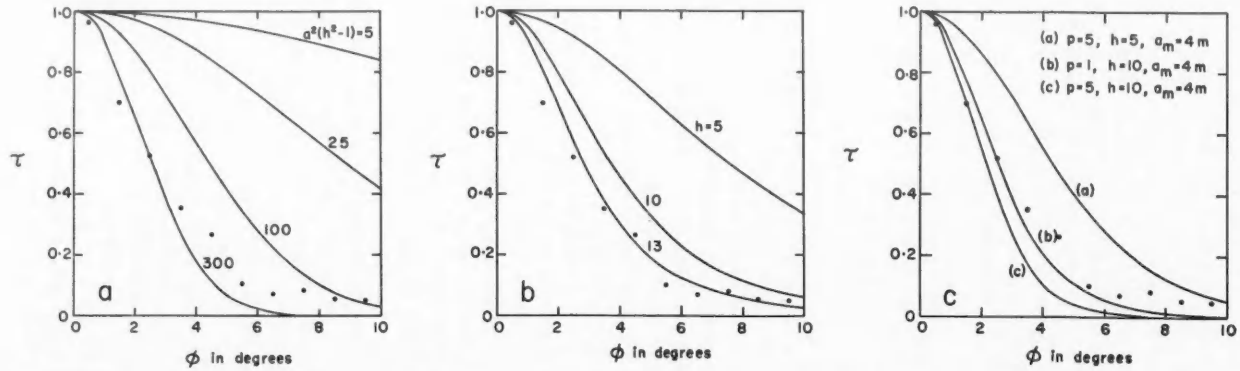

FIG. 8. Aspect sensitivity for (*a*) scatter theory for an assembly of similar gaussoids; (*b*) ray theory (critical reflection) for an assembly of gaussoids having the same peak electron density; (*c*) scatter theory for an assembly of gaussoids having a size distribution given by (41) of Part I. The dots show the corrected results of Greenhow *et al.* (1960).

compared with theoretical curves for weak scattering, ray theory, and weakly scattering assemblies with distributed sizes, respectively. It should be observed that the curves for the ray theory are uncorrected for the effect of the function $\delta(\phi, h, k'^2)$ which was discussed in Part I. Preliminary studies of the nature of the function $\delta(\phi, h, k'^2)$ indicate that its inclusion would markedly change the shape of the curves in Fig. 7*c*, probably enough to move the $h=5$ curve down to or past the indicated position of the $h=10$ curve. It seems that all three theories are about equally capable of explaining the results of Greenhow *et al.* These experimental observations do not decrease as rapidly with increasing angle as any of the theoretical curves. The curves for the ray theory are the most similar in shape. The scattering medium may consist of a mixture of critically reflecting and weak scattering irregularities (quite possible, since these results are a statistical distribution over many different events), and the experimental points may not be satisfactorily corrected for such effects as the geographical distribution of the ionization and the volume of ionization intercepted by the beam as it looks in different directions. Both these effects may contribute to the observed difference between the experimental points and the theoretical curves. However the results are interpreted, they imply a value for h between 5 and 10.

On the basis of the discussion of the effect of the magnetic field on diffusion given in Part I, there is no reason to expect that the degree of anisotropy should be constant over the scattering volume (or, in view of the variation of the collision frequency with height, that the length of irregularities should be constant throughout the scattering volume). This will depend, of course, on the range of heights over which the echoes are obtained, but there appears to be no reason why the scatterers at, say, 100 km, could not be isotropic, while those at 110 or 115 km might be very much elongated along the field lines. The bistatic observations of Collins and Forsyth (1959) suggest two or three different types of aspect sensitivity.

CONCLUSIONS

In spite of the relatively few experimental observations which are relevant to the determination of the characteristics of auroral ionization, it has been possible to arrive at several important conclusions concerning this ionization. The existence of critical reflection at frequencies between 30 and 50 Mc/s appears to be established. This implies electron densities which at times reach values as large as 3×10^{13} electrons/m^3. This value does not seem to be incompatible with densities deduced on the basis of the intensity of auroral light. There is unquestionable evidence that the scatterers composing the auroral ionization are elongated along the lines of the magnetic field, but the extent of this elongation is by no means settled. Although there is no reason to expect that the degree of anisotropy is constant throughout the auroral ionization, the characteristic axial ratio of auroral scatterers appears to be between 5 and 10. The scatterers which are important for the reflection of radio waves have sizes of the order of a few meters (by size is meant that distance measured from the axis of the scatterer, in a plane normal to it, at which the electron

density is $1/e$ of its maximum value), the experimental results being consistent with a distribution of sizes as given by (41) of Part I, having the values of a_m range from 2 to 5 m or more, and those of p range from 1 to 10.

It is clear from the nature of the experimental observations used to obtain them, that the characteristics given above for auroral ionization can not be considered to be final. The purpose of this paper has been simply to indicate a broader point of view in considering the possibilities for an auroral model, and in so doing to indicate the lack of adequate observational evidence on which to base a model of radio-aurora. It is evident, for example, that none of the observations made to date are really suitable for studying the aspect sensitivity of the reflection mechanism. What is needed is an experimental arrangement which will measure the strength of the signal reflected from the *same* volume at different angles. Similarly, the frequency dependence of auroral reflections will not be free of ambiguities until scaled systems are operating on three or more frequencies simultaneously. It appears that it would be particularly valuable if these frequencies were chosen within about 10 megacycles of each other in the frequency range of 50 to 100 Mc/s. Because of the nature of the differences between the predicted frequency dependence of the various auroral models, as well as a superimposed effect due to absorption, distinctions are better made with closely spaced frequencies than widely separated ones.

It is hoped that this paper has also illustrated the usefulness of the particular approach to models of ionization used in Part I. This approach allows inclusion in one treatment of both critical reflection and weak scattering and enables one to discuss the experimental results in terms of what seem to the author to be physically significant parameters.

ACKNOWLEDGMENTS

During the course of the research for both these papers the author has benefited from discussions with several members of the faculty of the Department of Physics at the University of Saskatchewan. He is particularly indebted to Dr. A. Kavadas for many interesting and profitable discussions. Dr. P. A. Forsyth, who supervised this research, provided stimulating guidance and unceasing encouragement, for which the author is sincerely grateful. The two papers are based in part upon a thesis submitted to the Faculty of Graduate Studies of the University of Saskatchewan in partial fulfilment of the degree of Master of Science. This research was carried out with the assistance of two N.R.C. scholarships, the author receiving a bursary in 1958 and a studentship in 1959.

REFERENCES

ASPINALL, A. and HAWKINS, G. S. 1950. J. Brit. Astron. Assoc. **60**, 130.
BOOKER, H. G. 1956. J. Atmospheric and Terrest. Phys. **8**, 204.
BOOKER, H. G., GARTLEIN, C. W., and NICHOLS, B. 1955. J. Geophys. Research, **60**, 1.
BOWEN, E. G. 1954. A textbook of radar (Cambridge).
BULLOUGH, K. and KAISER, T. R. 1954. J. Atmospheric and Terrest. Phys. **5**, 189.
——— 1955. J. Atmospheric and Terrest. Phys. **6**, 198.
COLLINS, C. and FORSYTH, P. A. 1959. J. Atmospheric and Terrest. Phys. **13**, 315.
CURRIE, B. W., FORSYTH, P. A., and VAWTER, F. E. 1953. J. Geophys. Research, **58**, 179.

DYCE, R. B. 1955*a*. J. Geophys. Research, **60**, 317.
——— 1955*b*. Tech. Rept. No. 23, School of Electrical Engineering, Cornell University, Ithaca, New York.
FLOOD, W. A. 1959. Unpublished.
——— 1960. J. Geophys. Research, **65**, 2261.
FORSYTH, P. A. 1953. J. Geophys. Research, **58**, 53.
——— 1960. Can. J. Phys. **38**, 593.
FORSYTH, P. A. and VOGAN, E. L. 1957. J. Atmospheric and Terrest. Phys. **10**, 215.
GREENHOW, J. S., NEUFELD, E. L., and WATKINS, C. D. 1960. J. Atmospheric and Terrest. Phys. **18**, 174.
HARANG, L. and LANDMARK, B. 1954. J. Atmospheric and Terrest. Phys. **4**, 332.
HELLGREN, G. and MEOS, J. 1952. Tellus, **3**, 249.
HERLOFSON, N. 1947. Nature, **160**, 867.
KAISER, T. R. 1956. The airglow and the aurorae (Pergamon Press), p. 156.
——— 1957. J. Geophys. Research, **62**, 297.
LITTLE, C. G., RAYTON, W. M., and ROOF, R. B. 1956. Proc. I. R. E. **44**, 992.
LOVELL, A. C. B., CLEGG, J. A., and ELLYETT, C. D. 1947. Nature, **160**, 372.
MCNAMARA, A. G. 1959. Private communication.
MEOS, J. and OLVING, S. 1958. Report No. 43, Research Laboratory of Electronics, Chalmers University of Technology, Gothenburg, Sweden.
MOORCROFT, D. R. 1960. Unpublished.
——— 1961. Can. J. Phys. **39**. This issue.
PRESNELL, R. I., LEADABRAND, R. L., PETERSON, A. M., DYCE, R. B., SCHLOBOHM, J. C., and BERG, M. R. 1959. J. Geophys. Research, **64**, 1179.
SCHLOBOHM, J. C., LEADABRAND, R. L., DYCE, R. B., DOLPHIN, L. T., and BERG, M. R. 1959. J. Geophys. Research, **64**, 1191.
UNWIN, R. S. and GADSDEN, M. 1957. Nature, **180**, 1469.

SCATTERING OF RADIO WAVES BY AN IONIZED GAS IN THERMAL EQUILIBRIUM IN THE PRESENCE OF A UNIFORM MAGNETIC FIELD[1]

J. A. FEJER

ABSTRACT

In an earlier paper (Fejer 1960) a theory was developed for the scattering of radio waves by the electron density fluctuations that exist in an ionized gas in thermal equilibrium. The theory treated only the extreme cases where the "characteristic scale" of the scattering irregularities is either very much larger or very much smaller than the Debye length. The presence of only one type of singly charged ion was considered and the ion and electron temperatures were assumed equal. The effects of an external magnetic field were not taken into account.

These earlier limitations are removed in the present paper and the effects of an external magnetic field are taken into account.

It is shown that the total power is independent of the magnetic field and an expression for the frequency spectrum of scattered power in the presence of a uniform magnetic field is obtained. Useful approximations to this expression are derived for various limiting cases of interest.

It is concluded that the magnetic field need not be taken into account in the interpretation of past observations by Bowles (1958, 1959) and by Pineo, Kraft, and Briscoe (1960). In future experiments, however, particularly at great heights, the effect of the magnetic field could be considerable.

1. INTRODUCTION

Gordon (1958) suggested that radio waves incident on the ionosphere at frequencies well above the critical frequency are scattered by irregularities in electron density which are present even under conditions of thermal equilibrium. His simple theory predicted that the scattered power would be proportional to the electron number density, and that the width of the frequency spectrum would be determined by a Doppler spread caused by the thermal velocities of the electrons.

Observations of this phenomenon by Bowles (1958, 1959) and by Pineo, Kraft, and Briscoe (1960) have approximately confirmed Gordon's predictions about the scattered power but showed the frequency spectrum to be much narrower than anticipated.

Bowles (1958) has explained this discrepancy by showing that, under the conditions of the experiments so far performed, the Doppler spread is determined by the thermal velocities of the ions although the electrons are responsible for the scattering. Subsequently several authors (Fejer 1960; Dougherty and Farley 1960*a*; Renau 1960; and Salpeter 1960*a*, *b*) have developed the theory of this phenomenon, and using a variety of methods have arrived at identical conclusions. The aim of the present paper is first to remove certain limitations from one of these developments (Fejer 1960), and then to extend it to include the effects of the magnetic field.

One of the most serious limitations of the earlier treatment (Fejer 1960)

[1]Manuscript received January 11, 1961.
Contribution from the Defence Research Board Theoretical Studies Group, Ottawa, Canada.
Can. J. Phys. Vol. 39 (1961)

was the assumption that the Debye length was either very much greater or very much smaller than the "characteristic scale" of the scattering irregularities. In removing this limitation and generalizing the treatment to several types of ions and to unequal values of the ion and electron temperature no fundamentally new results are obtained which were not already present, implicitly or explicitly, in two of the earlier treatments (Dougherty and Farley 1960*a*; Salpeter 1960*b*). There are, however, two reasons for devoting Sections 2–5 to the generalization of Fejer's earlier work. The first reason is that the generalized theory is needed for the treatment of magnetic effects in later sections. The second no less important reason is that the new treatment makes fewer assumptions and is therefore simpler and of a more general applicability.

The basic assumptions are that in the absence of Coulomb forces, the particles are randomly distributed, and that their velocity distribution is Maxwellian. (In principle a different velocity distribution could be assumed and would then lead to different results.) For purposes of the present paper the particles are said to be randomly distributed if their probability density in configuration space is independent of the co-ordinates of all the particles.

It is further assumed that the electric field acting on a particle is, for the present purposes, well approximated by the Coulomb field of the other particles. It is difficult to justify this assumption fully without including the effect of induced electric fields in the theory first and then showing that their effect on the result is small. It is easily shown that, if the random thermal motion were unperturbed by forces acting on the electrons and ions then the electric field caused by the thermal motion would be very much smaller than the Coulomb field for thermal velocities much smaller than the velocity of light. It is further possible to show that for the parameters of interest the electric fields, induced by the magnetic field of currents due to the unperturbed random thermal motion, are insufficient to perturb that motion appreciably. Such considerations make it seem likely that the perturbation of the random thermal motion and the resulting electron densities are mainly determined by the Coulomb forces.

In Sections 6–8, the effects of a uniform magnetic field are taken into account in the calculation of the spectral power density. The total scattered power could be calculated from the results of Section 7 by integrating the spectral power density over the whole frequency spectrum. An alternative method of calculation for the total scattered power was given in the Appendix of the earlier treatment (Fejer 1960). That treatment is not altered by the presence of a magnetic field if the electric field energy is taken to be only that contained in the Coulomb field. Therefore the results derived there for the total scattered power are not affected by the magnetic field within the limits of the present approximation. The author would, however, like to take this opportunity to point out that the result derived in that paper for the total scattered power was in error. The nature and cause of this error was explained in an Erratum in the September issue of Canadian Journal of Physics. The correct form of Fejer's (1960) equation (8) (also derived by Renau (1960) and by Salpeter (1960*b*)), is

$$\sigma = \sigma_e N \frac{[4\pi l_D \sin(\theta/2)]^2+\lambda^2}{[4\pi l_D \sin(\theta/2)]^2+2\lambda^2}$$

as already given in the above-mentioned Erratum.

It is of interest to mention that Dougherty and Farley (1960*b*) have also extended their earlier theory (Dougherty and Farley 1960*a*) to take the effect of the magnetic field into account. They first derive an exact expression for the spectral power density without approximating the forces acting on the electrons by the Coulomb forces. They then show by contour integration of this expression that the total scattered power is not affected by the magnetic field and is given by an expression identical with the above corrected form of Fejer's equation (8). In subsequent parts of their paper, Dougherty and Farley (1960*b*) make the same approximations as the present paper in order to simplify their rather cumbersome exact expressions for the spectral power density. They derive a sufficient condition for the validity of this approximation but do not show that the condition is also a necessary one. Their condition is satisfied in most ionospheric applications and thus their treatment provides further justification for the approximations made here. Results similar to those of the present paper were also obtained separately by Renau, Salpeter, and Hagfors (private communication).

The result for the spectral power density is given in two forms in Section 7, as an integral and as an expansion into tabulated functions. Either of these forms could be used for a computation of the frequency spectrum.

A better insight into the effects of the magnetic field is gained by considering certain extreme cases where the results can be expressed more simply. Two such extreme cases are considered in Section 8, where it is assumed that the gyro-radius is either very much greater or very much smaller than the "characteristic scale" of the scattering irregularities. The approximations obtained for these two extreme cases are probably sufficiently accurate for most ionospheric applications and in addition provide a good insight into the nature of the spectrum even in intermediate cases. Computations would be needed for more accurate results.

2. THE TOTAL SCATTERED POWER FOR RANDOMLY DISTRIBUTED ELECTRONS

It may be shown (for example, from equation (4) of Fejer 1960) that for an ionized gas, for sufficiently high frequencies, for weak scattering by irregularities in electron density, and for variations of electron density in time which have dominating periodic components much longer than the period of the incident radio wave

$$\sigma = \sigma_e V^{-1} \overline{\left| \int_V \Delta N_1(\mathbf{r},t) \exp[i(\mathbf{k}_s - \mathbf{k}_0)\cdot\mathbf{r}] d^3\mathbf{r} \right|^2} \tag{1}$$

where σ, the scattering cross section of the gas, is defined as the power per unit incident power density, unit solid angle, and unit scattering volume, and where V is the scattering volume, ΔN_1 is the deviation of the electron number density from its average value N_1, where the suffix 1 denotes electrons, $\mathbf{k}_0$ is

the propagation vector of the incident wave, $\mathbf{k}_s$ is a vector of the same magnitude as $\mathbf{k}_0$ which points in the direction of scattering, $\mathbf{r}$ is the radius vector to a point in the scattering volume, $d^3\mathbf{r}$ is the volume element in the scattering volume, and $\sigma_e = (\mu_0 e^2 \sin\gamma/4\pi m_1)^2$ is the Thompson scattering coefficient of an electron. In the latter expression, μ_0 is the permeability of free space, $-e$ is the electronic charge, γ is the angle between the electric field vector of the incident wave and the direction of scattering, and m_1 is the electronic mass. The bar in equation (1) indicates either averaging in time or an ensemble average. It is convenient to introduce the vector $\mathbf{k} = \mathbf{k}_s - \mathbf{k}_0$.

It is relatively simple to show (Kahn 1959) that for randomly distributed stationary particles

$$\overline{\left|\int_V \Delta N_1 \exp(i\mathbf{k}\cdot\mathbf{r}) d^3\mathbf{r}\right|^2} = N_1 V \tag{2}$$

where the bar now indicates an ensemble average. Substitution of (2) into (1) yields

$$\sigma = N_1 \sigma_e. \tag{3}$$

Equation (3) expresses the result originally stated and proved by Rayleigh (1871) that the power scattered by n random scatterers in any direction other than the direction of the incident wave is on the average n times the power scattered by a single scatterer. Rayleigh's proof is based on the fact that the fields due to randomly distributed scatterers have random phases.

The above step leading from equation (2) to equation (3) could be reversed in order to derive the mean square value of the spatial Fourier component of electron density from a knowledge of the scattering cross section. Such a reversed procedure is useful for some purposes and is followed in Sections 3 and 4. In Section 3 the frequency spectrum of scattered power for randomly distributed electrons is derived and exemplified by application to a Maxwellian gas. In Section 4 the space–time Fourier component of the number density for random scatterers is then derived from the frequency spectrum of scattering.

3. THE FREQUENCY SPECTRUM OF SCATTERED POWER FOR RANDOMLY DISTRIBUTED ELECTRONS IN THE ABSENCE OF COLLISIONS

The frequency spectrum of the scattered power may be calculated by dividing the electrons into groups which have almost the same velocity component in the $\mathbf{k}$ direction and therefore produce almost the same Doppler shift. The scattered power in each group is given by equation (3), with N_1 replaced by the mean number density of electrons within the group. If $f(v)$ is the normalized velocity-component distribution in the direction of the $\mathbf{k}$ vector, then this mean number density is $N_1 f(v)dv$ for the group that has velocity components between v and $v+dv$. The Doppler shift for this group of scattering electrons is

$$\omega_s - \omega_0 = kv \tag{4}$$

where ω_0 is the angular frequency of the incident wave, and ω_s the angular

frequency of the scattered wave. Abbreviating $\omega = \omega_s - \omega_0$, one obtains for the scattering cross section $\sigma_\omega d\omega$ of this group with the aid of equation (3)

$$\sigma_\omega d\omega = N_1 f(v) dv \sigma_e \tag{5}$$

where σ_ω satisfies

$$\sigma = \int \sigma_\omega d\omega. \tag{6}$$

Equations (4) and (5) yield the expression

$$\sigma_\omega = N_1 f(\omega/k)\sigma_e/k \tag{7}$$

for the spectrum function σ_ω. For a Maxwellian distribution

$$f(v) = (m_1/2\pi K T_1)^{\frac{1}{2}} \exp(-m_1 v^2/2KT_1) \tag{8}$$

where T_1 is the temperature of the electrons and K is Boltzmann's constant, and then

$$\sigma_\omega = (N_1\sigma_e/k)(m_1/2\pi K T_1)^{\frac{1}{2}} \exp(-m_1\omega^2/2KT_1k^2). \tag{9}$$

4. THE SPACE-TIME FOURIER COMPONENT FOR RANDOM SCATTERERS

The number density deviation ΔN from the mean may always be expressed as a Fourier integral in four dimensions

$$\Delta N(\mathbf{r},t) = \int s(\omega,\mathbf{k}) \exp[i(\omega t - \mathbf{k}.\mathbf{r})] d\omega d^3\mathbf{k}. \tag{10}$$

A simple and general relationship between the space–time Fourier component, defined by (10), and the frequency spectrum σ_ω will be derived in this section.

For the mathematical convenience of keeping $s(\omega,\mathbf{k})$ finite the deviations ΔN are assumed to vanish outside a finite time interval t_0 which can be made arbitrarily large compared with the period of interest. Similarly the deviations ΔN are assumed to vanish outside a finite volume V.

In equation (10) the deviations ΔN are decomposed into travelling density waves with different frequencies ω and wave numbers $\mathbf{k}$. Density waves of angular frequency ω (and the correct wave number) are then responsible for scattered radio waves of angular frequency $\omega_0+\omega$.

The inverse form of equation (10) with respect to $\mathbf{k}$ is

$$\int_{-\infty}^{\infty} s(\omega,\mathbf{k}) \exp(i\omega t) d\omega = (2\pi)^{-3} \int_V \Delta N \exp(i\mathbf{k}.\mathbf{r}) d^3\mathbf{r}. \tag{11}$$

Equations (10) and (11) are valid for any type of particle. If the particles are electrons and if only those density waves, whose angular frequency lies in the small but finite interval between ω and $\omega+\Delta\omega$ are considered, then the density deviation $\Delta_\omega N_1$ corresponding to this group of density waves satisfies

$$\int_{\omega}^{\omega+\Delta\omega} s_1(\omega,\mathbf{k}) \exp(i\omega t) d\omega = (2\pi)^{-3} \int_V \Delta_\omega N_1 \exp(i\mathbf{k}.\mathbf{r}) d^3\mathbf{r}\,. \tag{12}$$

This group of density waves is then responsible for scattered radio waves with angular frequencies between $\omega_0+\omega$ and $\omega_0+\omega+\Delta\omega$. The power scattered by these waves is then from equation (1)

$$\int_{\omega}^{\omega+\Delta\omega} \sigma_\omega d\omega = \sigma_e V^{-1} \overline{\left| \int_V \Delta_\omega N_1 \exp(i\mathbf{k}\cdot\mathbf{r}) d^3\mathbf{r} \right|^2} \cong \sigma_\omega \Delta\omega \tag{13}$$

or by combination of (12) and (13)

$$\sigma_\omega \Delta\omega = \sigma_e V^{-1} (2\pi)^6 \overline{\left| \int_{\omega}^{\omega+\Delta\omega} s_1(\omega,\mathbf{k}) \exp(i\omega t) d\omega \right|^2} \tag{14}$$

where the bar indicates averaging in time over the time interval between $t = 0$ and $t = t_0$ which is approximately the time interval over which the function $u(t)$ defined by

$$u(t) = (2\pi)^{-\frac{1}{2}} \int_{\omega}^{\omega+\Delta\omega} s_1(\omega,\mathbf{k}) \exp(i\omega t) d\omega \tag{15}$$

has non-vanishing values, if $t_0 \gg (\Delta\omega)^{-1}$. If equation (15) is satisfied then by a well-known theorem on Fourier transforms

$$\int_{-\infty}^{\infty} |u|^2 dt = \int_{\omega}^{\omega+\Delta\omega} |s_1(\omega,\mathbf{k})|^2 d\omega \cong t_0 \overline{|u|^2}$$

and a combination of this equation with (14) leads to

$$\sigma_\omega = (2\pi)^7 \sigma_e V^{-1} t_0^{-1} \overline{|s_1(\omega,\mathbf{k})|^2} \tag{16}$$

where

$$\overline{|s_1(\omega,\mathbf{k})|^2} = (\Delta\omega)^{-1} \int_{\omega}^{\omega+\Delta\omega} |s_1(\omega,\mathbf{k})|^2 d\omega.$$

The bar in equation (16) must therefore be interpreted as an average over a small but finite angular frequency range $\Delta\omega$ in the vicinity of ω. The quantity $|s_1(\omega,\mathbf{k})|^2$ varies rapidly and irregularly with frequency in the interval between ω and $\omega+\Delta\omega$ but its average value is well defined.

The mean square value $\overline{|s_{r1}|^2}$ of the space–time Fourier component of randomly distributed electrons may now be obtained from a combination of equations (9) and (16)

$$\overline{|s_{r1}(\omega,\mathbf{k})|^2} = (2\pi)^{-7} V t_0 N_1 k^{-1} (m_1/2\pi K T_1)^{\frac{1}{2}} \exp(-m_1\omega^2/2k^2 K T_1) \tag{17}$$

where the mean value of $|s_{r1}(\omega,\mathbf{k})|^2$ is formed over a small frequency range which, however, is large compared to t_0^{-1}. Expression (17) is by no means restricted to electrons and is equally valid for the Fourier component of the number density for any type of particle as long as the velocity distribution is Maxwellian and the positions are random. An alternative direct derivation of an equation similar to (17), which does not use the concepts of scattering and Doppler shifts, is given by Dougherty and Farley (1960*a*) in their Appendix.

The subscript r in s_{r1} has been used to distinguish this space–time Fourier component, which would exist if the electrons were randomly distributed in space, from the actually existing space–time Fourier components s_1.

5. FREQUENCY SPECTRUM OF SCATTERED POWER FOR A COLLISION-FREE PLASMA

In the derivation of equation (17) it was assumed that the particles move in straight lines at constant velocity. This can be true only if there are no forces acting on the particles. The particles of a plasma are charged, however, and there are electrostatic forces acting on them. No external magnetic field is assumed in this section and the magnetic field of the particles themselves is neglected. The electrostatic forces modify the motion of the particles and therefore also modify the spectrum of scattered power. Fejer (1960) has shown how this modification to the frequency spectrum of scattering can be introduced by a correction factor. His treatment, which was restricted to very small values of the Debye length, is generalized here.

Let the mean number density of electrons in the plasma be N_1, and let the charge of the jth type ion be $Z_j e$, and its mean number density N_j, so that

$$\sum_{j=1}^{n} Z_j N_j = 0 \tag{18}$$

where $Z_1 = -1$ (for electrons).

If, in the absence of electrostatic forces, the particles were randomly distributed with a Maxwellian velocity distribution, the mean square space–time Fourier component of the electron number density would be given by (17). In general, the mean square space–time Fourier component of the number density for the jth type ion would be

$$\overline{|s_{rj}(\omega,\mathbf{k})|^2} = (2\pi)^{-7} V t_0 N_j k^{-1} (m_j/2\pi K T_j)^{\frac{1}{2}} \exp(-m_j\omega^2/2k^2 K T_j). \tag{19}$$

The real problem, however, is the determination of the mean square space–time Fourier component $\overline{|s_1(\omega,\mathbf{k})|^2}$ for electrons in the presence of the electrostatic forces, having obtained a knowledge of $\overline{|s_{rj}(\omega,\mathbf{k})|^2}$ for the jth type of charged particle in the absence of electrostatic forces. If this more realistic quantity $\overline{|s_1(\omega,\mathbf{k})|^2}$ were obtained, the spectrum function of scattering σ_ω would be given by equation (16).

The meaning of the quantities s is made clear by equation (10); they are associated with elementary number density deviations of the form $s(\omega,\mathbf{k})\exp[i(\omega t - \mathbf{k}.\mathbf{r})]d\omega d^3\mathbf{k}$. In the following calculation, the quantities s are taken to be these elementary number density deviations, although the factors $\exp[i(\omega t - \mathbf{k}.\mathbf{r})]d\omega d^3\mathbf{k}$ are omitted. The quantities $s_{r1}, s_{r2}, \ldots, s_{rn}$ are given by equation (19), and represent number density deviations in the absence of electrostatic forces. A new set of quantities $s_{t1}, s_{t2}, \ldots, s_{tn}$ are introduced and are taken to represent the elementary number density deviations which would arise if the electrostatic forces acting on the particles were taken to act on a uniform distribution of particles. The elementary number density deviations $s_1, s_2, \ldots, s_n$ actually present may then be equated, within the accuracy of a linear approximation, to the sum of the deviations s_{rj} which would have occurred in the absence of the fluctuating electric field, and the

deviations s_{tj} which would have been caused by the fluctuating electric field if it had acted on a uniform distribution of particles. Thus:

$$s_j = s_{rj} + s_{tj}. \tag{20}$$

The fluctuating electric field has the charge density

$$e \sum_{j=1}^{n} Z_j s_j$$

as its source, and so is proportional to this quantity. Similarly the quantities s_{tj} must be proportional to the electric field and therefore may be expressed by

$$s_{tj} = \xi_j \sum_{q=1}^{m} Z_q s_q \tag{21}$$

where the ξ are factors of proportionality which remain to be calculated.

Multiplication of equations (20) by Z_j and summation over j results after substitution of s_{tj} from (21) in

$$\sum_{j=1}^{n} Z_j s_j = \sum_{j=1}^{n} Z_j s_{rj} + \left(\sum_{j=1}^{n} Z_j \xi_j\right)\left(\sum_{q=1}^{n} Z_q s_q\right) \tag{22}$$

or

$$\sum_{j=1}^{n} Z_j s_j = \left(\sum_{j=1}^{n} Z_j s_{rj}\right) \Big/ \left(1 - \sum_{j=1}^{n} Z_j \xi_j\right). \tag{23}$$

Therefore, from (20), (21), and (23)

$$s_1 = \frac{1 - \sum_{j=2}^{n} Z_j \xi_j}{1 - \sum_{j=1}^{n} Z_j \xi_j} s_{r1} + \frac{\xi_1}{1 - \sum_{j=1}^{n} Z_j \xi_j} \sum_{j=2}^{n} Z_j s_{rj}. \tag{24}$$

Since the s_{rj} in equation (24) are statistically independent and of random phase

$$\overline{|s_1|^2} = \left| \frac{1 - \sum_{j=2}^{n} Z_j \xi_j}{1 - \sum_{j=1}^{n} Z_j \xi_j} \right|^2 \overline{|s_{r1}|^2} + \left| \frac{\xi_1}{1 - \sum_{j=1}^{n} Z_j \xi_j} \right|^2 \sum_{j=2}^{n} Z_j^2 \overline{|s_{rj}|^2}. \tag{25}$$

This is the required general equation for $\overline{|s_1(\omega,\mathbf{k})|^2}$. It is equally valid in the presence or in the absence of the magnetic field.

For the present section, then, there remains only the calculation of the factors of proportionality ξ_j in the absence of an external magnetic field. In this calculation one uses Liouville's equation

$$\partial W'/\partial t + \mathbf{v}.\operatorname{grad}_{\mathbf{r}} W' + \mathbf{F}_j.\operatorname{grad}_{\mathbf{v}} W' = 0 \tag{26}$$

where W' is the distribution function of the particle type considered, and

$\mathbf{F}_j$ is the force per unit mass. The direction of the x-axis will be taken parallel to $\mathbf{k}$ for convenience and a force per unit mass proportional to $\exp[i(\omega t-\mathbf{k}.\mathbf{r})]$ will be assumed.

The electric field $\mathbf{E}$ responsible for the force per unit mass $\mathbf{F}_j = Z_j e\mathbf{E}/m_j$ has its source in the charge density

$$e\sum_{j=1}^{n} Z_j s_j$$

and therefore

$$\epsilon_0 \operatorname{div}\mathbf{E} = -ik\epsilon_0 E = e\sum_{j=1}^{n} Z_j s_j \tag{27}$$

where ϵ_0 is the dielectric constant of free space.

If the velocity distribution of the unperturbed gas is assumed Maxwellian, one may write

$$W' = (1+W)(m_j/2\pi KT_j)^{3/2}\exp(-m_j v^2/2KT_j) \tag{28}$$

where W is a perturbation which is a function of velocity, position, and time.

If (28) is substituted into (26), one obtains after linearization,

$$\partial W/\partial t+v_x\partial W/\partial x-(m_j/KT_j)v_x F_j = 0. \tag{29}$$

Substituting the force per unit mass from (27) into (29) gives

$$i\omega W-ikv_x W+(m_j v_x Z_j e^2/KT_j ik\epsilon_0 m_j)\sum_{j=1}^{n} Z_j s_j = 0. \tag{30}$$

Solving (30) for W

$$W = \frac{Z_j e^2\sum_{j=1}^{n} Z_j s_j}{kKT_j\epsilon_0}\frac{v_x}{\omega-kv_x}. \tag{31}$$

The perturbation $(m_j/2\pi KT_j)^{3/2}W\exp(-m_j v^2/2KT_j)$ in the distribution function W' must be integrated over velocity space to obtain the fractional perturbation s_{tj}/N_j in the number density. Using (31) this leads to

$$s_{tj} = \left(\frac{m_j}{2\pi KT_j}\right)^{\frac{1}{2}}\frac{Z_j e^2 N_j\sum_{j=1}^{n} Z_j s_j}{k^2 KT_j\epsilon_0}\int_{-\infty}^{\infty}\frac{v_x}{\omega-kv_x}\exp\left(-\frac{m_j v_x^2}{2KT_j}\right)dv_x. \tag{32}$$

The integrand in (32) has a pole at $v_x = \omega/k$. The path of integration near the pole can be decided by letting ω have a very small negative imaginary part so that the waves $\exp[i(\omega t-\mathbf{k}.\mathbf{r})]$ represent waves growing in time which at $t = -\infty$ had negligible amplitude. (The more rigorous method of using Laplace transforms has been described by Landau (1946).)

The integral in (32) may then be replaced by the principal value minus πi times the residue of the pole. This leads to

$$s_{tj} = Z_j\left(\sum_{q=1}^{n} Z_q s_q\right)(N_j e^2/k^2\epsilon_0 KT_j)\Big[-1+2(\omega/\Omega_j)\exp(-\omega^2/\Omega_j^2)\int_0^{\omega/\Omega_j}\exp y^2 dy+i\pi^{\frac{1}{2}}(\omega/\Omega_j)\exp(-\omega^2/\Omega_j^2)\Big] \tag{33}$$

where

$$\Omega_j = k(2KT_j/m_j)^{\frac{1}{2}}. \tag{34}$$

Combination of (33) with (21) gives,

$$\xi_j = Z_j l_{Dj}^{-2} k^{-2}\left[-1+2(\omega/\Omega_j)\exp(-\omega^2/\Omega_j^2)\int_0^{\omega/\Omega_j}\exp y^2 dy + i\pi^{\frac{1}{2}}(\omega/\Omega_j)\exp(-\omega^2/\Omega_j^2)\right] \tag{35}$$

where

$$l_{Dj} = (KT_j\epsilon_0/N_j e^2)^{\frac{1}{2}} \tag{36}$$

is the Debye length for the jth particle.

Combination of (16), (17), (25), and (35) yields for the scattering cross section

$$\sigma_\omega = \left|\frac{1-\sum_{j=2}^{n} Z_j\xi_j}{1-\sum_{j=1}^{n} Z_j\xi_j}\right|^2 \pi^{-\frac{1}{2}}\Omega_1^{-1}N_1\sigma_e\exp(-\omega^2/\Omega_1^2) + \left|\frac{\xi_1}{1-\sum_{j=1}^{n} Z_j\xi_j}\right|^2 \sum_{j=2}^{n}\pi^{-\frac{1}{2}}\Omega_j^{-1}N_j\sigma_e\exp(-\omega^2/\Omega_j^2). \tag{37}$$

In the absence of the magnetic field, equation (37) is the formal solution to the problem. The quantity σ_ω represents the power scattered per unit incident power density, unit solid angle, unit scattering volume, and unit width of angular frequency.

Examination of equation (37) shows that the first term on the right represents a relatively wide spectral distribution of scattered power; the scattered power contained in the succeeding terms is spread over a much narrower range of frequencies. It is convenient to refer to the first term in equation (37) as the electronic term and to the succeeding terms as the ionic terms. This terminology will also be used for the terms of equation (25) and will be more fully justified in Section 8.

In the special case $n = 2$, $Z_1 = -1$, $Z_2 = 1$, $T_1 = T_2$ equation (37) agrees with the corresponding equations of Dougherty and Farley (1960). Similarly Salpeter's (1960) and Fejer's (1960) results can also be derived from equations (35) and (37).

Since certain special cases of this equation have already been discussed in some detail in the above papers the discussion here will be restricted to some additional computed results shown by Figs. 1–3.

Figure 1 refers to the case of $n = 2$, $Z_1 = -1$, $Z_2 = 1$, $T_1 = T_2$, $m_1 \ll m_2$. The curves on the right are identical with the curves of Salpeter's (1960*b*) Fig. 2. They represent $\sigma_\omega\Omega_1/N$ as a function of ω/Ω_1 for different values of the parameter $\alpha = (kl_D)^{-1}$ for large values of ω. The curves on the left represent

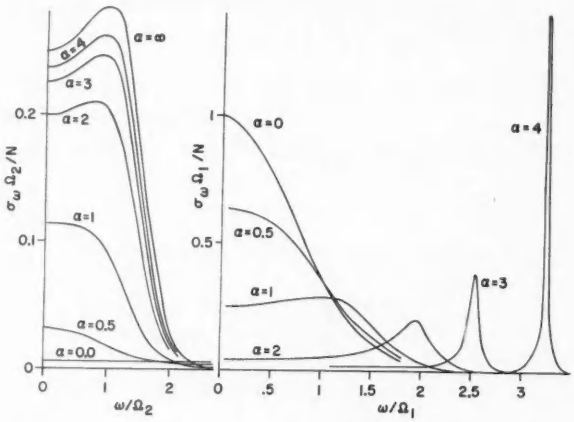

FIG. 1. The frequency spectrum for different values of the parameter $\alpha = k^{-1}l_D^{-1}$. The positive ions are assumed to be atomic oxygen. The ion and electron temperatures are assumed equal.

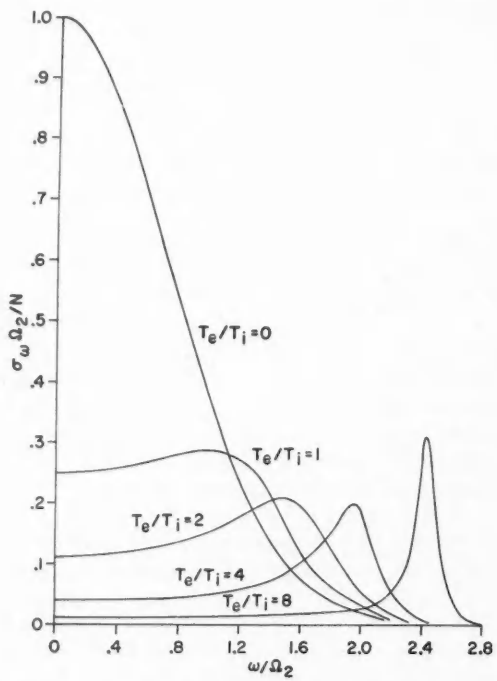

FIG. 2. The frequency spectrum for very large values of the parameter $\alpha = k^{-1}l_D^{-1}$ and for different ratios T_e/T_i of the electron temperature to the ion temperature.

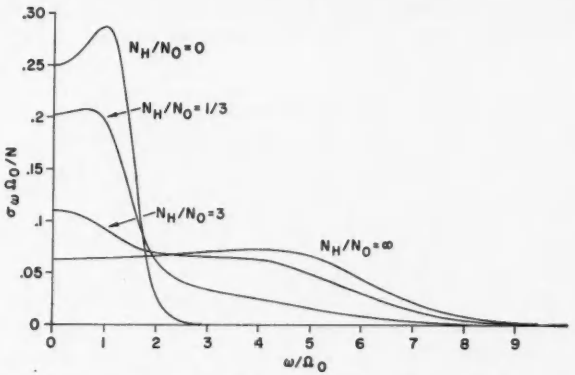

FIG. 3. The frequency spectrum for a plasma containing both atomic oxygen and hydrogen ions for different values of the ratio of their number densities N_O and N_H, for large values of the parameter α.

$\sigma_\omega\Omega_2/N$ as a function of ω/Ω_2 and thus represent the same curves drawn on a different scale for a different frequency range in order to show the behavior for small values of ω.

These two sets of curves of Fig. 1, show that for small values of the parameter α the spectrum function is very broad (the electronic part of the spectrum predominates) and of Gaussian shape; for large values of α the spectrum becomes narrow (the ionic part of the spectrum predominates) with the exception of a small amount of power scattered at frequencies differing from the frequency of the incident wave by the plasma frequency.

Figure 2 shows the spectrum functions $\sigma_\omega\Omega_2/N$ of a two-component plasma for $\alpha \gg 1$ for different ratios $T_1/T_2 = T_e/T_1$ of the electron and ion temperatures as a function of ω/Ω_2. It is seen that for low values of this ratio a Gaussian but narrow spectrum is obtained as predicted by Bowles (1959). The curve for $T_1 = T_2$ has been discussed previously. For large values of T_1/T_2 the total scattered power is greatly reduced and the spectrum has two sharp peaks which correspond to scattering by acoustic waves in the plasma involving the movement of both ions and electrons (Greene 1959). The Landau damping of these acoustic waves is low when the electron temperature is much greater than the ion temperature.

The curves of Fig. 2 show that given a knowledge of the ionic mass, the shape of the spectrum function not only gives an indication of the electron temperature, but also of its ratio to the temperature of the positive ions. For example, observations by Pineo *et al.* (1960), interpreted with the aid of the present theory, tend to show that the temperature of electrons is approximately equal to the temperature of positive ions in the F region and immediately above it.

Figure 3 is drawn for a three-component plasma consisting of electrons and positive atomic oxygen and hydrogen ions for $\alpha \gg 1$, $T_1 = T_2 = T_3$ for different values of the number density ratio $N_3/N_2 = N_H/N_O$ of hydrogen

to oxygen ions. Figure 3 thus shows the transition from a narrow spectrum corresponding to oxygen ions to a somewhat broader spectrum corresponding to hydrogen ions.

6. FREQUENCY SPECTRUM OF SCATTERED POWER FOR RANDOMLY DISTRIBUTED ELECTRONS IN A UNIFORM MAGNETIC FIELD IN THE ABSENCE OF COLLISIONS

The calculation carried out here uses a technique similar to that employed by Fejer (1960) in the calculation of the frequency spectrum for randomly distributed electrons with a high electron-neutral collision frequency.

The distribution of displacements l_t after time t in a direction parallel to the wave number vector $\mathbf{k} = \mathbf{k}_s - \mathbf{k}_0$ must be determined first. A new Cartesian co-ordinate system is introduced for this purpose with the z axis in the direction of the magnetic field and the $\mathbf{k}$ vector in the x,z plane. Consider the motion of an electron which, starting from the origin, reaches the point x_t, y_t, z_t after time t. The distance $R_t = (x_t^2+y_t^2)^{\frac{1}{2}}$, calculated from the equations of motion is then

$$R_t = (w/\Omega_H)[2(1-\cos \Omega_H t)]^{\frac{1}{2}} \tag{38}$$

where Ω_H is the electron gyro-frequency (the suffix 1 for electrons is dropped in this section) and w is the magnitude of the initial velocity component perpendicular to the magnetic field. The distance z_t travelled in the z direction in time t is given by

$$z_t = ut \tag{39}$$

where u is the velocity component in the z direction.

The Maxwellian velocity distribution, written in terms of the velocity components u and w, is given by

$$df = (m/2\pi KT)^{3/2} \exp[-(m/2KT)(u^2+w^2)]2\pi w dw du \tag{40}$$

or rewritten with the aid of equations (38) and (39) in terms of x_t, y_t, z_t

$$df = \left(\frac{m}{2\pi KT}\right)^{3/2} \frac{\Omega_H^2}{2(1-\cos \Omega_H t)} \exp\left\{-\frac{m}{2KT}\left[\frac{z_t^2}{t^2}+\frac{\Omega_H^2(x_t^2+y_t^2)}{2(1-\cos \Omega_H t)}\right]\right\} dx_t dy_t dz_t. \tag{41}$$

Let the unit vector in the direction of $\mathbf{k}$ have the Cartesian components $\sin\theta$, 0, $\cos\theta$. Then the distance l_t in the direction $\mathbf{k}$ is given by

$$l_t = x_t \sin\theta + z_t \cos\theta. \tag{42}$$

The distribution may now be expressed in terms of x_t, y_t, and l_t:

$$df = \left(\frac{m}{2\pi KT}\right)^{3/2} \frac{\Omega_H^2}{2(1-\cos \Omega_H t)\cos\theta} \exp\left\{-\frac{m}{2KT}\left[\left(\frac{l_t - x_t \sin\theta}{t\cos\theta}\right)^2 + \frac{\Omega_H^2(x_t^2+y_t^2)}{2(1-\cos \Omega_H t)}\right]\right\} dx_t dy_t dl_t. \tag{43}$$

The distribution in terms of l_t alone is obtained by carrying out the integrations in x_t and y_t. The result, without the normalizing factor, is

$$df \propto \exp\left[-\frac{m}{2KT}\frac{l_t^2}{t^2\cos^2\theta+2\Omega_H^{-2}(1-\cos\Omega_H t)\sin^2\theta}\right]dl_t. \tag{44}$$

It is assumed with Fejer (1960) that the particles moved with hypothetical velocities v such that $vt = l_t$ and it is further assumed that Doppler shifts $\omega_s-\omega_0 = \omega = kv$ result from these velocities so that the frequency spectrum of the scattered waves is proportional to

$$\exp\left[-\frac{m}{2KT}\frac{(\omega_s-\omega_0)^2t^2/k^2}{t^2\cos^2\theta+2\Omega_H^{-2}(1-\cos\Omega_H t)\sin^2\theta}\right]. \tag{45}$$

The Fourier transform of this hypothetical spectrum gives a hypothetical autocorrelation function

$$\rho_1(\tau) = \exp\left\{-i\omega_0\tau-\tau^2\frac{KTk^2}{2mt^2}[t^2\cos^2\theta+2\Omega_H^{-2}(1-\cos\Omega_H t)\sin^2\theta]\right\}. \tag{46}$$

The value of $\rho_1(\tau)$ is applicable to the actual problem only for $\tau = t$

$$\rho(t) = \exp\{-i\omega_0 t-\tfrac{1}{4}\Omega^2[t^2\cos^2\theta+2\Omega_H^{-2}(1-\cos\Omega_H t)\sin^2\theta]\} \tag{47}$$

where Ω is defined by equation (34). Then in terms of the Wiener–Kintchine theorem (Wiener 1930) the relative power spectrum $Q(\omega_s)$ is given by

$$Q(\omega_s) = (2\pi)^{-1}\int_{-\infty}^{\infty}\rho(t)\exp(i\omega_s t)\,dt$$

where

$$\int_{-\infty}^{\infty}Q(\omega_s)d\omega_s = 1.$$

The quantity σ_ω is then obtained in terms of equation (3) from $\sigma_\omega = Q(\omega_s)N\sigma_e$ where N is the electron number density. Thus

$$\sigma_\omega = (N\sigma_e/2\pi)\int_{-\infty}^{\infty}\exp\{i\omega t-\tfrac{1}{4}\Omega^2[t^2\cos^2\theta+2\Omega_H^{-2}(1-\cos\Omega_H t)\sin^2\theta]\}\,dt. \tag{48}$$

Comparison of this expression for the power spectrum σ_ω with equation (16) yields for the mean square space–time Fourier component $\overline{|s_\tau|^2}$ of randomly distributed electrons with a Maxwellian velocity distribution

$$\overline{|s_\tau(\omega,\mathbf{k})|^2} = (2\pi)^{-8}Vt_0N\int_{-\infty}^{\infty}\exp\{i\omega t-\tfrac{1}{4}\Omega^2[t^2\cos^2\theta+2\Omega_H^{-2}(1-\cos\Omega_H t)\sin^2\theta]\}\,dt. \tag{49}$$

This is one of the quantities which have to be determined before equations (16) and (25) are applied. Equation (49) may be rewritten to give $\overline{|s_{\tau j}|^2}$ for any particle j by attaching the suffix j to N, Ω, and Ω_H on the right.

It may be convenient sometimes to expand the factor $\exp(\frac{1}{2}\Omega^2\Omega_H^{-2}\sin^2\theta\cos\Omega_H t)$ in the integrand of (49) with the aid of the identity (Watson 1948)

$$\exp(x\cos\alpha) = I_0(x)+2I_1(x)\cos\alpha+2I_2(x)\cos 2\alpha+\ldots. \tag{50}$$

where $I_p(x)$ is the modified Bessel function of order p. The integration indicated in (49) can then be carried out, leading to

$$\overline{|s_r(\omega,\mathbf{k})|^2} = (2\pi)^{-7}\frac{Vt_0N}{\pi^{1/2}\Omega\cos\theta}\exp\left(-\frac{\Omega^2}{2\Omega_H^2}\right)\sum_{p=-\infty}^{\infty} I_p\left(\frac{\Omega^2\sin^2\theta}{2\Omega_H^2}\right)\exp\left[-\frac{(\omega+p\Omega_H)^2}{\Omega^2\cos^2\theta}\right]. \tag{51}$$

The spectrum σ_ω or the corresponding quantity $\overline{|s_r(\omega,\mathbf{k})|^2}$ may then be regarded as the sum of a number of Gaussian functions of ω, each centered on one of the harmonics (positive or negative) of the gyro-frequency of the particle. These Gaussian functions degenerate into δ functions when the wave number vector is perpendicular to the magnetic field.

An equivalent result has also been obtained by Laaspere (1960), who used a different method of calculation.

It follows from equation (49) that for $\Omega\cos\theta/\Omega_H \gg 1$ the integrand vanishes for large values of $\Omega_H t$. For small values of $\Omega_H t$ one may replace $1-\cos\Omega_H t$ by $\frac{1}{2}\Omega_H^2 t^2$ and therefore the effect of the magnetic field can be neglected if $\Omega\cos\theta/\Omega_H \gg 1$.

7. CALCULATION OF THE FACTORS ξ_j IN THE PRESENCE OF THE MAGNETIC FIELD

In the previous section the quantities $|s_{rj}|^2$ have been determined in the presence of the magnetic field. They represent the mean square space–time Fourier components which would exist in the absence of Coulomb interactions. Before equations (16) and (25) can be applied to the calculation of the spectrum, the factors ξ_j defined by equation (21) have to be determined. These factors have already been calculated in Section 5 for the field-free case from Liouville's equation. The present extension of the calculation closely follows Bernstein's (1958) analysis. In the presence of the magnetic field of induction $\mathbf{B}$ an additional force term $(Ze/m)(\mathbf{v}\times\mathbf{B})$ has to be included in Liouville's equation which takes the form

$$\partial W'/\partial t+\mathbf{v}.\mathrm{grad}_r W'+(Ze/m)(\mathbf{E}+\mathbf{v}\times\mathbf{B}).\mathrm{grad}_v W' = 0 \tag{52}$$

where the subscripts j are again omitted. Substitution of expression (28) for W' yields for the perturbation W after linearization

$$i\omega W-i(\mathbf{k}.\mathbf{v})W+(Ze/m)(\mathbf{v}\times\mathbf{B}_0).\mathrm{grad}_v W-(Ze/KT)(\mathbf{E}.\mathbf{v}) = 0 \tag{53}$$

where $\mathbf{B}_0$ is the induction of the uniform dominating magnetic field. Since the electric field $\mathbf{E}$ is taken to be the Coulomb field, it must be parallel to the vector $\mathbf{k}$, which points in the direction of the wave normal of the appropriate electron density waves. The electric field vector may therefore be expressed as $\mathbf{E} = E\mathbf{k}/k$ where $\mathbf{k}/k$ has the components $\sin\theta, 0, \cos\theta$. After introduction of the cylindrical velocity co-ordinates w, ϕ, u equation (53) may be written in the form

$$(54)\quad \partial W/\partial\phi+\Omega_H^{-1}[-i\omega+ik(w\sin\theta\cos\phi+u\cos\theta)]W$$
$$+(E/B_0)(m/KT)(w\sin\theta\cos\phi+u\cos\theta)=0$$

where $\Omega_H = ZeB_0/m$. If ω is again assumed to have a small negative imaginary part, the required solution of this first-order linear differential equation, which must be periodic in ϕ with a period of 2π, is

$$(55)\quad W=-(me/KTB_0)\exp\{\Omega_H^{-1}[(i\omega-iku\cos\theta)\phi-ikw\sin\theta\sin\phi]\}$$
$$\int_{\pm\infty}^{\phi}(w\sin\theta\cos\phi'+u\cos\theta)\exp\{\Omega_H^{-1}[(-i\omega+iku\cos\theta)\phi'+ikw\sin\theta\sin\phi']\}d\phi'.$$

The sign of the lower limit of the integral is taken to be the same as the sign of the charge. After introduction of the new variable $\beta = (\phi'-\phi)/2$ in the place of ϕ' and of the notation $\beta+\phi=\alpha$ equation (55) may be rewritten in the form

$$(56)\quad W=(2mE/KTB_0)\int_{\beta=0}^{\pm\infty}[w\sin\theta(\cos\alpha\cos\beta-\sin\alpha\sin\beta)+u\cos\theta]$$
$$\exp\{\Omega_H^{-1}[(-i\omega+iku\cos\theta)2\beta+2ikw\sin\theta\cos\alpha\sin\beta]\}\,d\beta$$

where the sign of the upper limit is taken to be the same as the sign of the charge.

In this form the periodicity of the solution (55) for W is clearly seen. In view of the discussion following equation (31)

$$(57)\quad s_t=N(m/2\pi KT)^{3/2}\int_0^{\infty}wdw\int_{-\infty}^{\infty}du\int_0^{2\pi}W\exp[-m(u^2+w^2)/2KT]d\phi$$

where W is given by equation (56). The expression on the right of equation (57) is then an integral in the four variables w, u, ϕ, β. It is convenient to start with the integration over ϕ and to change from ϕ to the new variable $\alpha=\phi+\beta$ already introduced in equation (56), with a corresponding change in the limits of integration. Further in terms of equations (21) and (29) one can write

$$(58)\qquad \xi = ies_t/k\epsilon_0E$$

and combination of this equation with equation (57) results in

$$(59)\quad \xi=(2ieN/k\epsilon_0B_0)(m/KT)(m/2\pi KT)^{3/2}\int_0^{\pm\infty}d\beta\int_0^{\infty}wdw\int_{-\infty}^{\infty}du$$
$$\exp[-m(u^2+w^2)/2KT+2\beta\Omega_H^{-1}(-i\omega+iku\cos\theta)]\int_{\beta}^{\beta+\pi}(w\sin\theta\cos\beta\cos\alpha$$
$$+u\cos\theta)\exp(2i\Omega_H^{-1}kw\sin\theta\sin\beta\cos\alpha)\,d\alpha.$$

The integrations over u are elementary. The integrations over α are readily carried out, using (Watson 1948)

$$(60)\qquad J_p(x)=(2\pi)^{-1}(-i)^p\int_0^{2\pi}\exp(ix\cos\varphi)\cos(p\varphi)\,d\varphi.$$

The result is

$$(61)\quad \xi = (ieN/k\epsilon_0 B_0)(m/KT)^2 \int_0^{\pm\infty} d\beta \int_0^{\infty} w \exp(-mw^2/2KT - 2i\beta\omega/\Omega_H$$
$$-2KT\beta^2 k^2 \cos^2\theta/m\Omega_H^2)[2iw \sin\theta \cos\beta J_1(2kw \sin\theta \sin\beta/\Omega_H)$$
$$+4i\Omega_H^{-1}\beta k \cos^2\theta(KT/m) J_0(2kw \sin\theta \sin\beta/\Omega_H)]\, dw.$$

The integration over w may be carried out, using (Watson 1948)

$$(62)\quad \int_0^{\infty} w^{r+1} J_r(aw) \exp(-w^2p^2) dw = a^r(2p^2)^{-r-1} \exp(-a^2/4p^2).$$

The result is, using the notation of equations (34)–(36) without the subscript j

$$(63)\quad \xi = -Zl_D^{-2}k^{-2}(\Omega^2/\Omega_H^2) \int_0^{\pm\infty} (\sin^2\theta \sin 2\beta + 2\beta \cos^2\theta) \exp[-2i(\omega/\Omega_H)\beta$$
$$-(\Omega^2/\Omega_H^2)(\beta^2 \cos^2\theta + \sin^2\beta \sin^2\theta)]\, d\beta.$$

In equation (63) the factor before the exponential differs only by the term $2i\omega/\Omega_H$ from the derivative of the exponent with respect to β. This makes a further simplification of the integral possible. The resulting equation

$$(64)\quad 1 + k^2 l_D^2 \xi/Z = (2i\omega/\Omega_H) \int_0^{\pm\infty} \exp[-2i(\omega/\Omega_H)\beta - (\Omega^2/\Omega_H^2)(\beta^2 \cos^2\theta$$
$$+\sin^2\beta \sin^2\theta)]\, d\beta$$

and equation (49) or (51), rewritten with the subscript j, yield all the quantities required for the calculation of the spectrum function σ_ω from equations (16) and (25).

In the special case when $\mathbf{k}$ is parallel to the magnetic field, equation (64) for ξ may be shown to be equivalent to equation (35) for ξ_j in the absence of the magnetic field, by execution of the indicated integrations.

Equation (64) remains nearly equivalent to equation (35) as long as $\Omega \cos\theta/\Omega_H \gg 1$, because then $\sin\beta$ can be replaced by β in the integrand for small values of β. For large values of β the integrand is vanishingly small.

A sometimes more convenient form of equation (64) is obtained by the substitution $2\beta = \gamma$ and subsequent expansion of the factor $\exp(\frac{1}{2}\Omega^2\Omega_H^{-2} \sin^2\theta \cos\gamma)$ with the aid of equation (50). This results in

$$(65)\quad 1 + k^2 l_D^2 \xi/Z = (i\omega/\Omega_H) \exp(-\Omega^2/2\Omega_H^2) \int_0^{\pm\infty} \exp(-i\omega\Omega_H^{-1}\gamma - \tfrac{1}{4}\gamma^2\Omega^2\Omega_H^{-2} \cos^2\theta)$$
$$\sum_{n=-\infty}^{n=\infty} I_n(\Omega^2 \sin^2\theta/2\Omega_H^2) \cos(n\gamma) d\gamma.$$

The integrals occurring in equation (65) may be evaluated, using the identity

$$(66)\quad \int_0^{\infty} \exp(-iax - \tfrac{1}{4}b^2x^2)\, dx = b^{-1} \exp(-a^2/b^2)\left(\pi^{\frac{1}{2}} - 2i \int_0^{a/b} \exp y^2 dy\right).$$

The resulting expansion is given by

$$(67)\quad 1+k^2l_D^2\xi/Z = \frac{\omega}{\Omega\cos\theta}\exp\left(\frac{\Omega^2}{2\Omega_H^2}\right)\sum_{n=-\infty}^{\infty} I_n\left(\frac{\Omega^2\sin^2\theta}{2\Omega_H^2}\right)$$
$$\exp\left[-\frac{(\omega-n\Omega_H)^2}{\Omega^2\cos^2\theta}\right]\left[i\pi^{\frac{1}{2}}+2\int_0^{(\omega-n\Omega_H)/\Omega\cos\theta}\exp y^2dy\right].$$

If this expansion converges rapidly, it may be more useful for numerical calculations than equation (64) because tables for the functions $\int_0^x \exp y^2dy$ and $I_n(x)$ exist.

8. FREQUENCY SPECTRUM OF SCATTERED POWER FOR A COLLISION-FREE PLASMA IN A UNIFORM MAGNETIC FIELD

The frequency spectrum is formally given by equations (16), (25), (49) or (51), and (64) or (67) in the presence of a uniform magnetic field. It may be necessary in some cases to use these equations for the evaluation of the spectrum but more often certain simple approximations are sufficient.

Before a description of any particular approximation is presented, a justification of the terminology introduced in Section 5 for the terms of equation (25) is given. It is shown that the spectrum function σ_ω can often be separated into two terms, the electronic and ionic term, since the mass of an ion is very much greater than the mass of an electron. For simplicity consider an ionized gas with only a single type of singly charged positive ion. In that case ξ_2 may be sometimes replaced by its limiting value for high frequencies in the first term of equation (25) and similarly ξ_1 may be replaced by its limiting value for low frequencies in the second term. The justification for these approximations is the fact that $\overline{|s_{r1}|^2}$ usually represents a very much wider spectrum than $\overline{|s_{r2}|^2}$ and similarly the characteristic variation of ξ_1 occurs over a much wider range of frequencies than that of ξ_2.

It is clear from equation (67) that for finite values of $\cos\theta$ the right-hand side vanishes for $\omega \to 0$ and thus $\lim_{\omega\to 0}\xi_1 = k^{-2}l_D^{-2}$. It is similarly clear from equation (63) that $\lim_{\omega\to\infty}\xi_2 = 0$. The simplified form of equation (25) becomes

$$(68)\quad \overline{|s_1|^2} = \frac{\overline{|s_{r1}|^2}}{|1+\xi_1|^2}+\frac{\overline{|s_{r2}|^2}}{|1+k^2l_D^2-k^2l_D^2\xi_2|^2}$$

where the first term depends only on the electronic parameters and the second term only on the ionic parameters. Equation (68) shows therefore that within the limits of its validity the effect of the magnetic field on the electronic and ionic spectra may be considered separately.

The approximations of equation (68) break down when $\Omega_{H1} \gg \Omega_1$, $\Omega_{H2} \ll \Omega_2$ and at the same time $\cos\theta \ll \Omega_2/\Omega_1$ because then $\overline{|s_{r1}|^2}$ represents a narrower spectrum (width of order $\Omega_1\cos\theta$) than $\overline{|s_{r2}|^2}$ (width of order Ω_2). Details of this case will be discussed later.

Since both ξ_1 and ξ_2 are proportional to $k^{-2}l_D^{-2}$ the second term vanishes for $kl_D \gg 1$ and the first term vanishes for $kl_D \ll 1$ in equation (68). With these results in mind three particular approximations valid in different limiting cases will now be considered.

(a) Strong Magnetic Field ($\Omega_H \gg \Omega$)

If the magnetic field is sufficiently strong, so that $\Omega_H \gg \Omega$ for both ions and electrons, then equation (64) becomes equivalent to equation (35) on replacement of Ω_j in the latter equation by $\Omega \cos\theta$ since the factor $\exp(-\Omega^2\Omega_H^{-2}\sin^2\beta\sin^2\theta)$ can then be replaced by unity. Similarly equation (49) becomes equivalent to equation (19) on replacement of $\Omega_j = k(2KT/m)^{\frac{1}{2}}$ by $\Omega\cos\theta$ in the latter.

Thus, if $\Omega_H \gg \Omega$ (i.e., if the radius of gyration is much smaller than k^{-1}) then the effect of the magnetic field is a reduction in the width of the spectrum by a factor $\cos\theta$; the effect in this case only depends on the direction of the field. In the extreme case of $\cos\theta = 0$ (i.e., when $\mathbf{k}$ is perpendicular to the magnetic field) the spectrum consists of only a single line at the frequency of the incident wave. The total scattered power is not changed by the magnetic field.

In ionospheric applications the condition $\Omega_H \gg \Omega$ is sometimes satisfied by electrons but not by ions. In such a case the above approximation applies only to the electronic spectrum. If at the same time $kl_D \ll 1$, then the power in the electronic spectrum is negligibly small and the approximation is of no interest.

(b) Weak Magnetic Field (i.e., $\Omega_H \ll \Omega$*) and* $\mathbf{k}$ *Sufficiently Far from Perpendicularity to the Magnetic Field (i.e.,* $\cos\theta \gg \Omega_H/\Omega$*)*

It has already been shown in Sections 6 and 7 that, for $\cos\theta \gg \Omega_H/\Omega$ equations (49) and (64) for $|s_r|^2$ and ξ in the presence of the field are equivalent to equation (19) and (35). The magnetic field thus has no effect on the spectrum under these conditions.

If the condition $\cos\theta \gg \Omega_H/\Omega$ is fulfilled only for ions, then the present approximation applies only to the ionic part of the spectrum. If at the same time $kl_D \gg 1$, then the power in the ionic spectrum is vanishingly small and the approximation is of no interest.

(c) Weak Magnetic Field (i.e., $\Omega_H \ll \Omega$*) and* $\mathbf{k}$ *Nearly Perpendicular to the Magnetic Field (i.e.,* $\cos\theta \ll \Omega_H/\Omega$*)*

Laaspere (1960) has already discussed the case for $kl_D \gg 1$ and has shown that a line spectrum is obtained if $\theta = \pi/2$. The envelope of the line spectrum has the same shape as the spectrum in the absence of the magnetic field. The frequencies of the spectral lines differ by exact multiples of the electron gyro-frequency from the frequency of the incident wave. The spectral lines spread out if the value of $\cos\theta$ is increased from zero, and for values of θ not very far from $\pi/2$ the lines are smeared out altogether so that approximation (*b*) applies.

The purpose of the present subsection is to show that, if equation (68) is valid, a similar approximation exists for other values of kl_D. The spectral lines do not differ from the frequency of the incident wave by exact multiples of the electronic or ionic gyro-frequency, however, and there are two sets of lines instead of one. The separation between the lines is close to the electronic gyro-frequency in one of these sets, and to the ionic gyro-frequency in the

other set. The envelopes of the two sets of lines have the respective shapes of the electronic and ionic spectrum that are found in the absence of a magnetic field.

The approximation is derived here only for $kl_D \ll 1$, which is the solution of greatest interest in ionospheric applications. A more general approximation may be derived by the same techniques for arbitrary values of kl_D, for both the electronic and the ionic parts of the spectrum, but the additional algebra is of no particular interest.

For $kl_D \ll 1$ equation (68) may be replaced by

$$\overline{|s_1|^2} = \frac{\overline{|s_{r2}|^2}}{|1-k^2l_D^2\xi_2|^2}. \tag{69}$$

For sufficiently small values of $\cos\theta$ equation (67) is well approximated by

$$1+k^2l_D^2\xi_2 = \exp(-\Omega_2^2/2\Omega_{H2}^2)\sum_{n=-\infty}^{\infty} I_n(\Omega_2^2/2\Omega_{H2}^2)\left\{\frac{\omega^2}{\omega^2-n^2\Omega_{H2}^2} + i\pi^{\frac{1}{2}}(\omega/\Omega_2\cos\theta)\exp\left[-\frac{(\omega-n\Omega_{H2})^2}{\Omega_2^2\cos^2\theta}\right]\right\}. \tag{70}$$

If $\theta = \pi/2$, then the imaginary part of the right-hand side of equation (70) vanishes for $\omega \neq n\Omega_{H2}$. The expression on the right of (69) therefore has infinities for all those values ω_m of the frequency ω for which $M = \mathrm{Re}(1-k^2 l_D^2\xi_2) = 0$, where from equation (70)

$$M = 2-\exp(-\Omega_2^2/2\Omega_{H2}^2)\sum_{n=-\infty}^{\infty} I_n(\Omega_2^2/2\Omega_{H2}^2)\frac{\omega^2}{\omega^2-n^2\Omega_{H2}^2}. \tag{71}$$

If θ is very nearly but not quite equal to $\pi/2$, then in the vicinity of one of the roots ω_m of $M = 0$ one may write approximately

$$1-k^2l_D^2\xi_2 = P_m(\omega-\omega_m)+iQ_m \tag{72}$$

where $P_m = (\partial M/\partial\omega)_{\omega=\omega_m}$ and $Q_m = \mathrm{Im}(1-k^2l_D^2\xi_2)_{\omega=\omega_m}$. A comparison of (51) and (70) shows that

$$\overline{(|s_{r2}|^2)}_{\omega=\omega_m} = -2^{-7}\pi^{-8}Vt_0N\omega^{-1}Q_m \tag{73}$$

and therefore

$$\sigma_\omega = -\pi^{-1}N\sigma_e\omega^{-1}Q_m/|P_m(\omega-\omega_m)+iQ_m|^2 \tag{74}$$

from equations (16) and (69).

If σ_ω is integrated over the frequencies in the neighborhood of the spectral line at $\omega = \omega_m$, using equation (74), the result is

$$\int_{\omega_m-\Delta\omega}^{\omega_m+\Delta\omega}\sigma_\omega d\omega = N\sigma_e\omega^{-1}|P_m|^{-1}. \tag{75}$$

The roots ω_m of the equation $M = 0$, with M given by (71), have to be determined before the application of equation (75), which gives the scattered power contained in the spectral lines.

The summation indicated in equation (71) may be replaced by integration for those terms for which

$$|n\Omega_{H2}-\omega| \gg \Omega_{H2} \tag{76}$$

since $\Omega_{H2} \ll \Omega_2$. In such an integration it is not necessary to exclude those terms for which condition (76) is not fulfilled, since they in any case do not contribute to the integral.

The result M' of the integration does not account for all the terms on the right of (71). The summation of terms in the vicinity of ω may, however, be carried out separately and yields M'', so that $M = M'+M''$. It will be seen after carrying out the integration and summation that the result M' of the integration is a relatively slowly varying function of ω, while the result M'' of the summation is a far more rapidly varying function if $\Omega_{H2} \ll \Omega_2$. For this reason the full expression $M = M'+M''$ will have to be used only in the determination of the roots ω_m of $M = 0$, while in the calculation of the derivative $P_m = (\partial M/\partial\omega)_{\omega=\omega_m}$ it is sufficient to set $M = M''$.

The integration indicated above is carried out first. From equation (71)

$$M' = 2-\exp(-\Omega_2^2/2\Omega_{H2}^2)\int_{-\infty}^{\infty} I_n(\Omega_2^2/2\Omega_{H2}^2)\,\frac{\omega^2}{\omega^2-n^2\Omega_{H2}^2}\,dn. \tag{77}$$

For large values of the argument one may approximate the modified Bessel function (Watson 1948) by

$$I_n(z) \cong (2\pi z)^{-\frac{1}{2}}\exp(z-n^2/2z). \tag{78}$$

Substitution of (78) into (77) and integration leads to

$$M' = 2-2(\omega/\Omega_2)\exp(-\omega^2/\Omega_2^2)\int_0^{2\omega/\Omega_2}\exp y^2 dy \tag{79}$$

which is the required contribution from the integration procedure. It is convenient to introduce the notation $\omega_d = \omega-(m+\frac{1}{2})\Omega_{H2}$ for the summation over terms for which $n\Omega_{H2} \sim \omega$ where ω is taken to lie between $m\Omega_{H2}$ and $(m+1)\Omega_{H2}$. Then n may be replaced by m in all the factors under the summation sign in equation (71) with the exception of the factor $(\omega-n\Omega_{H2})^{-1} = [\omega_d+(m+n-\frac{1}{2})\Omega_{H2}]^{-1}$. Equation (71) then gives, using $m\Omega_{H2} \sim \omega$,

$$M'' = -\exp(-\Omega_2^2/2\Omega_{H2}^2)I_m(\Omega_2^2/2\Omega_{H2}^2)\sum_{n=-\infty}^{\infty}\frac{\omega}{\omega_d+(m+n-\frac{1}{2})\Omega_{H2}}. \tag{80}$$

Substitution of I_m from (78) and combination of the terms $n = m+p-1$ and $n = m-p$ leads to

$$M'' = -2\pi^{-\frac{1}{2}}(\Omega_{H2}/\Omega_2)\exp(-\omega^2/\Omega_2^2)\omega\omega_d\sum_{p=0}^{\infty}[\omega_d^2-(p+\tfrac{1}{2})^2\Omega_{H2}^2]^{-1}. \tag{81}$$

The summation indicated in (81) can be carried out by contour integration which yields the identity (Titchmarsh 1939)

$$\tan z = 2z\sum_{n=0}^{\infty}[(n+\tfrac{1}{2})^2\pi^2-z^2]^{-1}.$$

Equation (81) then takes the form

$$M'' = \pi^{\frac{1}{2}}(\omega/\Omega_2)\exp(-\omega^2/\Omega_2^2)\tan(\pi\omega_d/\Omega_{H2}). \tag{82}$$

The root $\omega_{dm} = \omega_m - (m+\frac{1}{2})\Omega_{H2}$ of the equation $M'+M'' = 0$ is then obtained from equations (82) and (79) as

$$\tan(\pi\omega_{dm}/\Omega_{H2}) = 2\pi^{-\frac{1}{2}}\left[-(\Omega_2/\omega)\exp(\omega^2/\Omega_2^2)+\int_0^{\omega/\Omega_2}\exp y^2 dy\right] \tag{83}$$

where the argument of the tangent is taken to lie between $-\pi/2$ and $\pi/2$. This equation gives the position of the spectral lines for $\theta = \pi/2$. (Similar equations for the position of both electronic and ionic spectral lines are easily derived for general values of kl_D.)

The quantity $P_m \cong (\partial M''/\partial\omega_d)_{\omega_d=\omega_{dm}}$ may now be evaluated from equations (82) and (83) with the result

$$P_m = \pi^{\frac{1}{2}}\Omega_{H2}^{-1}(\omega/\Omega_2)\exp(-\omega^2/\Omega_2^2)\left\{\pi^2+4\left[-(\Omega_2/\omega)\exp(\omega^2/\Omega_2^2)+\int_0^{\omega/\Omega_2}\exp y^2 dy\right]^2\right\}. \tag{84}$$

Substitution of (84) into (75) results in

$$\int_{\omega_m-\Delta\omega}^{\omega_m+\Delta\omega}\sigma_\omega d\omega = \pi^{-\frac{1}{2}}N\sigma_e(\Omega_{H2}/\Omega_2)\frac{\exp(-\omega^2/\Omega_2^2)}{4\left[1-(\omega/\Omega_2)\exp(-\omega^2/\Omega_2^2)\int_0^{\omega/\Omega_2}\exp y^2 dy\right]^2+\pi[(\omega/\Omega_2)\exp(-\omega^2/\Omega_2^2)]^2} \tag{85}$$

which proves the original contention that the envelope of the spectral lines has the same shape as the spectrum given by equation (51) of Fejer (1960), which is found in the absence of the magnetic field. Comparison with equation (37) of the present paper shows in addition that the total scattered power is unchanged, as expected.

The amount of spread in the spectral lines, as $\cos\theta$ is increased from zero, can also be determined. Equation (74) shows that at half power the spread $\Delta_m\omega$ is given by

$$\Delta_m\omega = 2|Q_m/P_m|. \tag{86}$$

For sufficiently small values of $\cos\theta$ equations (70) and (78) give

$$|Q_m| = \frac{\omega\Omega_{H2}}{\Omega_2^2\cos\theta}\exp[-(\omega^2/\Omega_2^2)-(\omega_{dm}+\tfrac{1}{2}\Omega_{H2})^2/\Omega_2^2\cos^2\theta] \tag{87}$$

and P_m is given by (84).

Although equations (84), (86), (87) give the spread in the spectral lines quite accurately for sufficiently small values of $\cos\theta$, they are insufficiently accurate in the region $\cos\theta \sim \Omega_{H2}/\Omega_2$ where the transition from a spiky to a smeared-out spectrum occurs.

The displacement of the spectral lines, for $kl_D \ll 1$, from the positions which they would occupy for $kl_D \gg 1$, is illustrated by Fig. 4 which shows $(\omega_{dm}+\Omega_{H2}/2)/\Omega_{H2}$ as a function of ω/Ω_2.

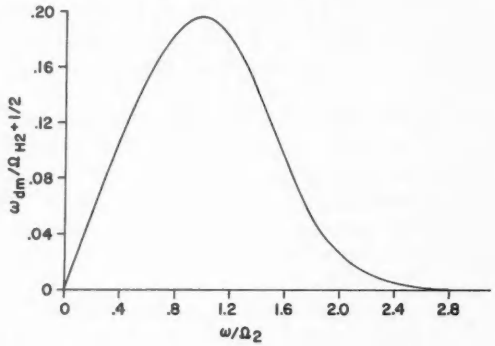

FIG. 4. The ratio of the displacement of spectral lines to the ion gyro-frequency as a function of ω/Ω_2 for $kl_D \ll 1$.

Three conditions were given for the validity of the approximation for the ionic spectrum discussed in the present subsection. These three conditions $kl_D \ll 1$, $\Omega_{H2} \ll \Omega_2$, and $\cos\theta \ll \Omega_{H2}/\Omega_2$ are sufficient if at the same time $\Omega_{H1} \ll \Omega_1$. If, however, this latter condition is not satisfied then the additional condition $\cos\theta \gg \Omega_2/\Omega_1 = (m_1/m_2)^{\frac{1}{2}}$ also has to be fulfilled because, as has been mentioned previously, equation (68) breaks down when $\Omega_{H1} \gg \Omega_1$, $\Omega_{H2} \ll \Omega_2$, and $\cos\theta \ll \Omega_2/\Omega_1$. There is usually an intermediate range of angles which satisfy the inequalities $\Omega_{H2}/\Omega_2 \gg \cos\theta \gg \Omega_2/\Omega_1$, and for which the approximation of the present subsection still applies even if $\Omega_{H1} \gg \Omega_1$.

The case $\Omega_{H1} \gg \Omega_1$, $\cos\theta \ll \Omega_2/\Omega_1$ is not very important in practice because it occurs only over a very narrow range of angles. For atomic oxygen ions θ would have to differ by less than one quarter of a degree from 90°. By considerations similar to those of the present subsection it may be shown that in this case practically no power is contained in those spikes for which $\omega \gg \Omega_1 \cos\theta$ and thus the spectrum, while it still consists of spikes separated approximately by the ion gyro-frequency, is narrower than the ionic spectrum in the absence of the magnetic field. For $\theta = \pi/2$ the spectrum consists of a single line at the frequency of the incident wave.

CONCLUSIONS

It has been shown, taking the magnetic field into account, that the spectrum function σ_ω can usually be divided into two parts, one of which is determined by the electrons, the other by the ions. The former dominates for $kl_D \gg 1$, the latter for $kl_D \ll 1$. This result makes a separate discussion of the electronic and ionic components of the spectrum possible. It has also been shown that the total power scattered is not affected by the magnetic field.

If $\Omega_H \gg \Omega$, for either electrons or ions then the magnetic field causes a contraction of the corresponding spectrum by a factor $\cos\theta$, where θ is the angle between $\mathbf{k}$ and the magnetic field.

If $\Omega_H \ll \Omega$ for either of the particles, and at the same time $\cos\theta \gg \Omega_H/\Omega$ then the magnetic field has practically no effect on the corresponding spectrum.

If $\Omega_H \ll \Omega$ for both ions and electrons but $\cos\theta \ll \Omega_H/\Omega$, then each spectrum has sharp maxima at frequencies separated approximately by the gyro-frequency of the corresponding particle. For $\theta = \pi/2$ these maxima become discreet spectral lines within the approximations of the present theory. The frequencies of these spectral lines differ by exact whole multiples of the gyro-frequency of electrons from the frequency of the incident wave, for $kl_D \gg 1$. For $kl_D \ll 1$ the spectral lines are displaced by amounts smaller than one-fifth of the ion gyro-frequency from positions which they would occupy if they differed by exact whole multiples of the ion gyro-frequency from the frequency of the incident wave. If one disregards the fine structure of the spectrum as manifested in these closely spaced maxima or discreet lines, then it is shown that the distribution of power in the spectrum, for $\Omega_H \ll \Omega$, is unchanged by the presence of the magnetic field.

If $kl_D \ll 1$, $\Omega_{H2} \ll \Omega_2$ but $\Omega_{H1} \gg \Omega_1$ then there is an intermediate range of angles, given by the condition $(\Omega_{H1}/\Omega_1)(\Omega_2/\Omega_1) \gg \cos\theta \gg \Omega_2/\Omega_1$, for which a spiky spectrum is again obtained in which, apart from the spiky structure, the distribution of power is still the same as in the absence of the magnetic field. For angles θ still nearer to $\pi/2$, however, the distribution of power in the spikes becomes progressively narrower. For $\theta = \pi/2$ all the scattered power is contained in a single line at the frequency of the incident wave.

In ionospheric experiments, at all frequencies likely to be used, the condition $\Omega_H \ll \Omega$ is satisfied for oxygen ions but not necessarily for hydrogen ions or electrons.

In experiments of Bowles (1958, 1959) and Pineo, Kraft, and Briscoe (1960), atomic oxygen ions were dominant and most of the energy was contained in the ionic part of the spectrum since $kl_D \ll 1$. Further, the inequality $\Omega_{H2}/\Omega_2 \cos\theta \ll 1$ was certainly satisfied by oxygen ions, and therefore the effect of the magnetic field on the spectrum was small.

In other experiments, however, the magnetic field could have an important effect on the spectrum as the following examples show.

For hydrogen ions, Ω_{H2} and Ω_2 may be of the same order of magnitude. If at the same time $kl_D \ll 1$ and $\mathbf{k}$ is nearly but not quite perpendicular to the magnetic field, then a large part of the scattered energy is contained in the two slightly broadened spectral lines whose frequency differs from the frequency of the incident wave approximately by the ion gyro-frequency. The existence of these spectral lines has been predicted by Bowles (1959).

Similarly, if the electron gyro-frequency Ω_{H1} is of the same order of magnitude as Ω_1, and at the same time $kl_D \gg 1$ and $\mathbf{k}$ is perpendicular to the magnetic field, then a large part of the scattered power is contained in those spectral lines whose frequency differs from the frequency of the incident wave by the electron gyro-frequency.

In both the above examples, the amount of scattered power contained in the spectral lines could be computed from the results of the present paper.

ACKNOWLEDGMENTS

The author is indebted to Mr. A. G. Heinicke who collaborated with him in the work described by Sections 3–6 of this paper, and to Miss S. Rousseau for assistance with the computations. The author would like to express his thanks to Dr. J. P. Dougherty for a stimulating exchange of ideas by correspondence. He would also like to acknowledge the benefit of discussions with Drs. V. R. Eshleman, J. Renau, T. Laaspere, C. O. Hines, and B. Segal. This work was performed under Project PCC No. D48-95-10-27.

REFERENCES

BERNSTEIN, I. B. 1958. Phys. Rev. **109**, 10.
BOWLES, K. L. 1958. Phys. Rev. Letters, **1**, 454.
——— 1959. Natl. Bur. Standards Rept. 6070.
DOUGHERTY, J. P. and FARLEY, D. T. 1960*a*. Proc. Roy. Soc. A, **259**, 79.
——— 1960*b*. Cavendish Laboratory, unpublished report.
FEJER, J. A. 1960. Can. J. Phys. **38**, 1114.
GORDON, W. E. 1958. Proc. I.R.E. **46**, 1824.
GREENE, J. M. 1959. Proc. Conference on Plasma Oscillations (privately circulated by Linde Co., Indianapolis).
HAGFORS, T. 1960. Scientific Report No. 1, Radioscience Laboratory, Stanford University.
KAHN, F. D. 1959. Astrophys. J. **129**, 205.
LAASPERE, T. 1960. J. Geophys. Research. To be published.
LANDAU, L. 1946. J. Phys. U.S.S.R. **10**, 25.
LORD RAYLEIGH. 1871. Phil. Mag. Ser. 4, **41**, 107.
PINEO, V. C., KRAFT, L. G., and BRISCOE, H. W. 1960. J. Geophys. Research, **65**, 2629.
RENAU, J. 1960. J. Geophys. Research, **65**, 3631.
SALPETER, E. E. 1960*a*. J. Geophys. Research, **65**, 1851.
——— 1960*b*. Phys. Rev. To be published.
TITCHMARSH, E. C. 1939. The theory of functions, 2nd ed. (Oxford University Press).
WATSON, G. N. 1948. Theory of Bessel functions (Cambridge University Press).
WIENER, N. 1930. Acta Math. **55**, 118.

EFFECT OF TWO-DIMENSIONAL MECHANICAL STRESS ON THE DIELECTRIC PROPERTIES OF POLED CERAMIC BARIUM TITANATE AND LEAD ZIRCONATE TITANATE[1]

R. F. Brown

ABSTRACT

Studies have been made of the dielectric behavior of several ferroelectric ceramic materials when a two-dimensional stress was applied normal to the axis of polarization. It has been shown that the dielectric constant decreases and the dielectric loss increases with increasing stress, part of the change being irreversible and part reversible. Upon application of stress to a sample, the dielectric constant did not change instantaneously but appeared to decrease linearly with the logarithm of time. Mechanisms are suggested for the observed effects.

INTRODUCTION

It is well known that the dielectric constant of barium titanate is dependent on the direction of measurement relative to the crystal axis. The dielectric constant of a pure barium titanate single crystal is about 300 in the direction of the spontaneous polarization (the *c*-axis) but about 4500 normal to the direction of polarization (the *a*-axis). Hence, in multidomain crystals, the dielectric constant is dependent upon the domain configuration and the orientation of the domains relative to the direction of measurement. If the direction of measurement is kept constant and the domain configuration is changed, the dielectric constant may be modified.

One method of altering the domain orientation is by the application of mechanical stress. Upon compression, the domains with the *c*-axis normal to the direction of stress have the lowest energy. Thus, the application of compressional stress to a multidomain crystal of barium titanate favors domains with a component of the *c*-axis normal to the applied stress. The dielectric constant normal to the direction of stress would be decreased while that in the direction of the stress would be increased.

Polycrystalline ferroelectric ceramics have a more complex structure than single crystals and the *c*-axes of the individual crystallites are randomly oriented, resulting in zero net polarization. However, a strong d-c. electric field tends to align the axes of spontaneous polarization of the domains in the direction of the external field, and the alignment remaining after removal of the field results in a remanent polarization in the ceramic. The application of stress to poled barium titanate ceramic would be expected to affect the dielectric constant, the magnitude and sign of the change being dependent upon the stresses and directions of application relative to the direction of polarization.

The effect of unidirectional stress on the dielectric properties of ceramic

[1]Manuscript received November 11, 1960.
Contribution from the Naval Research Establishment, Defence Research Board, Dartmouth, Nova Scotia.

barium titanate has been reported by a number of investigators in recent years (Takagi *et al.* 1948; Shirane and Sato 1951; Sinyakov and Izhak 1955; and Izhak 1956, 1957). In addition to unidirectional stress, the effects of two-dimensional stress have been studied by Roi (1955) and Ksendzov and Rotenberg (1959). The results presented in these papers show disagreement in the observed direction of change of the dielectric constant with stress, but this may be due in part to differences in the conditions of measurement such as the state of polarization of the samples, their history, and the time of measurement after the application of stress.

It has been observed by several investigators that the change in the dielectric constant of ceramic barium titanate which occurs after a change in stress is time dependent. Izhak (1957) showed that the application of a unidirectional compressional stress produced a rapid increase in dielectric constant followed by a gradual decrease to a steady value after several minutes.

This paper describes the effects of two-dimensional compressional stress on the low-field dielectric constant and dielectric loss of poled samples of two modified barium titanate compositions and two modified lead zirconate titanate compositions. Lead zirconate titanate has a crystal symmetry and domain structure similar to that of barium titanate and it would be expected that the effect of stress on the dielectric properties would be similar. It is found for both types of ceramic that, except for small values of stress, the dielectric constant in the direction normal to the stress decreases as the compression is increased. Most of this change is reversible, but there is usually a permanent drop in dielectric constant after the first pressure cycle on a fresh sample. Subsequent pressure cycles produce nearly reversible changes. The dielectric loss is found to increase as the stress is increased and falls to a value slightly higher than the initial value when the stress is released.

Quantitative measurements have been made of the aging process which is initiated by the stress, and it is shown that except for short times of less than about one minute, the dielectric constant usually decays substantially linearly with the logarithm of time, similar to the aging which follows poling of a ferroelectric ceramic. The aging rate is found to depend on the ceramic composition and the history of the sample.

STRESS SYSTEMS

A thin-wall sphere subjected to external hydrostatic pressure offers a simple means of obtaining high two-dimensional compressional stress in the wall for moderate external pressures. If a sphere of outside radius "b" and inside radius "a" is subjected to uniform external pressure P_0, the stress at any point at radius "r" in the wall of the sphere is fully described by three orthogonal stress components which are defined as the principal stresses. These are given by Love (1927):

(1) the tangential stresses

$$\sigma_\theta = \sigma_\phi = \frac{1}{2} P_0 \left(\frac{b}{r}\right)^3 \left[\frac{2r^3+a^3}{b^3-a^3}\right],$$

(2) the radial stress

$$\sigma_r = P_0\left(\frac{b}{r}\right)^3\left[\frac{r^3-a^3}{b^3-a^3}\right].$$

If the wall is thin relative to the radius, the radial component of stress can be neglected compared to the tangential components, which become

$$\sigma_\theta = \sigma_\phi \approx \frac{3}{2}P_0\left[\frac{b^3}{b^3-a^3}\right]$$

and the stress is essentially two-dimensional.

A thin-wall circular cylinder with ends closed by rigid caps and subjected to external hydrostatic pressure is also essentially a two-dimensional stress system. The two principal stress components are given approximately by Love (1927):

(1) the tangential stress

$$\sigma_\theta = 2P_0\left[\frac{b^2}{b^2-a^2}\right],$$

(2) the axial stress

$$\sigma_z = P_0\left[\frac{b^2}{b^2-a^2}\right] = \sigma_\theta/2.$$

Both the spherical and cylindrical samples of ceramic used in these experiments had silver electrodes on inner and outer surfaces and were poled radially. The capacity measured between electrodes was thus in a direction normal to the two principal stress components, and along the induced ferroelectric axis.

Although the stress tensors are different for spheres and end-capped cylinders exposed to external hydrostatic pressure, in both cases the important principal stresses are normal to the axis of polarization of the ceramic. If σ_1 and σ_2 represent the principal stresses in both two-dimensional systems, it has been found experimentally that the variation of dielectric constant as a function of the sum of the principal stresses, $\sigma_1+\sigma_2$, is approximately the same for spheres and cylinders of the same material. Most of the measurements reported here were made on cylindrical samples since these were more readily available than spherical samples.

DESCRIPTION OF CERAMIC SAMPLES

The hollow spheres were assembled by cementing together matched hemispherical shells of barium titanate or lead zirconate titanate ceramic with a nominal outside diameter of 3 in. and wall thickness of $\frac{1}{4}$ in. The shield of a coaxial cable was connected to the outer electrode of the sphere and the core was connected to the inner electrode via a small high pressure glass-to-metal seal cemented in the wall of the sphere. A thin waterproof coating was applied to the assembled sphere by dipping it in liquid neoprene.

The cylindrical test specimens (Fig. 1) consisted of ceramic cylinders of $1\frac{1}{2}$ in. nominal outside diameter, $1\frac{1}{2}$ in. length, and $\frac{1}{8}$ in. wall thickness, closed

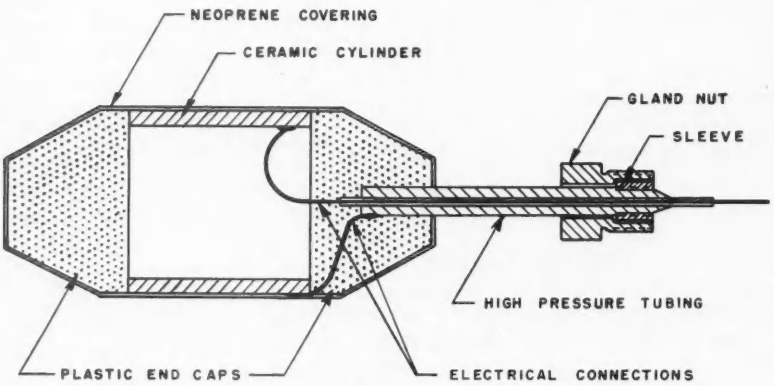

FIG. 1. Cross section of cylindrical ceramic specimen.

on the ends with rigid plastic caps. A length of high pressure steel tubing was moulded into one end cap to allow mounting of the specimen inside the high pressure tank with the electrical lead to the inner electrode running through the tube and that to the outer electrode connected to the tubing. The cylindrical samples were also given a thin waterproof covering of neoprene.

Four different ceramic compositions were investigated. The first was a common commercial material consisting of barium titanate with 4% by weight of lead titanate and 2% calcium titanate, which will be referred to as (Ba, Ca,Pb)TiO_3. The second was (Ba,Ca,Co)TiO_3, a composition described by Schofield and Brown (1957) consisting of barium titanate with additions of 5% by weight calcium titanate and $\frac{3}{4}$% cobalt carbonate. The lead zirconate titanate compositions were commercial PZT-4* and PZT-5*. All the samples were poled several months prior to these measurements, so that they were in a quasi-stable state and the changes due to stress application could be considered isolated from the changes due to normal aging of the ceramic.

EXPERIMENTAL METHOD

The pressure system consisted of a water-filled tank capable of 1000 kg/cm^2 hydrostatic pressure, monitored by a Bourdon gauge which had been calibrated against a dead-weight tester. Measurements of the capacity and dielectric loss of the samples were made with a General Radio Type 716C capacity bridge using a signal of about 1 volt across the samples at 1 kc/s. From the measured capacity and dimensions of the samples, the permittivity or dielectric constant was calculated. The stress in the wall of each sample was calculated from the measured dimensions of the sample and the known external pressure. Although no attempt was made at temperature control of the pressure vessel, the temperature remained in the region 21° to 23° C during the measurements, a range in which the dielectric constant of all four compositions is essentially temperature independent.

*PZT-4 and PZT-5 are registered trademarks of the Clevite Corporation.

Measurements of capacity and dielectric loss were made as a function of stress as the external pressure was increased in steps of 70 kg/cm² to a maximum of 490 kg/cm² and then reduced to zero in similar steps. The maximum pressure was limited to keep the stresses well within the estimated compressional strength of the materials. Because of the time dependence of permittivity after a change in stress, a standard time reference was established by taking the measurements 10 minutes after each change of pressure. The pressure was cycled at least four times in order to determine the permanent and reversible components of change in dielectric constant and the influence of each cycle on the following one. At the maximum pressure, the variation of capacity with time was recorded for a period of at least 2 hours on the first three pressure cycles, and for 2 or 3 days on the fourth cycle.

EXPERIMENTAL RESULTS

(a) Effects of Stress

The dielectric constant of cylindrical samples of each of the four ceramic materials is plotted against the sum of the principal stresses, $\sigma_T = \sigma_\theta + \sigma_z$ in Figs. 2 to 5 for the first two pressure cycles. With one exception, the dielectric constant on the third and fourth pressure cycles was only very slightly less than that on the second cycle, and is not shown in the figures. However, the fourth cycle is shown for PZT-4 because there was an appreciable change in dielectric constant. The drop in dielectric constant at the maximum pressure, which can be seen in the figures, occurred during the aging investigations which will be shown in detail later. After the release of pressure at the end of each cycle, there was an 18-hour interval before the start of the next pressure cycle during which time the dielectric constant of PZT-5 increased slightly while that of the other three compositions decreased. This change amounted to about 6% for PZT-4 but was less than 1% for the other materials.

On the fourth cycle, the maximum pressure was held for 4 days while measurements of dielectric constant and loss were made on all samples at convenient time intervals. It will be seen from Fig. 4 that a relatively large change occurred in the dielectric constant of PZT-4 which was not recovered after the release of the pressure. The changes which occurred in the other materials during this time were much smaller, and during the decrease of pressure to zero the dielectric constant followed closely the curves of the first two cycles.

In order to compare the different compositions graphically, the dielectric constant measured on the increasing leg of the second pressure cycle has been normalized and plotted in Fig. 6 against the sum of the principal stresses in the samples.

The dielectric loss, which is also shown in Figs. 2 to 5, increased with increasing stress and returned to a value slightly higher than the initial value after the release of stress. Under constant stress, the dielectric loss decreased slightly with time. The dielectric loss on successive pressure cycles is not shown since there was little change from the first cycle.

Spherical samples were available in (Ba,Ca,Pb)TiO_3 and PZT-4 ceramic.

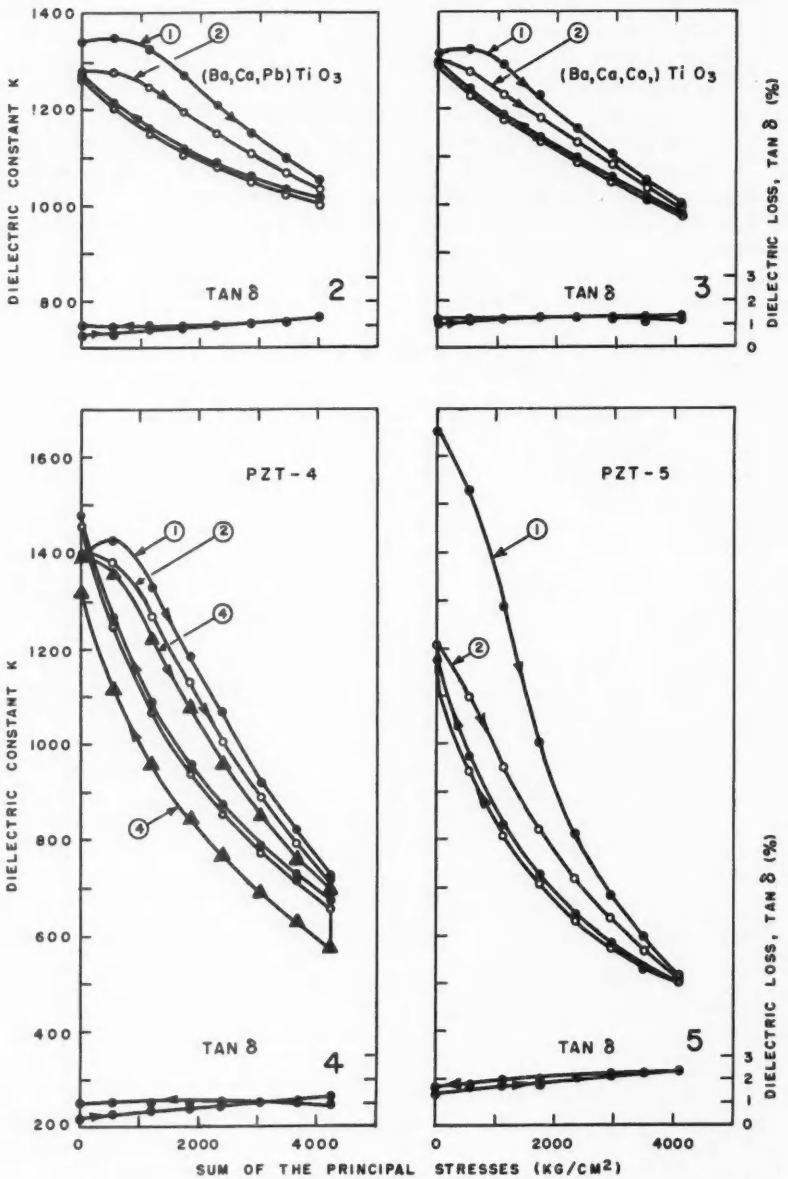

FIGS. 2–5. Effect of two-dimensional stress on the dielectric constant and dielectric loss of ceramic $BaTiO_3$ and PZT.

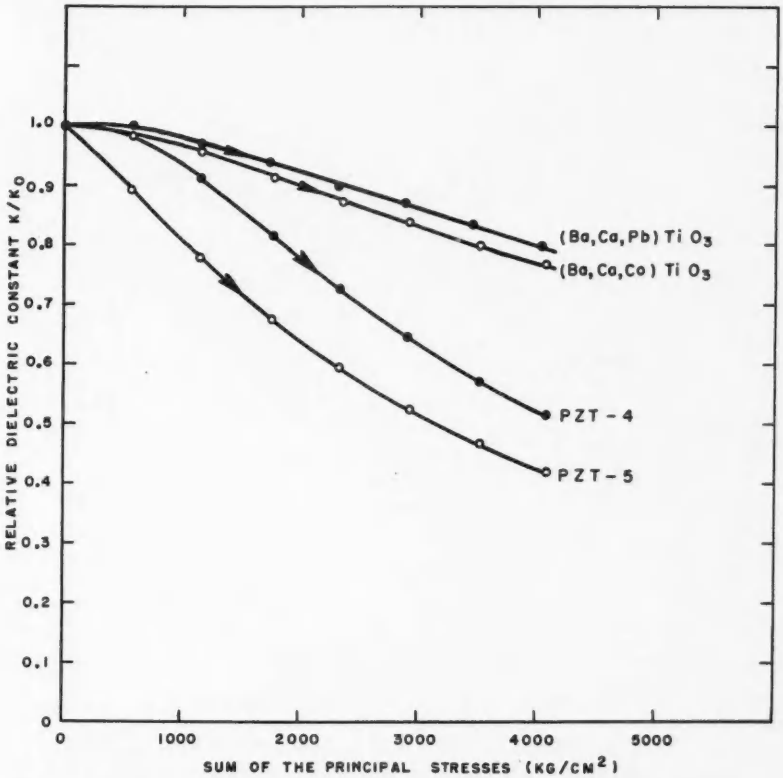

FIG. 6. Comparison of the change of dielectric constant with stress for different materials.

For these, the normalized dielectric constant measured on the second increasing pressure cycle is plotted in Figs. 7 and 8 against the sum of the principal stresses, $\sigma_T = \sigma_\theta + \sigma_\phi$. On the same graphs, the dielectric constant for cylindrical samples in the same cyclic condition is plotted against the sum of the principal stresses, $\sigma_T = \sigma_\theta + \sigma_z$. Even though the ratios of the principal stresses are $\sigma_\theta/\sigma_\phi = 1$ for the sphere and $\sigma_\theta/\sigma_z = 2$ for the cylinder, the curves coincide within 2%.

(b) Aging Phenomena

In these experiments it was found that the capacity did not reach a constant value within a few minutes after a change in stress, but continued to decrease over the period of measurement, which sometimes extended to several days. The dielectric constant of the four ceramic materials is plotted against the logarithm of time in Figs. 9 to 12. The data for these curves were obtained after the external pressure had been raised from 420 to 490 kg/cm² on each of

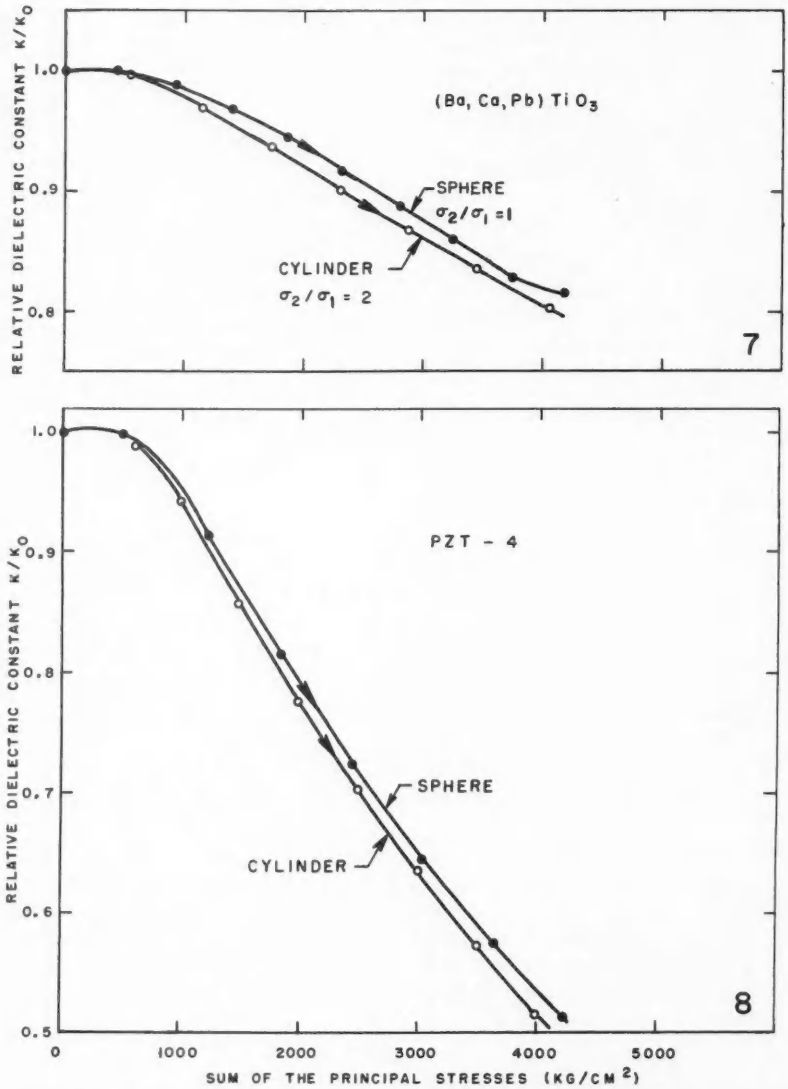

FIGS. 7–8. Variation of the dielectric constant with stress for different ratios of the principal stresses.

the four successive pressure cycles which have been described. It should be noted that the method of measurement did not allow observation of the dielectric behavior immediately after a change in stress, and consequently the

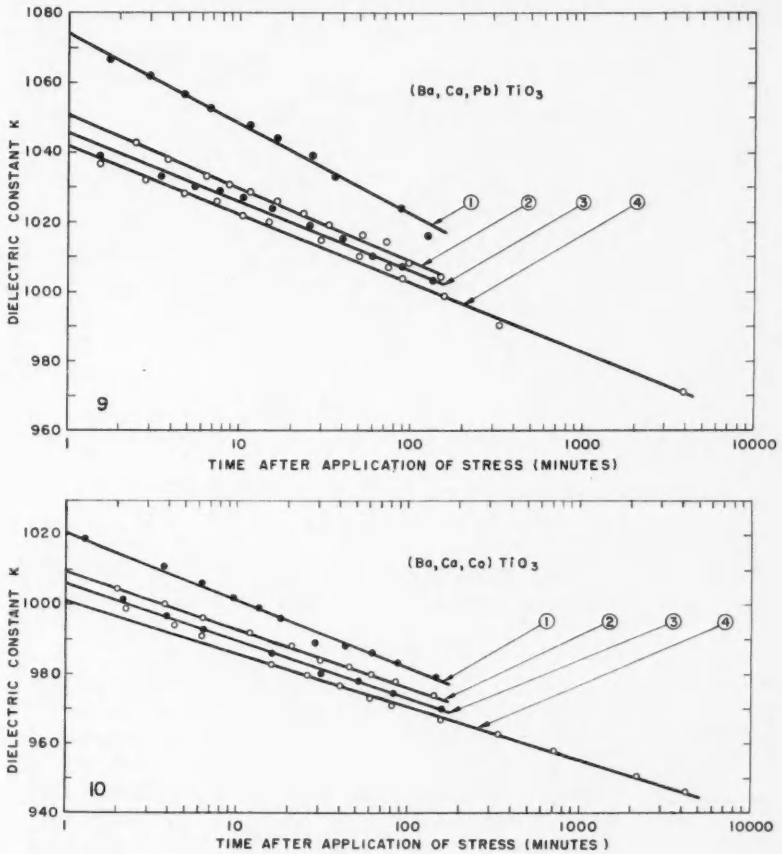

FIGS. 9–10.

initial increase in dielectric constant noted by Izhak (1957) could not be observed.

For comparison of the four materials, the dielectric constant measured on the fourth time run has been normalized, taking the 1-minute value as $K/K_0 = 1.00$, and the curves plotted together in Fig. 13. It is evident that the dielectric constant for three of the materials continues to fit a linear relationship with log t quite closely, but the slope of the curve for PZT-4 increases with time. The rates of decrease, expressed as the percentage change in the decade from 10 minutes to 100 minutes after application of pressure, are tabulated in Table I for the various cycles for each composition. It should be noted that the values listed for PZT-4 are average values for this decade, since the

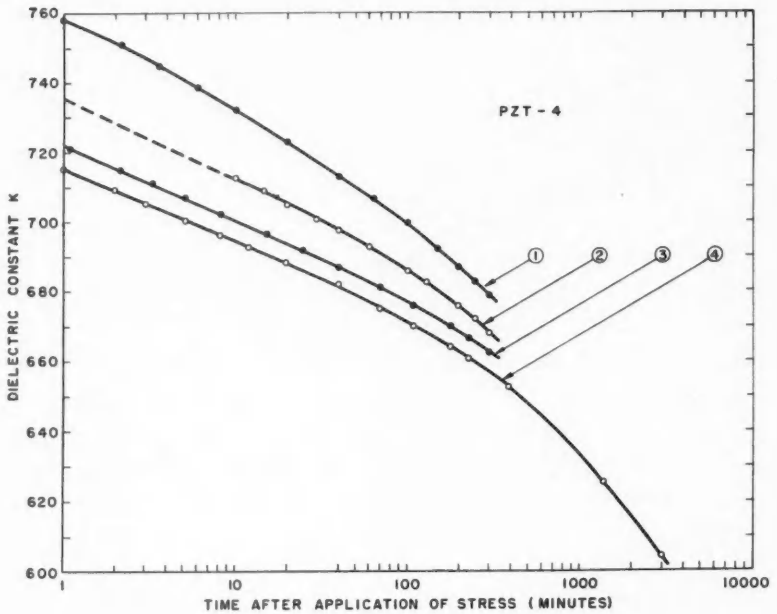

FIG. 11.

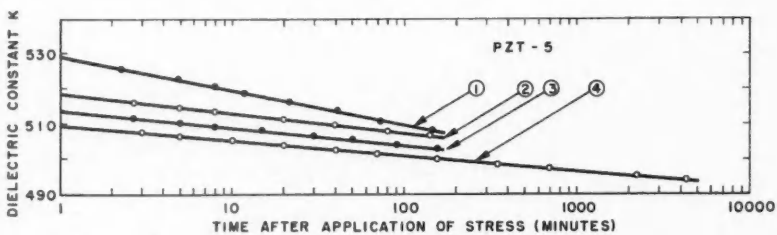

FIGS. 9–12. Aging of the dielectric constant after four successive applications of two-dimensional stress.

TABLE I

Rate of stress-induced aging

Ceramic material	Rate of change of dielectric constant (per cent per decade) for a change in external pressure from 420 to 490 kg/cm²			
	1st cycle	2nd cycle	3rd cycle	4th cycle
$(Ba,Ca,Pb)TiO_3$	2.5	2.0	2.0	2.0
$(Ba,Ca,Co)TiO_3$	1.9	1.7	1.7	1.6
PZT-4	4.4	3.8	3.4	3.4
PZT-5	1.9	1.1	1.0	0.9

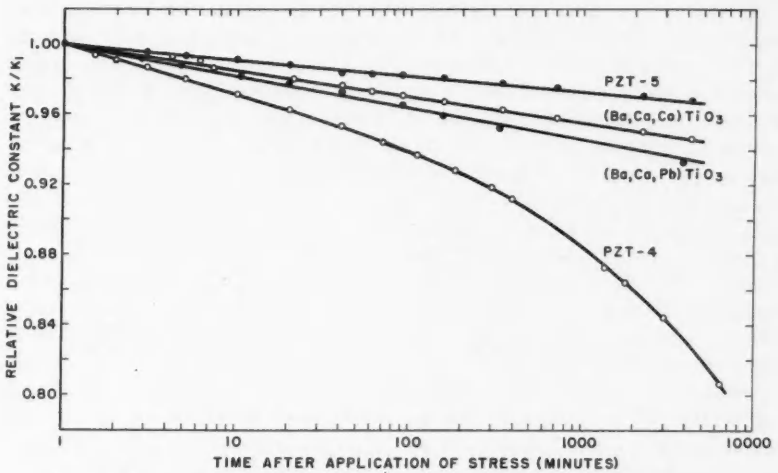

FIG. 13. Comparison of stress-induced aging for different materials.

decrease is not linear with log t. The fact that the rate of aging is higher on the first time run than on successive runs indicates a certain amount of stabilization in the ceramic after the first application of high stress.

DISCUSSION

(a) Effect of Stress

There are two components contributing to the observed dielectric constant or permittivity in a ferroelectric ceramic. One is the intrinsic permittivity of domains, and the other is a contribution to permittivity due to the oscillation of 90° domain walls as described, for example, by Plessner (1956).

The effect of stress on the intrinsic permittivity of a single domain may be predicted from the thermodynamic theory of ferroelectricity. This shows that the changes in permittivity which occur when stress is applied normal to the c-axis or normal to the a-axis are opposite in sign. In a ceramic, only a portion of domains are aligned with c-axes along the poling direction, so that domains may be compressed in either the a or c directions by the external pressure. The resultant changes in dielectric constant would have opposite signs and tend to cancel, so that only a small contribution to the total dielectric constant would be expected from changes in the intrinsic permittivity of individual domains.

Probably a more important effect is the fact that compressional stress tends to align domains so that their polar axes (c-axes) are normal to the direction of applied stress. Since the intrinsic permittivity in the c direction is much less than that in the a direction, this domain alignment should result in a reduction of the contribution to total dielectric constant from the intrinsic permittivity of domains.

However, it is also necessary to take account of the contribution from domain wall oscillation. In order to explain the experimentally observed increase in total dielectric constant which occurs for small compressional stresses in some of the ceramic compositions, it is postulated that the application of this stress facilitates the oscillation of domain walls in response to a small alternating voltage, that is, that it increases domain wall mobility. This would result in an increase in the contribution to permittivity due to domain wall oscillation.

The observed behavior can be explained by assuming that, as the stress is increased, greater wall mobility causes the dielectric constant to increase initially, but that domain alignment soon becomes the controlling factor resulting in a decrease in the dielectric constant. The relative magnitude of the two effects depends on the obstacles to domain wall motion and domain alignment and can therefore be expected to be composition dependent. The process of domain alignment would be expected to continue with increasing stress until all domains were aligned with *c*-axes normal to the stress. This would result in the dielectric constant decreasing to a limiting value, and there is some experimental evidence in Figs. 2 to 5 that the curves do tend to level out for sufficiently high stress.

The failure of the dielectric constant to return to the initial value after a pressure cycle indicates some permanent reorientation of domains. However, the greater part of the change is reversible, showing that domain reorientation is largely a reversible process. This is in agreement with strain measurements made by Subbarao, McQuarrie, and Buessem (1957), which showed little permanent domain reorientation after the release of a compressive stress.

The increase in dielectric loss with stress is explained by the assumption of higher domain wall mobility, since domain wall oscillation is inherently an energy-dissipating process. The fact that this loss gradually decreases with time when the stress is held constant indicates that the wall mobility becomes less with time as the walls assume positions of greater stability.

(b) Aging Phenomena

The aging of permittivity which occurs after a change in stress is similar to that initiated when ceramic samples are freshly poled, and thus seems likely to be due to a similar process. The aging which occurs after poling has been ascribed to the motion of domain boundaries to more stable positions. By analogy with ferromagnetism, McQuarrie and Buessem (1955) and Plessner (1956) have shown that, except for very short and very long times after poling, the aging process should follow a log t relationship if it is assumed that the obstacles to domain wall motion have a random character, resulting in a wide distribution of activation energies. However, the aging of some ceramic samples has been found to deviate from a linear relation with log t, sometimes increasing and sometimes decreasing in slope with time. Therefore it is not surprising that the stress-induced aging in PZT-4 is found to deviate from the simple log t relation, although the mechanisms are not well understood. A more detailed study of the pressure dependence of the aging rate is continuing and will be reported separately.

ACKNOWLEDGMENTS

The advice and encouragement of Dr. D. Schofield, who suggested this investigation, are gratefully acknowledged.

This work arose as part of an investigation under Defence Research Board Project D108-55-25-02 and is published by permission of the Board.

REFERENCES

IZHAK, I. A. 1956. Izvest. Akad. Nauk S.S.S.R. Ser. Fiz. **20**, 199.
——— 1957. Zhur. Tekh. Fiz. **27**, 953 (translated in Soviet Phys.-Tech. Phys. **2**, 872).
KSENDZOV, YA. M. and ROTENBERG, B. A. 1959. Fiz. Tver. Tela, **1**, 637 (translated in Soviet Phys.-Solid State, **1**, 579).
LOVE, A. E. H. 1927. A treatise on the mathematical theory of elasticity, 4th ed. (Dover Publications, New York).
MCQUARRIE, M. C. and BUESSEM, W. R. 1955. Am. Cer. Soc. Bull. **34**, 402.
PLESSNER, K. W. 1956. Proc. Phys. Soc. (London), B, **69**, 1261.
ROI, N. A. 1955. Soviet Phys.-Acoustics, **1**, 366.
SCHOFIELD, D. and BROWN, R. F. 1957. Can. J. Phys. **35**, 594.
SHIRANE, G. and SATO, K. 1951. J. Phys. Soc. Japan, **6**, 20.
SINYAKOV, E. V. and IZHAK, I. A. 1955. Doklady Akad. Nauk S.S.S.R. **100**, 243.
SUBBARAO, E. C., MCQUARRIE, M. C., and BUESSEM, W. R. 1957. J. Appl. Phys. **28**, 1194.
TAKAGI, Y., SAWAGUCHI, E., and AKIOKA, T. 1948. J. Phys. Soc. Japan, **3**, 270.

INVESTIGATIONS ON THE DIFFUSION OF MINORITY CARRIERS FROM A POINT ON SILICON[1]

C. H. CHAMPNESS[2]

ABSTRACT

The field-free diffusion of minority carriers injected at a point in silicon has been studied and the time from injection to the maximum of the collector signal due to the arriving carriers measured for various emitter–collector distances. Firstly, it was found that for 2-ohm-cm, 6-microsecond, *n*-type material the time to maximum was proportional approximately to the emitter–collector spacing raised to the power 1.2 for flat surfaces and to the power 1.6 for 3- and 6-degree wedge samples. The power 1.6 was also found for a 17-degree wedge of 120-ohm-cm, 100-microsecond, *p*-type silicon. Secondly, decay times following the maxima appeared to increase with emitter–collector spacing. No adequate two-surface theory is available but comparison with a one-surface theory revealed serious disagreements. It would appear that the results may be explained qualitatively by assuming that the effective lifetime is dependent on the excess carrier density and decreases as the emitter point is approached.

INTRODUCTION

Much of the early work on transistor action and on drift mobility studies was done using point contacts on the surface of a semiconductor. There appears, however, to have been no special experimental study of the concentration of carriers with distance and time as they diffuse out from a point contact with no applied electric field. No doubt this is because it was thought that the process of field-free diffusion is a straightforward one which could be accurately described by a radial solution of the diffusion equation with a simple recombination term. Such a solution assumes only small concentrations. However, actually the problem involves a high concentration of extra carriers near the point of origin. This could affect both the lifetime and the diffusivity. The present experiments were therefore carried out to test the validity of the conventional diffusion theory under the circumstance of very heavy localized injection at a point contact.

If minority carriers are injected at a point they will diffuse outwards radially and give rise to a collector current through a reversed biased collector point. This collector current is approximately proportional to the concentration of excess minority carriers near the point (Shockley, Pearson, and Haynes 1949). The collector current will increase with time as more carriers reach the point. However, for pulsed injection, as was used in the present experiments, it will reach a maximum and begin to decrease because of the decrease of carriers at the emitter. This is shown in Fig. 1B, which shows a typical oscilloscope trace obtained in the experiments. The asymmetry of the arrival pulse is to be compared with that in Fig. 1A, which shows a trace recorded in a drift mobility experiment where the carriers are transported under an applied

[1]Manuscript received November 29, 1960.
Contribution from the Solid State Physics Laboratory, Research and Development Division, Northern Electric Company Limited, Montreal, Que.
[2]Now at Physics Department, McGill University, Montreal, Canada.

PLATE I

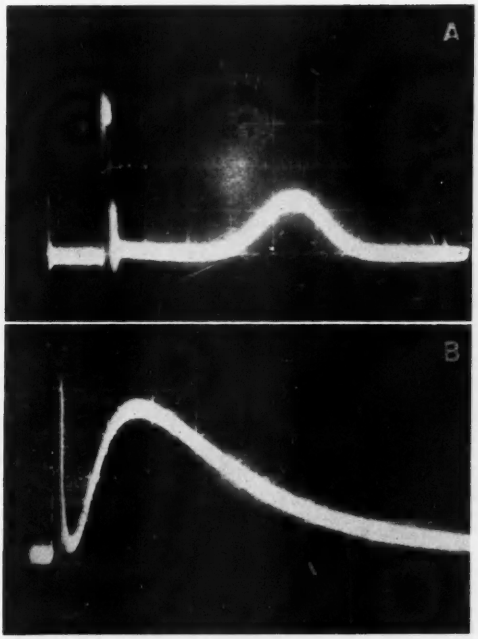

FIG. 1. Variation of collector signal with time. A shows an oscilloscope trace obtained during a drift mobility experiment. B shows the trace with the circuit of Fig. 3, i.e., no applied electric field.

electric field. In the experiments reported in this paper there was no applied electric field. The quantities measured were the time (t_m) from the center of the injection pulse to the maximum in the collector signal, the decay of the collector signal following the maximum, and the emitter–collector spacing (r).

THEORY OF DIFFUSION FROM AN INSTANTANEOUS POINT SOURCE

Before the details of the experimental work are presented, it is helpful to review theoretical results for the case of diffusion from an instantaneous point source firstly in an infinite and secondly in a semi-infinite medium.

Infinite Solid

Suppose N_p holes are injected in a very short interval of time at a point $r = 0$ inside an infinite n-type semiconductor. Suppose, too, that there are no applied electric fields and that there is no space charge anywhere. With Δp, the excess concentration of holes, equal to Δn, the excess concentration of electrons, there is a single lifetime τ for holes and electrons. The rate of change of Δp with time t is then given by

$$\frac{\partial \Delta p}{\partial t} = \text{div } (D' \text{ grad } \Delta p) - \frac{\Delta p}{\tau} \tag{1}$$

where D' is the ambipolar diffusivity $(n+p)[(n/D_p)+(p/D_n)]^{-1}$, D_n is the electron diffusivity, D_p the hole diffusivity, and n and p respectively are the electron and hole concentrations. If div grad is expressed in polar co-ordinates with radial dependence only, equation (1) may be solved with the boundary conditions $N_p = \int_0^\infty \Delta p . 4\pi r^2 dr$ as $t \to 0$, and $\Delta p \to 0$ as $r \to \infty$ to give the well-known (Shockley 1950) solution

$$\Delta p = N_p (4\pi D_p t)^{-3/2} \exp\left\{-\left(\frac{r^2}{4D_p t} + \frac{t}{\tau}\right)\right\}, \tag{2}$$

where D' has been replaced by D_p since $n \gg p$ is assumed.

This equation predicts qualitatively the approximate shape of the observed oscilloscope trace in Fig. 1B. At its maximum, equation (2) yields

$$\tau = 4D_p t_m^2 (r^2 - 6D_p t_m)^{-1}, \tag{3}$$

where t_m is the time at the maximum. If $\tau \gg \frac{2}{3} t_m$, equation (3) reduces to

$$t_m = r^2/6D_p \tag{4}$$

and if $\tau \ll \frac{2}{3} t_m$ we get

$$t_m = \frac{r}{2} (\tau/D_p)^{\frac{1}{2}}. \tag{5}$$

Thus in comparison with the time to maximum, if the lifetime is large, t_m depends quadratically on the emitter–collector spacing but if the lifetime is small a linear variation is expected. For lifetimes between the two extremes equation (3) gives

$$t_m = \frac{3}{4} \tau \left\{\left(1 + \frac{4r^2}{9D_p \tau}\right)^{\frac{1}{2}} - 1\right\}. \tag{6}$$

Semi-infinite Solid

The theory of diffusion in a semi-infinite solid has been worked out in great detail by van Roosbroeck (1955), taking surface recombination velocity (s) into account. Using his theory the following three cases may be considered: (A) emitter and collector on the surface, (B) emitter inside the solid and collector on the surface, and (C) emitter on the surface and collector inside the solid. At the maximum of Δp the following result holds for the three cases

$$\tau = 4D_p t_m^2\{r^2-6D_p t_m(1+\tfrac{2}{3}\epsilon)\}^{-1} \tag{7}$$

where ϵ is a number between 0 and 1 which can be evaluated specifically for extreme values of s. These are as follows:
(i) $s \ll (D_p/t_m)^{\frac{1}{2}}$, i.e. s small, $\epsilon = 0$ for all three cases and hence the results obtained for an infinite solid apply, since equation (7) reduces to equation (3).
(ii) $s \gg (D_p/t_m)^{\frac{1}{2}}$, i.e. s large, $\epsilon = 1$ for case (A) but for cases (B) and (C)

$$\epsilon = [1+(r/2st_m)]^{-1}. \tag{8}$$

(iii) $s \gg r/2t_m$, i.e. s still larger (since $r/2t_m \gtrsim (D_p/t_m)^{\frac{1}{2}}$), $\epsilon = 1$ for all three cases. Equation (7) then reduces to

$$\tau = 4D_p t_m^2(r^2-10D_p t_m)^{-1}. \tag{9}$$

Under condition (ii) for cases (B) and (C), equations (7) and (8) may be solved for s to get the following result

$$s = \frac{r}{2t_m}\frac{X\tau-1}{1-Y\tau} \tag{10}$$

where $X = (r^2-6D_p t_m)/4D_p t_m^2$ and $Y = (r^2-10D_p t_m)/4D_p t_m^2$. Since $X > Y$, we must have, for s to be a positive quantity, that

$$X^{-1} < \tau < Y^{-1}. \tag{11}$$

Using the above notation for X and Y we may rewrite equations (3) and (9) as simply

$$\tau = X^{-1}, \qquad s \to 0 \tag{3A}$$

$$\tau = Y^{-1}. \qquad s \to \infty \tag{9A}$$

EXPERIMENTAL METHOD

The experiments were mostly carried out using samples cut from a 2-ohm-cm doped n-type single crystal of silicon. Subsidiary measurements made on the material gave a lifetime of about 6 microseconds, a drift mobility for the holes of 230 cm^2/volt sec, and a donor concentration of about 10^{15}/cm^3. Experiments were also made on a sample of 120-ohm-cm p-type Du Pont single crystal silicon for which the lifetime was quoted as 100 microseconds.

The first set of experiments was carried out using a silicon sample in the form of a filament (approximately 0.2×0.2×1 cm) with electroplated nickel end contacts to which wires had been soldered. Two point contacts of tungsten wire 0.005 in. in diameter were placed close together on one of the faces of

the sample by means of micromanipulators. In the later experiments, the ends of the wires were reduced to a finer point by etching.

In the second set of experiments, which formed the greater part of the work, measurements were carried out on wedge-shaped specimens. In these experiments, the thick end of the wedge was clamped between spring-loaded copper blocks (base connection) and the emitter and collector wires were placed opposite to each other on the two inclined faces of the wedge as shown in Fig. 2.

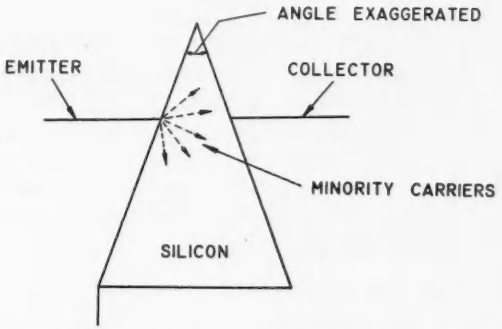

FIG. 2. Cross section of a wedge of silicon showing the position of the emitter and collector points.

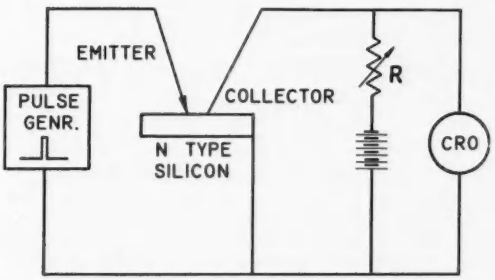

FIG. 3. Diagram of the circuit used to observe the diffusion pulse.

The circuit used is shown in Fig. 3. The resistor R of 1000 ohms was smaller than the collector resistance ($> 10^4$ ohms), so that the signal across R and hence that shown on the oscilloscope was approximately proportional to the collector current.

The forward pulse applied to the emitter was usually less than 1 microsecond in length and frequently less than 0.1 of a microsecond.

The experiments consisted of obtaining different oscilloscope traces for different emitter–collector spacings and measuring the variation in the time to maximum and in the decay following the maximum. The distances were measured with a travelling microscope.

EXPERIMENTAL RESULTS

Time to Maximum Measurements

Flat Surface Experiments

These measurements were carried out with a single filamentary sample A3 and are referred to in the results as the flat sample experiments, since both emitter and collector points were on the same surface.

Figure 4A shows a log–log plot of time to maximum against emitter–collector spacing for a surface treatment giving a shiny finish to the sample. This

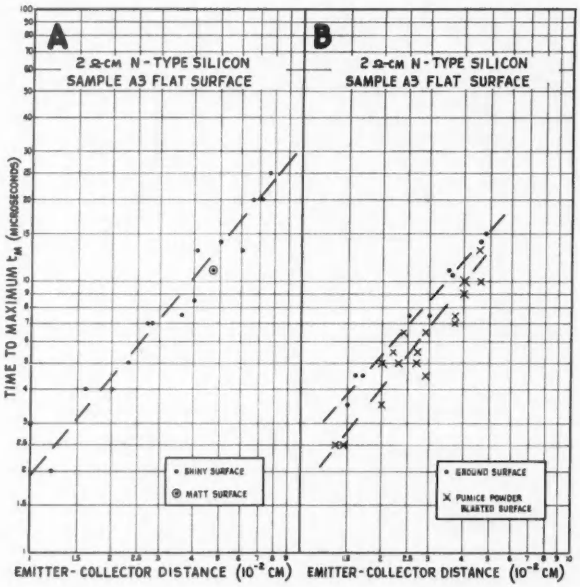

FIG. 4. Log–log plots of the time to collector maximum against the distance between emitter and collector points, on the same surface of 2-ohm-cm, *n*-type silicon sample A3. A shows results for a surface etched to give a shiny finish. B shows results for a surface ground on carborundum paper and also a surface blasted with pumice powder.

treatment consisted of first polishing the sample surface with progressively finer lapping powders and then etching it for 5 minutes in a 5:1 mixture of nitric and hydrofluoric acids. One point was obtained for a mat finish to the surface. The treatment in this case was an etch for 2 hours in a mixture of acetic, nitric, and hydrofluoric acids in the ratio 10:3:1. Another set of measurements was made on the same sample after the surface was rubbed on 400A carborundum paper. Yet another set of measurements was taken on the same sample, this time after air blasting with pumice powder to produce a pitted surface. The results for these two surface treatments are given in Fig. 4B.

For comparison purposes, the three average lines through the points are shown redrawn on a single graph in Fig. 6B. The ground surface on the

average appears to give the largest time to maximum values and the pumice blasted surface the least; the shiny surface values are between the two. From the slopes, the following empirical laws are found:

(12) $t_m = 4.9\times10^{-4}r^{1.21}$ (shiny surface),

(13) $t_m = 4.8\times10^{-4}r^{1.15}$ (ground surface),

(14) $t_m = 5.6\times10^{-4}r^{1.26}$ (blasted surface).

Thus it may be said that the experiments give approximately $t_m \propto r^{1.2}$ regardless of the surface treatment.

Wedge Experiments

The wedge experiments were carried out to ensure that diffusion was taking place through the bulk and not predominantly along the surface of the specimen. The wedge form of geometry enabled different emitter–collector distances through the bulk to be used. Three wedges were used. Each was prepared by lapping or grinding a specimen of silicon waxed to an inclined face set in a block of steel. The apex angles were kept small so that the small areas on the faces near the emitter and collector might be regarded, for theoretical purposes, as parallel.

Figure 5A shows the results for a wedge made from the same material as sample A3 used in the flat surface experiments. This wedge had an apex angle of 3° but later on it was reground without maintaining the original angle. Figure 5B shows the results for a sample A2 with an apex angle of 6°. Figure 6A shows results for a 17° wedge of *p*-type material.

The average lines drawn through the experimental points for the three wedges are redrawn together on Fig. 6B. The slopes for these lines are greater than those for the flat surface experiments. The empirical laws for the three lines are as follows:

(15) $t_m = 1.9\times10^{-3}r^{1.64}$ (sample A3),

(16) $t_m = 9.2\times10^{-4}r^{1.5}$ (sample A2),

(17) $t_m = 7.1\times10^{-4}r^{1.6}$ (Du Pont *p*-type sample).

Apart from the differences in the proportionality constants, the wedge experiments therefore give approximately $t_m \propto r^{1.6}$.

Decay Measurements

Figure 7 shows typical plots of the logarithm of the collector signal against time for three particular emitter–collector spacings. The decay curve in one case is a straight line. It is slightly convex in another case and slightly concave in the third. Despite the slight curvature observed in some of the cases, it was found that log–linear plots gave, in general, the nearest approach to straight lines. Other plots (log–log) for instance gave greater curvatures. The decays were thus described by a term $\exp(-t/\tau_1)$ and values of the so-called decay time τ_1 were obtained from the slopes of the lines. These values covered a wide range but were not completely random. Figure 8 shows τ_1 plotted

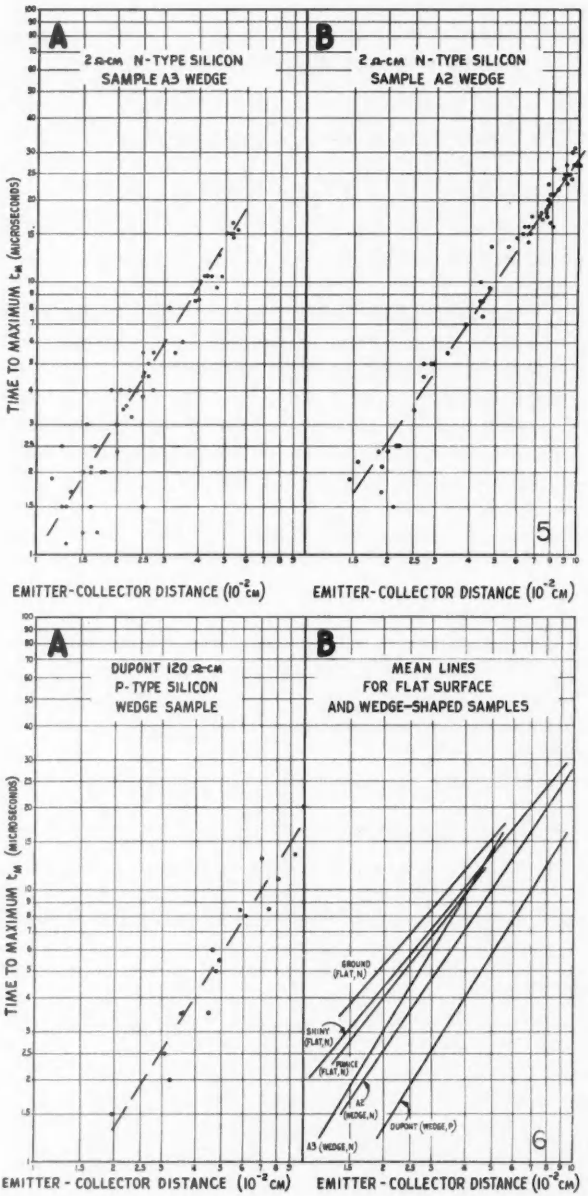

FIG. 5. Log–log plots of time to maximum against distance between emitter and collector points on wedges of 2-ohm-cm, *n*-type silicon. A shows results for wedge sample A3 with an original apex angle of 3° and B shows results for wedge sample A2 with an angle of 6°.

FIG. 6. Log–log plots of time to maximum against distance between emitter and collector points. A shows results for a 17° wedge sample of 120-ohm-cm, 100-microsecond *p*-type silicon. B shows all the average lines through the experimental points in the previous plots.

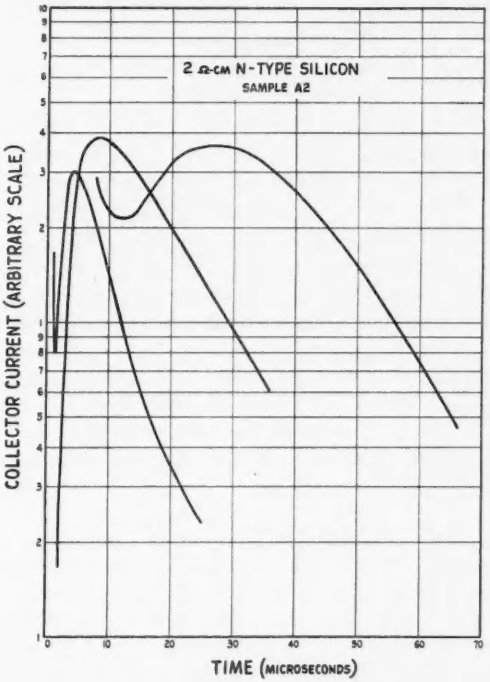

FIG. 7. Variation of the logarithm of the collector signal against time, taken from three typical oscilloscope traces.

against t_m and Fig. 9 shows it plotted against r. While there is considerable scatter in the points, indicating that some important factor is not kept constant, there is a general tendency for τ_1 to increase with t_m or r as indicated by the broken line in each case. There was no obvious difference between values of τ_1 for the flat surface and for the wedge experiments, although with such scatter present any small difference would not show up. At larger values of r (or t_m), τ_1 appears to flatten off somewhat. Linear–log plots for τ_1 and t_m and τ_1 and r appear to have the effect of straightening out the general trends. However, it is found that the variation in Fig. 8 may be described in the simplest way by a rough empirical formula of the form

$$\tau_1 = 10^{-2} t_m^{0.6}. \tag{18}$$

All the experiments were done in semidarkness to get the best sensitivity to resolve the maxima. The effect of steady light from a microscope lamp on the sample was generally to reduce the amplitude of the maximum without noticeably altering the time to maximum. While the decay time was slightly reduced under illumination, the variation with t_m (and r) was apparently still present.

Regarding the effect of the collector circuitry, it is estimated from the capacitances (preamplifier 25 $\mu\mu$f) and resistances (load resistance 10^3 ohms)

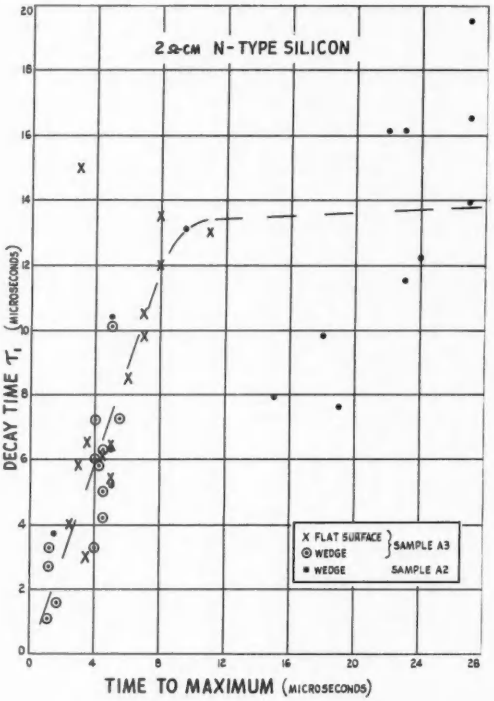

FIG. 8. Decay time τ_1 (determined from log–linear plots of collector signal versus time) plotted against time to maximum.

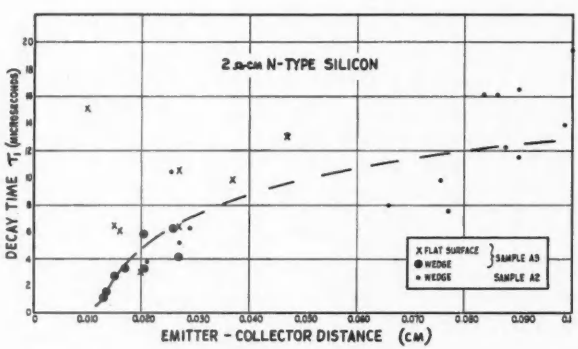

FIG. 9. Decay time τ_1 (determined from log–linear plots of collector signal versus time) plotted against emitter–collector spacing.

involved that they result in a time constant of less than 0.1 microsecond; the capacitance of the collector contact itself was less than 1 $\mu\mu$f. This has, therefore, a negligible effect on the decay curves.

Other Measurements

Effect of Injection Voltage on Decay Time

Increasing the amplitude of the injecting pulse did not produce a clear-cut effect but the general tendency was for the decay time τ_1 to increase slightly.

Effect of Emitter and Collector Fields on t_m

The influence of both fields was examined by measuring times to maximum firstly with increasing values of collector bias, secondly with increasing pulse generator amplitude settings, and thirdly with increasing injection pulse widths, keeping the two other variables constant each time. It was found that in all three cases the time to maximum decreased. However, extrapolation to zero values showed that a finite value of time to maximum would still be obtained for an injection pulse of very small amplitude and width with a very small value of collector bias. Thus we are justified in saying that the experimentally observed maximum is predominantly due to diffusion and not to drift in an electric field.

ANALYSIS OF RESULTS

Time to Maximum Results

There appears to be no definite order in the relative vertical positions of the experimental lines in Fig. 6B. At a given value of r, the ratio of t_m values might be expected to vary as D^{-1} (equation (4)) or as $D^{-\frac{1}{2}}\tau^{\frac{1}{2}}$ (equation (5)) but this is not so. Wedge sample A3 is of the same material as wedge sample A2 but the t_m values are roughly a third higher. For the p-type sample with a diffusivity about 4 times and a lifetime about 17 times as great, the t_m values are only about half those for sample A2. If an attempt is made to calculate values of t_m for the n-type material using equations (4) and (5), it is found taking $\tau = 6$ microseconds and $D = 6$ cm^2/sec that the values are larger than the experimental ones by roughly a factor of 2.

The empirical equations (12) to (17) show that the variation of t_m with r is neither quadratic as in equation (4) nor linear as in equation (5). Furthermore, detailed examination shows that the variation cannot be fitted by the more general relation (6), which applies not only to an infinite solid but also to a semi-infinite solid with $s = 0$ on the surface. In fact, even the theory with a non zero s in a semi-infinite solid is inadequate. This can be seen from Fig. 10 where $r^2/4D_p t_m$, obtained from the experimental results on flat shiny sample A3 and wedge sample A2, has been plotted against t_m. Equation (7) may be rewritten in the form

$$\frac{r^2}{4D_p t_m} = \frac{t_m}{\tau} + \frac{3}{2} + \epsilon.$$

Thus the plot should have a slope $1/\tau$ and an intercept on the ordinate axis of $3/2+\epsilon$. It is, however, apparent that the slope is not constant and the

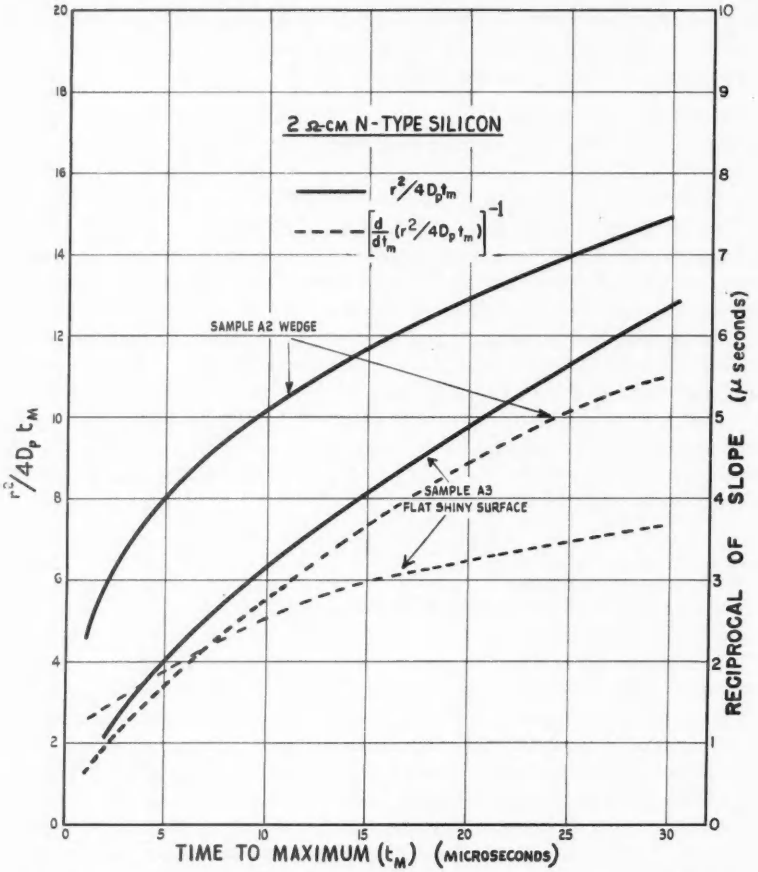

FIG. 10. Variation of $r^2/4D_p t_m$ with time to maximum obtained from the experimental t_m, τ plots for the flat shiny surface sample A3 and the wedge sample A2, taking $D_p = 6$ cm²/sec. The broken curves were obtained by taking reciprocals of slopes of the continuous curves.

extrapolated intercept does not lie between the values 3/2 and 5/2 as predicted. In these considerations ϵ varies sufficiently slowly with t_m to be taken as a constant. The theory with a constant lifetime is therefore clearly not sufficient. The variation of the reciprocals of the slopes, indicated by the broken lines in Fig. 10, shows a "lifetime" which apparently increases with t_m; a tendency to flatten off somewhat is seen at the higher values.

Another approach at analyzing the results is to use the one-surface theory to calculate s from equation (10). Unfortunately, such a calculation yields negative values. This is due to using the measured value for τ of 6 microseconds which does not satisfy inequality (11). To get positive values of s not

only must a smaller value of τ be used but also one which varies with t_m. Figure 11 shows a plot of X^{-1} and Y^{-1} (see equations (3), (3A), (9), and (9A))

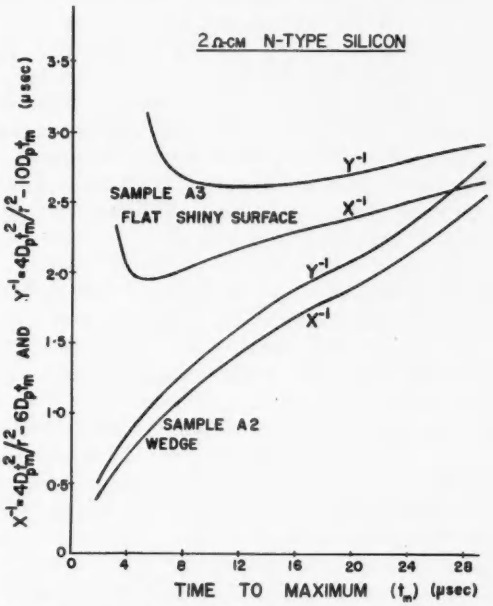

FIG. 11. Variation of $X^{-1} = 4D_p t_m^2/(r^2 - 6D_p t_m)$ and $Y^{-1} = 4D_p t_m^2/(r^2 - 10D_p t_m)$ with time to maximum obtained from the experimental t_m, r plots for the flat shiny surface sample A3 and the wedge sample A2, taking $D_p = 6$ cm²/sec. The quantities X^{-1} and Y^{-1} represent values of lifetime calculated on the assumption of a zero and infinite surface recombination velocity, respectively.

against t_m for the same two samples as in Fig. 10. The two curves for each sample represent values of τ calculated for the two extreme cases of zero and infinite s. To get positive finite values of s, by inequality (11), the calculated values of lifetime must lie between the two curves. Since both pairs of curves show, for the most part, an increase, the lifetime must also increase with t_m if the theory is correct. This result is thus the same as that deduced by the previous type of analysis. However, the magnitudes and the shapes of the curves in Figs. 10 and 11 are not the same.

Decay Time Results

If the decay time τ_1 is taken as a measure of the lifetime, then the increase of τ_1 with t_m in Fig. 8 is consistent with the variation already deduced from the analysis of the t_m, r curves. However, the magnitudes of τ_1 are roughly 3 and 5 times those of Figs. 10 and 11 respectively. From an analytical point of view, if empirical equation (18) is inserted in equation (5), it is found that $t_m = 3.6 \times 10^{-3} r^{1.45}$. Comparing with equation (16), namely $t_m = 0.9 \times 10^{-3} r^{1.5}$, this shows a reasonable agreement in the exponent but a disagreement

by a factor of 4 in the proportionality constant. This limited amount of agreement is surprising when one considers that the substitution procedure is inherently wrong, since the derivation of equation (5) was based anyway on the assumption of a constant lifetime.

DISCUSSION

While the "lifetimes" calculated in the previous section differ depending on how they are deduced, they all show a "lifetime" which decreases as the emitter–collector spacing is reduced. The differences are no doubt due to the inapplicability of the theory. For consistency, the theory should include in the original differential equation (1) a lifetime which depends on distance or concentration.

One possible way in which the lifetime could depend on concentration is as follows: It is estimated that about 10^{10} holes were injected during a pulse of 0.1 microsecond. This means that while the carriers were confined to a sphere of diameter 10^{-3} cm, the local concentration was about 10^{19} holes/cm^3. Direct electron–hole recombination can take place across the gap at a rate proportional to np/n_i^2 (van Roosbroeck and Shockley 1954), where n_i is the intrinsic density of electrons. If Δp is much larger than the density of minority carriers (p_0) but much less than that of the majority carriers (n_0) i.e. $p_0 \ll \Delta p \ll n_0$, then τ is a constant equal to $2n_i\tau_i/n_0$, where τ_i is the lifetime in intrinsic material; but if Δp is so large that it is even greater than the majority equilibrium density, i.e. $\Delta p \gg n_0$, then the decay of Δp with time becomes hyperbolic instead of exponential and the "lifetime" is found to be equal to the time itself. In this case, the "lifetime", starting from the bulk value, would decrease progressively on approaching the emitter point. For the n-type material used, this decrease would start when Δp exceeds $n_0 \simeq 10^{15}$/cm^3, that is, if bimolecular recombination were the only factor.

A lifetime dependent on excess concentration might also explain the t_m, r results on the 120-ohm-cm p-type silicon, which are particularly puzzling. This material shows the same type of dependence of t_m on r as in the case of the 6-microsecond n-type silicon. Yet the p-type material has a 100-microsecond lifetime which is much larger than all the measured t_m values. In this case we should have expected $t_m \propto r^2$ instead of the observed $t_m \propto r^{1.6}$. The magnitudes of t_m are also smaller than expected for such a lifetime. These facts could possibly be accounted for with a much smaller effective lifetime governed by the excess carrier concentration.

It should be mentioned that the assumption of a lifetime dependent on excess carrier concentration has two serious difficulties. The first of these is that the decay following the maximum would not be exponential. Hence the dependence on concentration, if it exists at all, cannot be too strong. Secondly the lifetime at a given value of r should decrease with increased injection of carriers, whereas in fact no such decrease was observed. This is not understood.

It should be mentioned here that Bath and Cutler (1958) have found that s in silicon depends on excess concentration but they do not believe body lifetime was affected.

Another factor besides lifetime which could be affected by excess carrier

concentration is the diffusivity which arises in the original differential equation through Fick's law. For large added hole concentrations $\Delta p = \Delta n = p = n$ and the ambipolar diffusivity consequently reduces to $D' = 2D_p (1+D_p/D_n)^{-1}$. Since $D_n > D_p$, D' is approximately $2D_p$. Thus D' could decrease from $2D_p$ near the point of injection to D_p a long distance from it where the hole concentration is low. Besides this variation, an increase with distance may be obtained if D_p and D_n are reduced by electron–hole scattering at the high excess concentration near the emitter point. Such a variation would affect the t_m, r curves and the calculated lifetimes.

Trapping (Haynes and Hornbeck 1955) is not thought to be an important effect in this work. While it could explain the values of decay time greater than 6 microseconds, it could not explain the many observed times less than this value.

The scatter of the experimental points in Figs. 4, 5, and 6 is somewhat larger than can be accounted for by an estimation of errors in the measurements of t_m and r. The same is true for Figs. 8 and 9 but to an even greater extent. For these plots one naturally thinks of the capacitance and resistance of the collector point contact as uncontrolled parameters causing the scatter. However, these quantities have values which are apparently too small to affect the results. If indeed such factors had been important, there might have been a possible, though unlikely, explanation for the variation of decay time with r; it was found necessary in the experiments to increase the pressure on the points as r was increased and this in turn could result in a change of capacitance and resistance of the collector point with distance.

It is unfortunate that no two-surface theory is available for comparison with the experimental results in this paper, although the one-surface theory of van Roosbroeck does correspond to the flat surface experiments. However, the indications are that a two-surface theory alone would anyway be inadequate. What is required is a theory which takes into account at the outset enhanced recombination and modification of the diffusivity near the emitter point.

ACKNOWLEDGMENTS

It is a pleasure for the author to acknowledge the assistance of his colleagues, particularly F. S. Eadie and S. D. Rosenbaum. The author wishes to thank W. van Roosbroeck for very helpful discussions in connection with the application of his theory and T. M. Buck and F. S. McKim for their measurement of bulk lifetime at the Bell Telephone Laboratories. He also expresses his thanks to A. B. Hunt, Director of Northern Electric Laboratories, for permission to publish this paper.

REFERENCES

BATH, H. M. and CUTLER, M. 1958. J. Phys. Chem. Solids, **5**, 171.
HAYNES, J. R. and HORNBECK, J. A. 1955. Phys. Rev. **100**, 606.
VAN ROOSBROECK, W. 1953. Phys. Rev. **91**, 282.
——— 1955. J. Appl. Phys. **26**, 380.
VAN ROOSBROECK, W. and SHOCKLEY, W. 1954. Phys. Rev. **94**, 1558.
SHOCKLEY, W. 1950. Electrons and holes in semiconductors (D. van Nostrand Co., Inc., New York), p. 349.
SHOCKLEY, W., PEARSON, G. L., and HAYNES, J. R. 1949. Bell System Tech. J. **28**, 344.

NOTES

STRAIN IN CRYSTALS OF YTTRIUM IRON GARNET

ARCHIBALD W. SMITH AND GERALD W. WILLIAMS

Yttrium iron garnet ($Y_3Fe_5O_{12}$) is a ferrimagnetic oxide which can be prepared in the form of small crystals by growth from a melt (Nielsen and Dearborn 1958). In a recent paper, Smith and Williams (1960) pointed out that an unusual type of strain occurs near (112) growth faces of these crystals. The strain axis, which is a direction of easy magnetization, is inclined to the growth face, and appears to be introduced during the growth of the crystals. This is to be contrasted with the strain which is often introduced during grinding of the crystals, and results in a strain axis perpendicular to the ground surface. As an extension of the work on (112) growth faces, the magnetic strain anisotropy has been investigated by means of ferromagnetic resonance. This method is convenient with yttrium iron garnet because of its unusually narrow resonance line width. The measurements have been carried out on an optically transparent disk, and the optical birefringence has been investigated with a polarizing microscope. The magnetic and optical anisotropy due to the strain have been correlated by considering the magnetoelastic and photoelastic interactions. An explanation of the magnetic birefringence is proposed in terms of the magnetostrictive and photoelastic effects.

EXPERIMENTAL

Two samples cut from the same crystal were investigated. They were prepared by grinding and polishing thin slices from the crystal, and cutting disks from these with an ultrasonic "cookie cutter". Sample 1 had a (112) growth face on one side, and was 0.103 cm in diameter and 0.0023 cm thick. The crystal was strained, with the strain axis inclined to the growth face. The $[\bar{1}\bar{1}1]$ direction was located in the plane by X-ray techniques. The domain structure took the form of strips running across the sample. The magnetization was parallel to the strain axis, and was antiparallel in adjacent domains. The strips were 2° from $[\bar{1}\bar{1}1]$ toward $[\bar{1}10]$. The sample exhibited a permanent birefringence with the direction of vibration of the slow wave 6° from $[\bar{1}\bar{1}1]$ toward $[\bar{1}10]$.

The direction of minimum anisotropy energy in the plane of the disk is $[\bar{1}\bar{1}1]$ for the intrinsic negative cubic anisotropy, and along the projection of the strain axis for the strain anisotropy. It will be seen below that the latter is nearly uniaxial in form. As the domain strips indicate the position of the composite energy minimum, it follows that the projection of the strain axis, which must coincide with the direction of vibration of either the fast or slow wave, was 6° from $[\bar{1}\bar{1}1]$. The strain axis itself was inclined at 60° to the plane. Thus the strain axis was close to the [001] direction, which occurs at 55° above $[\bar{1}\bar{1}1]$. The inclination was determined by tilting the sample about an axis perpendicular to the domains until a position was found where the contrast between the domains disappeared. This occurs when the light path

inside the sample is parallel to the strain axis. The procedure for this experiment was the same as previously described (Smith and Williams 1960).

The retardation due to the birefringence was measured with the magnetization parallel to the $[\bar{1}\bar{1}1]$ and $[\bar{1}10]$ directions. The results over the main part of the sample were 7.5×10^{-7} and 10.3×10^{-7} cm, respectively. In a sharply defined region occupying about 15% of the disk, the results were 11.0×10^{-7} and 14.2×10^{-7} cm. As the inclination of the strain axis was the same in this region, these results indicate that the magnitude of the strain was greater. This region was located along the edge of the disk in the $[\bar{1}\bar{1}1]$ direction from the center. The difference between the two values for each region gives an average retardation of 1.5×10^{-7} cm for the magnetic birefringence, and shows that the direction of vibration of the fast wave is parallel to the magnetization.

Sample 2 was cut from material about 0.025 cm below a (112) growth face. It was ground on both sides and had a strain axis perpendicular to its plane. The diameter was 0.127 cm and the thickness 0.0036 cm. The domain structure took the form of an irregular maze pattern. The magnetization was parallel to the strain axis, and was antiparallel in adjacent domains.

The resonance field measurements for the two samples are shown in Fig. 1.

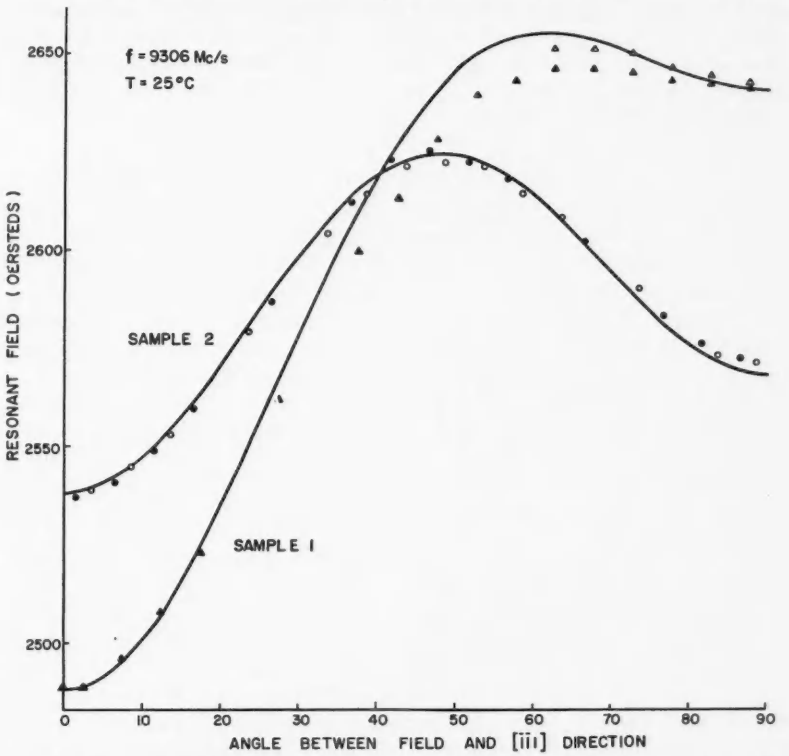

FIG. 1. Resonant field plotted against angular position in plane of disk. The solid points were taken between 0 and 90°, and the open points between 90° and 180°. The curves are theoretical functions which have been fitted to the experimental points.

These were obtained using a reflection cavity technique similar to that described by Artman and Tannenwald (1955). The disks were mounted so that they could be tilted to align the plane of the disk with the field, and rotated to vary the angular position of the field in the plane. The field was measured with a nuclear magnetic resonance gaussmeter.

THEORETICAL

The resonant frequency ω of a ferrite disk with the field in the plane of the disk is (cf. Artman 1957)

$$\left(\frac{\omega}{\gamma}\right)^2 = H^2+H\left[4\pi M(1-3n)+\frac{1}{M}(E_{A\theta\theta}+E_{A\phi\phi})\right]+4\pi(1-3n)E_{A\phi\phi},$$

where H is the external field, θ and ϕ are the polar and azimuthal angles, respectively, of the magnetization M, and γ is the gyromagnetic ratio. E_A is the anisotropy energy, and $E_{A\theta\theta}$ and $E_{A\phi\phi}$ are the second order partial derivatives with respect to θ and ϕ. This expression is correct to the first order in the angular deviation of M and H. In the resonance measurements described here, this deviation is less than 2°, and it will be assumed that M and H are aligned.

The anisotropy energy is the sum of the magnetocrystalline and magnetoelastic or strain contributions. The former can be adequately expressed by a first-order term only (Dillon 1957). The latter will be written for a uniform strain ϵ, in terms of the two magnetostrictive constants λ_{100} and λ_{111} (cf. Baltzer 1957). The total energy is then

$$E_A = K\sum_{i>j}\alpha_i^2\alpha_j^2-\frac{3}{2}\lambda_{100}(C_{11}-C_{12})\epsilon\sum_i\alpha_i^2\gamma_i^2-6\lambda_{111}C_{44}\epsilon\sum_{i>j}\alpha_i\alpha_j\gamma_i\gamma_j$$

where the α_i and γ_i are the direction cosines of the magnetization and strain axis, respectively, referred to the edges of the unit cell. K is the magnetocrystalline anisotropy constant, and C_{11}, C_{12}, and C_{44} are the stiffness constants. If the strain is along a cube edge, or if the crystal behaves isotropically, i.e. $\lambda_{111}C_{44} = \frac{1}{2}\lambda_{100}(C_{11}-C_{12})$, the strain contribution reduces to a uniaxial term $-K_s\cos^2\delta$, where $K_s = (3/2)\lambda_{100}(C_{11}-C_{12})$ and δ is the angle between the magnetization and the strain axis. The experimental results can be adequately represented by taking a uniaxial term only, with the projection of the strain axis along $[\bar{1}\bar{1}1]$. In terms of the co-ordinate system of Fig. 2,

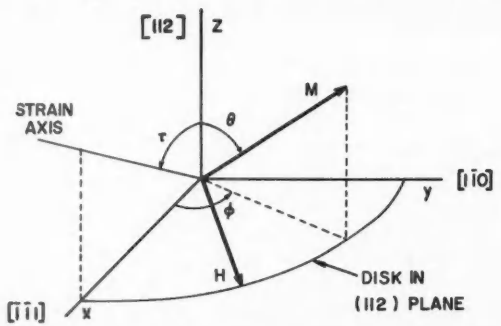

FIG. 2. Co-ordinate system for disk in (112) plane. Polar angles are measured from [112], azimuthal angles from $[\bar{1}\bar{1}1]$.

$$E_A = K[\sin^4\theta(\tfrac{1}{4}\sin^4\theta+\tfrac{1}{3}\cos^4\phi)+\tfrac{1}{4}\cos^4\theta-\tfrac{\sqrt{2}}{3}\sin\theta\cos^3\theta\sin\phi$$
$$+\sin^2\theta\cos\theta\sin^2\phi(\tfrac{1}{2}\cos\theta+\sqrt{2}\sin\theta\cos\phi)]$$
$$-K_s(\sin\tau\sin\theta\cos\phi+\cos\tau\cos\theta)^2,$$

and the partial derivatives are

$$E_{A\theta\theta} = K(\sin^2\phi\cos^2\phi-\tfrac{4}{3}\cos^4\phi)-2K_s[1-\sin^2\tau(1+\cos^2\phi)]$$

and

$$E_{A\phi\phi} = K(7\cos^2\phi\sin^2\phi-\sin^4\phi-\tfrac{4}{3}\cos^4\phi)-2K_s\sin^2\tau(1-2\cos^2\phi).$$

Examination of the above equations shows that K_s and τ, the polar angle of strain axis, enter only in the form $4\pi M(1-3n)-2K_s/M$ and $(2K_s/M)\sin^2\tau$. This means that K_s cannot be determined independently of $4\pi M(1-3n)$ and τ by resonance measurements alone.

The permanent birefringence which occurs in sample 1 is due to the photoelastic effect of the strain. This effect has been evaluated in terms of the elasto-optical coefficients for a uniform strain along the [001] direction, which is nearly the case in sample 1. The index of refraction for light passing through the strained crystal in the [112] direction is given by the index ellipse

$$\frac{\cos^2\psi}{n_\parallel^2}+\frac{\sin^2\psi}{n_\perp^2} = 1,$$

where ψ is the angle of the plane of polarization with respect to $[\bar{1}\bar{1}1]$. In an unstrained crystal $n_\parallel = n_\perp = n$. In terms of the elasto-optical coefficients P_{11} and P_{12} (Nye 1957), $n_\parallel-n_\perp = n^3(P_{11}-P_{12})\epsilon/6$. The measured retardation is equal to $d(n_\parallel-n_\perp)$, where d is the thickness of the sample.

The ratio of the magnetic and optical anisotropy is independent of the strain:

$$\left|\frac{K_s}{n_\parallel-n_\perp}\right| = \frac{9(C_{11}-C_{12})}{n^3}\left|\frac{\lambda_{100}}{P_{11}-P_{12}}\right|.$$

In order to establish the validity of the theory, this ratio will be evaluated and compared to the experimental result. The only quantity which has been measured is the index of refraction: $n = 2.24$. The others may be estimated as follows: $\lambda_{100} \approx 5\times10^{-6}$ (cf. Baltzer 1957, Table II), $C_{11}-C_{12} \approx 10^{12}$ dynes/cm^2 (cf. A.I.P. Handbook 1957, Table 2f-1), and $P_{11}-P_{12} \approx 0.2$ (cf. Nye 1957, Table 17). The result is $K_s/(n_\parallel-n_\perp) \approx 2\times10^7$ dynes/cm^2.

The magnetostrictive and photoelastic effects provide a possible explanation of the magnetic birefringence. In contrast to the Faraday rotation, the magnetic birefringence in yttrium iron garnet is only weakly dependent on wavelength, which suggests that it has a different origin. The Faraday rotation arises from the effect of the internal magnetic field on electric dipole transitions in the Fe^{3+} ion (Clogston 1959). The photoelastic birefringence arising from the magnetostriction has been evaluated for an isotropic medium, with the magnetization perpendicular to the line of sight. Under these conditions, the strain is uniform and either the major or minor axis of the index ellipse is

parallel to the magnetization. In an anisotropic medium this would not generally be the case. The difference in the principal indices of refraction is $n_\parallel - n_\perp = \frac{3}{4}\lambda n^3(P_{11}-P_{12})$, where λ is the isotropic magnetostriction. Using the same data as before, this quantity is estimated to be $|n_\parallel - n_\perp| \approx 8\times10^{-6}$.

DISCUSSION

The resonance equation has been plotted in the form H vs. ϕ for sample 2, with $\tau = 0$ and taking $K/M = -42$ oersteds and $g = 2.005$ ($\gamma = ge/2mc$ = 2.8064 Mc/sec oersted) from Dillon (1957). The value $4\pi M(1-3n)-2K_s/M = 1645$ oersteds was derived from the point at $\phi = 0$. It can be seen from Fig. 1 that this gives a satisfactory fit to the experimental points. As the sample is appreciably strained, this means that the crystal is nearly isotropic in behavior, i.e. $\lambda_{100}(C_{11}-C_{12}) \approx 2\lambda_{111}C_{44}$. The fact that the strain anisotropy overrides the cubic indicates that $2K_s/M \gtrsim 80$ oersteds; this inequality cannot be calculated exactly because the first derivative of the cubic anisotropy is not zero in the [112] direction. A value of $n = 0.021$ was calculated on the assumption that the sample was an ellipsoid, although this is not an adequate representation. A value of $4\pi M \gtrsim 1840$ gauss is then found. This is high compared to most published values, which fall in the range 1720 ± 40 gauss, but is compatible with the value of 1890 gauss recently found for a particular batch of crystals (Rossal 1960).

For sample 1, the resonance equation has been plotted by deriving $4\pi M(1-3n)-2K_s/M = 1500$ oersteds and $(2K_s/M)\sin\tau = 76.7$ oersteds from the points at $\phi = 0$ and 90°. The fit is not as good in this case, but is still satisfactory considering that the sample is not uniformly strained. The strain anisotropy is expected to be uniaxial in this case because the strain axis is close to [001]. Taking $\tau = 30°$ and $n = 0.017$, the values $2K_s/M = 300$ oersteds and $4\pi M = 1900$ gauss are obtained. The difference between the two values of $4\pi M$ may be due to an inadequate analysis of the non-uniform sample, or may indicate an actual difference between the growth face and the inner part of the crystal.

In evaluating the ratio $|K_s/(n_\parallel - n_\perp)|$ experimentally, it will be assumed that the resonance experiment measures a weighted average of the strain anisotropy in the two regions of sample 1. The retardation calculated on the same basis is 1.0×10^{-6} cm. The experimental ratio is then $|K_s/(n_\parallel - n_\perp)| = 4.8\times10^6$ dynes/cm^2, which is in satisfactory agreement with the predicted value. The corresponding value of the strain ϵ is about 2×10^{-3}. Thus it is possible to make a unified analysis of the magnetic and optical properties of the strained crystals. For the magnetic birefringence, $|n_\parallel - n_\perp| = 6.5\times10^{-5}$ experimentally, which is about 10 times the predicted value. It is clear that the mechanism outlined here will make an appreciable contribution to the magnetic birefringence, although it may not be able to account for all of it. Measurements of λ and $P_{11}-P_{12}$ would be required to make a more conclusive analysis, as well as more extensive experiments on the magnetic birefringence itself.

AMERICAN INSTITUTE OF PHYSICS HANDBOOK. 1957. (McGraw-Hill Book Co., New York).
ARTMAN, J. O. 1957. Phys. Rev. **105**, 74.
ARTMAN, J. O. and TANNENWALD, P. E. 1955. J. Appl. Phys. **26**, 1124.
BALTZER, P. K. 1957. Phys. Rev. **108**, 580.
CLOGSTON, A. M. 1959. J. phys. radium, **20**, 151.
DILLON, J. F. 1957. Phys. Rev. **105**, 759.
NIELSEN, J. W. and DEARBORN, E. F. 1958. J. Phys. Chem. Solids, **5**, 202.
NYE, J. F. 1957. Physical properties of crystals (Clarendon Press, Oxford).
ROSSAL, F. C. 1960. J. Appl. Phys. **31**, 2273.
SMITH, A. W. and WILLIAMS, G. W. 1960. Can. J. Phys. **38**, 1187.

RECEIVED JANUARY 23, 1961.
ELECTRONICS LABORATORY,
DEFENCE RESEARCH TELECOMMUNICATIONS ESTABLISHMENT,
DEFENCE RESEARCH BOARD,
OTTAWA, ONTARIO.

THE *K* INTERNAL CONVERSION COEFFICIENT OF THE 412-KEV TRANSITION IN Hg^{198}*

J. L. WOLFSON

Hamilton, Frey, and Hultberg (1960) have recently measured α_K, the *K* internal conversion coefficient of the 412-kev transition in Hg^{198} by the internal–external method (Hultberg and Stockendal 1959*a*; Hultberg 1959) arriving at a value of $(2.44\pm0.08)\times10^{-2}$. Using the same method, de Vries *et al.* (1960) measured the value to be $(2.52\pm0.13)\times10^{-2}$, whereas employing the more common method of comparing the area of the *K* line to that of the beta spectrum, de Vries *et al.* arrived at the value $(2.41\pm0.09)\times10^{-2}$. These values are all lower than most determinations of this quantity (a complete listing is given in Nuclear Data Sheets). The most accurate determination, made by Wapstra *et al.* (1959), is $(2.81\pm0.05)\times10^{-2}$.

Hamilton *et al.* point out that their value is considerably lower than the theoretical value of 3.00×10^{-2} (Sliv and Band 1956; Rose 1958) and regard it as anomalously low, since the total conversion coefficients of other *E*2 transitions, in low *Z* elements, viz. Co^{58} (Frey, Hamilton, and Hultberg 1960) and Sc^{46} (Hultberg, Frey, and Hamilton 1960), measured by the same method, have been found to be in good agreement with the theoretical values of Rose (1958). They conclude that the latest theoretical *E*2 conversion coefficients of high *Z* unhindered transitions may be in substantial error.

It is the purpose of this communication to draw attention to hitherto unreported measurements made some years ago at the Chalk River Laboratories of Atomic Energy of Canada Limited, which have a bearing on this question. In these measurements α_K for the 412-kev transition was measured relative to α_T, the total internal conversion coefficient, for the 1.33-Mev and 1.17-Mev transitions in Ni^{60}, whence it becomes possible to deduce the ratio

*Issued as N.R.C. No. 6256.

of α_K, for the 412-kev transition to each of the values of α_K for the 1.33-Mev and 1.17-Mev transitions in Ni^{60}. The method employed avoided comparisons of line areas with integrated beta spectra on the one hand, and on the other, achieved a comparison of the internal conversion coefficients of an $E2$ transition in a high Z nuclide (412 kev in Hg^{198}) with those of two $E2$ transitions in a low Z nuclide (1.33 and 1.17 Mev in Ni^{60}). The results obtained do not support the findings of Hamilton, Frey, and Hultberg. The ratios obtained are found to be somewhat higher than the theoretical ratios.

The measurements made involved the determination of two quantities: the relative numbers of conversion electrons from the transitions in question, and the numbers of quanta. The former were determined by comparison of the areas of the corresponding internal conversion lines in the conversion electron spectra from Au^{198} and Co^{60} sources, using a magnetic lens spectrometer. The latter were deduced from the measured disintegration rates of the same sources. This procedure avoids difficulties inherent in determining intensities of beta-ray spectra, but there is an assumption of constant spectrometer transmission over the energy range 328 kev to 1.32 kev. There are experimental checks which justify this assumption in that determinations of the intensities of conversion lines obtained with the spectrometer have been found to be in good agreement with identical measurements made elsewhere on other instruments. As an example, the intensity of the line at 9988 gauss cm to that at 2607 gauss cm in the conversion electron spectrum of RdTh active deposit, 0.099 ± 0.003 as found with the present instrument (Elliott *et al.* 1954), compares with the value 0.101 ± 0.002 as found by Krisiuk *et al.* (1956). This example is quoted as being particularly pertinent since in the latter measurement the question of penetration of counter slit edges by the energetic conversion electrons received careful study.

The source of Au^{198} was prepared by neutron irradiation of gold leaf of thickness 200 $\mu g/cm^2$. The activity of the source was measured by direct comparison with a standard Au^{198} source supplied by the standards laboratory of Atomic Energy of Canada Limited. The comparison was made by gamma-ray counting using a sodium iodide detector. The activity of the standard source had been measured to better than 1% and the comparison was made with an accuracy of better than 1%. In deducing the number of 412-kev quanta from the disintegration rate, a value of $\alpha_T = 0.041$ was assumed. The findings of Hamilton *et al.* (1960) and de Vries (1960) for α_K would lead to a value of $\alpha_T = 0.036$, with a resulting uncertainty, on this account, of about $\frac{1}{2}\%$ in the number of 412-kev quanta. The total uncertainty in the number of 412-kev quanta is estimated to be less than 2%.

Sources of Co^{60} were prepared by evaporation from $Co(NO_3)_2$ solution. Average source thickness was about 200 $\mu g/cm^2$. Because the transitions studied were of high energy, and also because of the high specific activity of the Co^{60} solution, uniformity of deposition was not of primary importance. Nevertheless since uniformity could not be assured by this method of source preparation, three separate sources were prepared and measurements made with all three. As for the Au^{198} source the disintegration rates of the sources

were measured by comparison with a standard source, supplied by the Atomic Energy of Canada Limited standards laboratory. The number of 1.33-Mev and 1.17-Mev quanta from each source was deduced with an accuracy of about $1\frac{1}{2}\%$.

The conversion lines from the Au^{198} source and one of the Co^{60} sources (source no. 2) are shown in Fig. 1. For the Ni^{60} conversion lines, the L and

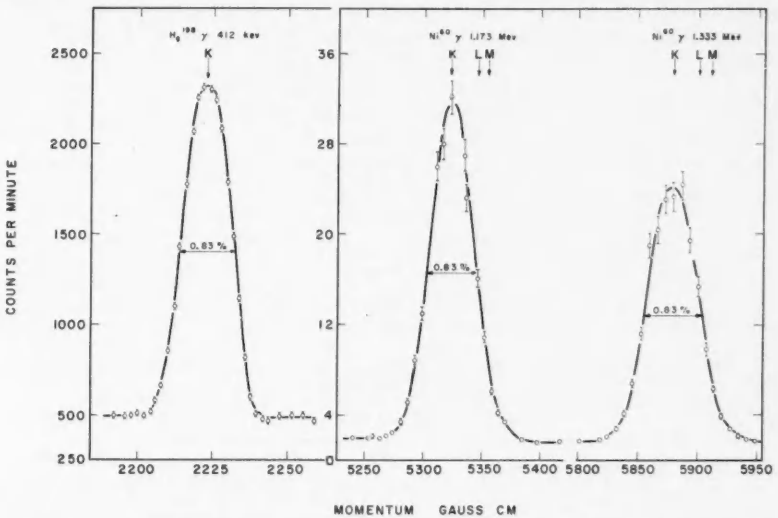

FIG. 1. Internal conversion lines of the 412-kev transition in Hg^{198} and of the 1.17- and 1.33-Mev transition in Ni^{60}. The vertical bars represent standard deviations of the plotted points.

M lines are not resolved from the K lines. Using the data of Kamada *et al.* (1958), who found that for each of the transitions the ratio $K/(L+M)$ was 9.1 ± 0.5, it was possible to make a correction for the L and M line contributions to the line areas. This leads to a value of $\alpha_K = (0.900\pm0.005)\alpha_T$ for each of the transitions, where $\alpha_T = \alpha_K+\alpha_L+\alpha_M$. (It should be noted that using the theoretical values of Rose (1958) for the internal conversion coefficients, and performing the necessary extrapolations, leads to a value $\alpha_K = 0.888\alpha_T$.)

One further correction was required. The three Co^{60} sources had diameters respectively of 2.35, 2.30, and 1.75 mm whereas the Au^{198} source shown in Fig. 1 had a diameter of 2.30 mm. In order to determine the effect of source diameter on line area, Au^{198} sources of diameters 1.08, 2.30, 3.65, and 4.00 mm were prepared, their relative activities measured, and the area of the γ 412-kev K lines from each of the sources measured in the spectrometer. It was found that for diameters close to 2 mm the ratio of line area to source activity varied only slightly with source diameter. Relative to the 2.30 mm diameter sources, corrections of -1.4% and 0% were required for the 1.75 mm and 2.35 mm sources respectively.

The results obtained cannot be compared directly with the theoretical values of Sliv and Band (1956) since these authors have not computed values for $Z < 33$. Nor can they be compared directly with the theoretical values of Rose (1958) since Rose has not given values for energies $>2.0\ mc^2$. Extrapolation of the computed values of Rose indicates, however, that the theoretical values of α_K for the 1.33-Mev and 1.17-Mev transitions are expected to be, within about 1%, 1.12×10^{-4} and 1.48×10^{-4} respectively. The theoretical value of α_K for the 412-kev transition in Hg^{198} is 3.00×10^{-2} (Sliv and Band 1956).

The ratios of α_K for the 412-kev transition in Hg^{198} to each of the values of α_K for the 1.33-Mev and 1.17-Mev transitions in Ni^{60}, i.e. $\alpha_K(Hg^{198})/\alpha_K(Ni^{60})$, were found to be:

	Co^{60} sources			
Transition in Ni^{60} (Mev)	No. 1	No. 2	No. 3	Means
1.33	280	290	278	283±12
1.17	217	223	—	220±10

A comparison with the theoretical values, and with the results of Hamilton, Frey, and Hultberg (1960), gives the following for the same ratios:

Transition in Ni^{60} (Mev)	This work	Theoretical	$\frac{\alpha_K(Hg^{198}, \text{Hamilton } et\ al.)}{\alpha_K(Ni^{60}, \text{theoretical})}$
1.33	283±12	268	218±7
1.17	220±10	203	165±5

The results do not support the tentative conclusions of Hamilton *et al.* that α_K for the 412-kev transition in Hg^{198} is anomalously low. The experimentally determined ratios found in this work are actually somewhat higher than the theoretical ratios.

The results do not of course lead directly to a value for α_K for the 412-kev transition in Hg^{198}. If the theoretical values of α_K for the 1.33- and 1.17-Mev transitions in Ni^{60} are combined with the results, values of $(3.17\pm0.16)\times10^{-2}$ and $(3.25\pm0.16)\times10^{-2}$ are obtained for α_K for the 412-kev transition. Most experimental values (Nuclear Data Sheets) of α_K for the Ni^{60} transitions are higher than the theoretical ones, leading to even larger values for α_K for the 412-kev transition. De Vries (1960) has pointed out, however, that if Hultberg and Stockendal's (1959*b*) data are combined with Colgate's (1952) value for the photoelectric cross section of uranium at 1.33 Mev, then a value of 0.98×10^{-4} (±6%) is obtained for α_K for the 1.33-Mev transition. If this value be combined with the corresponding experimental ratio above, then a value of 2.78×10^{-2} (±7%) is obtained for α_K for the 412-kev transition in Hg^{198}, in agreement with the determination of Wapstra *et al.* (1959), of $(2.81\pm0.05)\times10^{-2}$.

ACKNOWLEDGMENTS

The author acknowledges with thanks provision of the Co^{60} and Au^{198} standards by Messrs. R. C. Hawkings and W. F. Merritt, formerly of the standards laboratory of Atomic Energy of Canada Limited. The author is also indebted to Dr. J. S. Geiger of the Atomic Energy of Canada Limited for a critical discussion of this work.

COLGATE, S. A. 1952. Phys. Rev. **87**, 592.
DE VRIES, C. 1960. Thesis, University of Amsterdam, p. 122.
DE VRIES, C., BLEEKER, E. J., and SALOMONS–GROBBEN, MRS. N. 1960. Nuclear Phys. **18**, 454.
ELLIOTT, L. G., GRAHAM, R. L., WALKER, J., and WOLFSON, J. L. 1954. Unpublished work.
FREY, W. F., HAMILTON, J. H., and HULTBERG, S. 1960. Bull. Am. Phys. Soc. **5**, 448.
HAMILTON, J. H., FREY, W. F., and HULTBERG, S. 1960. Bull. Am. Phys. Soc. **5**, 449.
HULTBERG, S. 1959. Arkiv Fysik, **15**, 307.
HULTBERG, S., FREY, W. F., and HAMILTON, J. H. 1960. Bull. Am. Phys. Soc. **5**, 449.
HULTBERG, S. and STOCKENDAL, R. 1959*a*. Arkiv Fysik, **4**, 565.
——— 1959*b*. Arkiv Fysik, **15**, 355.
KAMADA, K., TERANISHI, T., and YOSHIZAWA, Y. 1958. J. Phys. Soc. Japan, **13**, 763.
KRISIUK, E. M., VITMAN, A. D., VOROB'EV, V. D., VOROB'EV, I. V., IL'IN, K. I., LATYSHEV, G. D., LISTENGARTEN, M. A., and SERGEEV, A. G. 1956. Izvest. Akad. Nauk. S.S.S.R. **20**, 883. (Translation: Bull. Acad. Sci. U.S.S.R. **20**, 803.)
ROSE, M. E. 1958. Internal conversion coefficients (North-Holland Publishing Co., Amsterdam).
SLIV, L. A. and BAND, I. M. 1956. Leningrad Physico-Technical Institute, Academy of Sciences of the U.S.S.R. (Translation: 1957. Report 57 ICC K1, Physics Dept., University of Illinois.)
WAPSTRA, A. H., NIJGH, G. J., SALOMONS–GROBBEN, N., and ORNSTEIN, L. TH. M. 1959. Nuclear Phys. **9**, 519.

RECEIVED JANUARY 11, 1961.
X-RAYS AND NUCLEAR RADIATIONS LABORATORY,
DIVISION OF APPLIED PHYSICS,
NATIONAL RESEARCH COUNCIL,
OTTAWA, CANADA.

LETTERS TO THE EDITOR

Under this heading brief reports of important discoveries in physics may be published. These reports should not exceed 600 words and, for any issue, should be submitted not later than six weeks previous to the first day of the month of issue. No proof will be sent to the authors.

Frequency Measurement of Standard Frequency Transmissions[1,2]

Measurements are made at Ottawa, Canada, using N.R.C. caesium-beam frequency resonator as reference standard (with an assumed frequency of 9 192 631 770 c.p.s.). Frequency deviations from nominal are quoted in parts per 10^{10}. A negative sign indicates that the frequency is below nominal.

Date, February 1961	MSF, 60 kc/s	GBR, 16 kc/s		WWVB, 60 kc/s
		6½-hour average*	24-hour average†	
1	−160	−151	−152	N.M.
2	−158	−150	−151	N.M.
3	−162	−151	−153	−155
4	−148	−153	−152	−150
5	−153	−146	−148	N.M.
6	−155	−151	−150	N.M.
7	−160	−150	−149	−156
8	−156	−143	−144	−151
9	−155	−149	−149	−153
10	−152	−143	−146	−162
11	−146	−144	−144	−147
12	−146	−142	−142	N.M.
13	−150	−143	−141	−150
14	N.M.	−141	−144	−150
15	−148	−140	−141	−153
16	−152	−137	−138	−154
17	−157	−144	−143	−157
18	−155	−140	−143	−148
19	−143	−143	−141	−145
20	−155	−142	−142	−156
21	−155	−145	−145	−151
22	−158	−142	−143	−152
23	−162	−145	−147	−153
24	−160	−147	N.M.	−154
25	−152	−148	−150	−147
26	N.M.	−151	−148	N.M.
27	−151	−147	−152	−152
28	−150	−142	−145	−152
Average	−154	−145	−146	−152
Midmonthly mean of WWV	−150			

NOTE: N.M. no measurement.
*Time of observations: 23.30 to 06.00 hours U.T.
†Time of observations: 15 to 15 hours U.T.

RECEIVED MARCH 10, 1961.
S. N. KALRA
DIVISION OF APPLIED PHYSICS,
NATIONAL RESEARCH COUNCIL,
OTTAWA, CANADA.

[1]Issued as N.R.C. No. 6259.
[2]Cf. Kalra, S. N. 1959. Can. J. Phys. **37**, 1328.

The Conversion Electron Spectrum from a Mass-separated Source of Xe^{133}*

A mass separator of the Nobel Institute type (Alväger and Uhler 1958) has recently been installed and brought into operation in the Chemistry Division of this laboratory. It is designed primarily to produce isotopically pure radioactive materials for sources in nuclear spectroscopy or for radiochemical investigations. It can also provide small quantities of stable material of high isotopic purity for use, for example, in targets for nuclear reaction studies.

As a test of the performance of the mass separator, we have prepared a source of Xe^{133}, 1 mm wide by 20 mm long, for use with the Chalk River iron-free β-ray spectrometer (Graham *et al.* 1960). An iron ampoule containing natural Xe gas was irradiated for 6 days in a neutron flux of 2.5×10^{14} cm^{-2} sec^{-1} in the NRU reactor. We are indebted to Dr. R. O. Kelly for supplying the container and for arranging this irradiation. The gas was then admitted to the ion source of the mass separator at an accelerating potential of 30 kv. The focused Xe ions appeared at the collector as lines $\sim$1.5 mm wide and were separated by $\sim$15 mm per mass unit. Under optimum conditions the line width can be reduced to less than 1 mm. A 1-mm$\times$20-mm slit defined the fraction of the Xe^{133} ion beam striking a source foil of 800 μg/cm^2 Al. There was no deceleration voltage at the collector and it is known from other experiments (Davies 1961) that the mean depth of penetration of the ions into the collecting foil was $\sim$8 μg/cm^2.

The conversion lines of the 80.99$\pm$0.02 kev γ-transition in Cs^{133} following β-decay from Xe^{133} are shown in Fig. 1. The β-spectrometer was adjusted for an instrumental resolution of

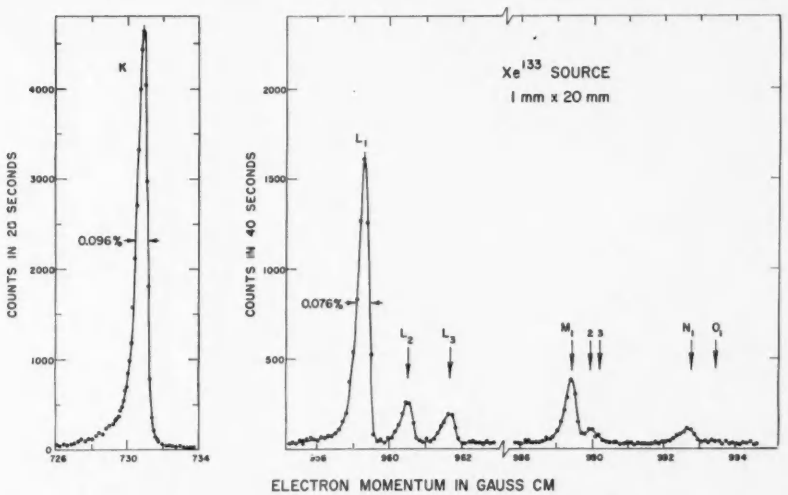

FIG. 1. Conversion electron spectrum of the 80.99-kev gamma transition in Cs^{133}. The points are the observed counts which include β-continuum and background rates.

$\sim$0.07% in momentum. The greater line widths observed experimentally are attributed to source thickness, i.e., to energy loss as the electrons emerge from the depth at which the Xe atoms are located.

The ratios of the line intensities are: $K{:}L_1{:}L_2{:}L_3 = 79\pm2{:}10.0{:}1.48\pm0.05{:}1.15\pm0.05$. Comparison with the theoretical conversion coefficients of Sliv and Band (1957) indicate that the multipolarity of the 80.99-kev transition is 97.4% $M1+(2.6\pm0.2)\%$ $E2$. From this and the measured half-life of $(6.0\pm0.4)\times10^{-9}$ sec for this transition (Graham and Bell 1953) one deduces that the transition rate of the $E2$ component is about five times the single particle estimate (see, for example, Wapstra *et al.* 1959). If one takes into account the statistical factor (Moskowski 1953) of $S = 0.19$ for the spin sequence $5/2 \rightarrow 7/2$ (Bergström 1952) the enhancement factor is $\sim$25. The hindrance factor for the $M1$ component is $\sim$700.

*Issued as A.E.C.L. No. 1229.

ALVÄGER, T. and UHLER, J. 1958. Arkiv Fysik, **13**, 145.
BERGSTRÖM, I. 1952. Arkiv Fysik, **5**, 191.
DAVIES, J. 1961. Private communication to F. Brown.
GRAHAM, R. L. and BELL, R. E. 1953. Can. J. Phys. **31**, 377.
GRAHAM, R. L., EWAN, G. T., and GEIGER, J. S. 1960. Nuclear Instr. and Methods, **9**, 245.
MOSKOWSKI, S. A. 1953. Phys. Rev. **89**, 474.
SLIV, L. A. and BAND, I. M. 1957. Coefficients of internal conversion of γ-radiation. (The K conversion coefficients have been issued as Report 57 I.C.C. K.1 University of Illinois, the L conversion coefficients circulated privately.)
WAPSTRA, A. H., NIJGH, G. J., and VAN LIESHOUT, R. 1959. Nuclear spectroscopy tables (North-Holland Pub. Co.).

RECEIVED APRIL 4, 1961.
RESEARCH CHEMISTRY AND GENERAL PHYSICS BRANCHES,
ATOMIC ENERGY OF CANADA LIMITED,
CHALK RIVER, ONTARIO.

F. BROWN
R. L. GRAHAM
G. T. EWAN
J. UHLER*

*Visitor from the Nobel Institute of Physics, Stockholm, Sweden.

NOTES TO CONTRIBUTORS

Canadian Journal of Physics

MANUSCRIPTS

General.—Manuscripts, in English or French, should be typewritten, double spaced, on paper 8½×11 in. **The original and one copy are to be submitted.** Tables and captions for the figures should be placed at the end of the manuscript. Every sheet of the manuscript should be numbered. Style, arrangement, spelling, and abbreviations should conform to the usage of recent numbers of this journal. Greek letters or unusual signs should be written plainly or explained by marginal notes. Characters to be set in boldface type should be indicated by a wavy line below each character. Superscripts and subscripts must be legible and carefully placed. Manuscripts and illustrations should be carefully checked before they are submitted. Authors will be charged for unnecessary deviations from the usual format and for changes made in the proof that are considered excessive or unnecessary.

Abstract.—An abstract of not more than about 200 words, indicating the scope of the work and the principal findings, is required, except in Notes.

References.—References should be listed **alphabetically by authors' names,** unnumbered, and typed after the text. The form of the citations should be that used in current issues of this journal; in references to papers in periodicals, titles should not be given and only initial page numbers are required. The names of periodicals should be abbreviated in the form given in the most recent *List of Periodicals Abstracted by Chemical Abstracts.* All citations should be checked with the original articles and each one referred to in the text by the authors' names and the year.

Tables.—Tables should be numbered in roman numerals and each table referred to in the text. Titles should always be given but should be brief; column headings should be brief and descriptive matter in the tables confined to a minimum. Vertical rules should not be used. Numerous small tables should be avoided.

ILLUSTRATIONS

General.—All figures (including each figure of the plates) should be numbered consecutively from 1 up, in arabic numerals, and each figure referred to in the text. The author's name, title of the paper, and figure number should be written in the lower left corner of the sheets on which the illustrations appear. Captions should not be written on the illustrations.

Line drawings.—Drawings should be carefully made with India ink on white drawing paper, blue tracing linen, or co-ordinate paper ruled in blue only; any co-ordinate lines that are to appear in the reproduction should be ruled in black ink. Paper ruled in green, yellow, or red should not be used. All lines must be of sufficient thickness to reproduce well. Decimal points, periods, and stippled dots must be solid black circles large enough to be reduced if necessary. Letters and numerals should be neatly made, preferably with a stencil (**do NOT use typewriting**) and be of such size that the smallest lettering will be not less than 1 mm high when the figure is reduced to a suitable size. Many drawings are made too large; originals should not be more than 2 or 3 times the size of the desired reproduction. Whenever possible two or more drawings should be grouped to reduce the number of cuts required. In such groups of drawings, or in large drawings, full use of the space available should be made; the ratio of height to width should conform to that of a journal page (4¾×7½ in.), but allowance must be made for the captions. **The original drawings and one set of clear copies (e.g. small photographs) are to be submitted.**

Photographs.—Prints should be made on glossy paper, with strong contrasts. They should be trimmed so that essential features only are shown and mounted carefully, with rubber cement, on white cardboard, with no space between those arranged in groups. In mounting, full use of the space available should be made. **Photographs are to be submitted in duplicate;** if they are to be reproduced in groups one set should be mounted, the duplicate set unmounted.

REPRINTS

A total of 100 reprints of each paper, without covers, are supplied free. Additional reprints, with or without covers, may be purchased at the time of publication.

Charges for reprints are based on the number of printed pages, which may be calculated approximately by multiplying by 0.6 the number of manuscript pages (double-spaced typewritten sheets, 8½×11 in.) and including the space occupied by illustrations. Prices and instructions for ordering reprints are sent out with the galley proof.

Contents

Printed in Canada *by* University of Toronto Press